Modelling and visualization of a bubble growth in an evolutive, heterogeneous medium

Yannick Laridon

ANNÉE 2014

UNIVERSITÉ DE RENNES 1

ueb

THÈSE / UNIVERSITÉ DE RENNES 1
sous le sceau de l'Université Européenne de Bretagne

pour le grade de

DOCTEUR DE L'UNIVERSITÉ DE RENNES 1

Mention : mécanique

Ecole doctorale SDLM

présentée par

Yannick Laridon

Préparée à l'unité de recherche TERE
(Technologie des équipements agroalimentaires)
Irstea

Modélisation et visualisation d'une croissance de bulle dans un milieu viscoélastique évolutif et hétérogène

Thèse soutenue à Rennes le 5 juin 2014

devant le jury composé de :

Valérie GUILLARD
Maître de conférence, UMR iAte Montpellier
rapporteur

Sofiane GUESSASMA
Chargé de recherche, INRA Nantes
rapporteur

Jean-Dominique DAUDIN
Directeur de recherche, INRA Theix-Clermont
examinateur

Alain LE BAIL
Professeur, ONIRIS Nantes
examinateur

Tiphaine LUCAS
Directrice adjointe scientifique, Irstea Rennes
directeur de thèse

Denis FLICK
Professeur, UMR 1145, Paris
co-directeur de thèse

La reconnaissance silencieuse ne sert à personne

— G. B. Stern

REMERCIEMENTS

La première de mes pensées va à Tiphaine. Il est difficile de donner sur le papier la mesure ma gratitude à son égard, mais son implication sans faille à chaque étape, la force de travail qu'elle su (et pu) déployer, l'invariable méticulosité qui caractérise son travail, sans oublier sa sympathie ont été autant de facteurs clés pour l'aboutissement de cette thèse. Un très grand merci à Denis pour sa patience, sa persévérence, la grande richesse scientifique de ses apports et la constante justesse de ses réflexions. Je tiens à remercier très chaleureusement David pour son accompagnement, son soutien sans faille, sa disponibilité ininterrompue, son amitié, son grand sens physique et la pertinence ses contributions. Je ne désespère pas de danser ensemble une bourrée en bal un de ces jours !

Je remercie très sincèrement Valérie Guillard et Sofiane Guessasma qui ont accepté la tâche de rapporteurs de ce mémoire, ainsi que Jean-Dominique Daudin et Alain Le Bail qui ont accepté de les rejoindre dans le jury.

Tous les travaux réalisés dans le cadre de cette thèse ont bénéficié de la contribution de beaucoup de personnes. Un grand merci à Christophe pour son aide à l'analyse numérique des problèmes étudiés, et pour sa ténacité dans le débogage des programmes qui m'ont accompagné au quotidien. Merci aussi aux personnes de l'équipe IRMFood et de l'unité TERE avec qui j'ai pu travailler. Je remercie en particulier Sylvain pour sa grande disponibilité et sa bonne humeur, Dominique et Michel pour l'ingéniosité dont ils ont fait preuve et qui ont permis que la validation expérimentale se passe aussi bien que possible, Stéphane pour sa pédagogie dans ma découverte de l'IRM, Amina pour son soutien technique et, *last but not least*, un très grand merci à Yvonne, Julie et Marie-Christine pour la très grande qualité de leur accompagnement. Merci aussi à François de m'avoir accueilli, et d'avoir supporté mes velléités à l'encontre des logiciels propriétaites en général, et d'*Office* en particulier. Merci aussi à lui et à tous les partenaires du projet U2M-ChOp pour leurs retours sur le travail accompli pendant cette thèse. En particulier, je remercie Camille pour avoir contribué à lever le voile de brume qui entourait la rhéologie à la sortie de mon master, et tout le monde à AgroParisTech Massy pour m'avoir accueilli et avoir réussi en un temps très bref à me faire renouer avec un accessoire que je pensais avoir laissé au vestiaire il y a longtemps : la blouse. Merci aussi à Guy et Benoît pour leur recul très appréciable par rapport au produit.

Toute ma reconnaissance et ma sympathie pour Maëlle et David H., qui ont contribué de façon non-négligeable à l'aboutissement de cette thèse.

Il serait injuste de laisser penser que ces années se résument uniquement aux interactions professionnelles. Aussi, je tiens à remercier très chaleureusement tous les gens qui rendent plaisante la vie à l'IRSTEA de Rennes. Je pense aux différentes équipes de *Mosaïque*, mais aussi à ceux que j'ai eu le plaisir de rencontrer et avec qui j'ai partagé des moments conviviaux pendant ces quelques années. Une pensée amicale à tous les doctorants du centre. Tout spécialement, je voudrais remercier Cécile, Clément, Delphine et Faustine de s'être trouvés là au même moment. L'aventure n'aurait pas été aussi agréable sans eux.

Naturellement, une pensée aux membres de ma famille qui se demandent bien comment on peut faire des *trucs et des machins* sur du fromage, mais qui n'ont jamais remis en question mon choix de me lancer dans cette entreprise et m'ont toujours soutenu. Enfin, un merci tout particulier à Riwalenn pour son soutien infaillible.

À mon grand-père.

TABLE DES MATIÈRES

LISTE DES TABLEAUX

INTRODUCTION

CONTEXTE GÉNÉRAL DU TRAVAIL DE THÈSE

Les produits agroalimentaires aérés sont présents sous de nombreuses formes, allant des boissons gazeuses, en passant par les mousses laitières et crèmes glacées, les produits céréaliers (pain, biscuits), ou certains fromages. La fraction gazeuse comprise dans ces produits est variable, pouvant atteindre des niveaux très élevés, environ 10% pour les fromages à pâte pressée (Huc et al. 44), 50% minimum pour la crème glacée, 70 à 80% pour le pain. À l'état final dans le pain, les bulles atteignent un diamètre de plusieurs millimètres, alors que pour les fromages à pâte pressée elles atteignent un diamètre de plusieurs centimètres. L'aération, suivant son importance et sa distribution en taille de bulles, donne accès à un panel de textures très riche et constitue un élément non négligeable pour les démarches d'innovation produit. La présence d'ouvertures est une caractéristique organoleptique (principalement visuelle) essentielle des fromages à pâte pressée, qu'elle soit cuite, comme pour l'emmental, ou non, comme pour le maasdammer. Pour le consommateur c'est un critère déterminant d'achat et donc pour le producteur, c'est un indicateur privilégié de la qualité du produit fini, comptant jusqu'à 60 % de la note finale.

Le fromage considéré dans ce travail de thèse appartient à la famille des fromages à pâte pressée non-cuite. Il n'existe pas à proprement parler de codex alimentaire dédié, ni de dénomination canonique pour ce type de fromage (on parle indifféremment de Swiss-type ou de fromage semi-dur), mais ils sont cependant très proches de fromages comme l'emmental (CODEX STAN 269-1967) ou le gouda (CODEX STAN 266-1966). La fermentation lactique et la fermentation propionique sont les deux acteurs majeurs de l'affinage de ce type de fromages. Pour ce type de fromages, la croissance d'ouvertures est en grande partie reliée au développement bactérien (fermentation propionique principalement, Huc et al. 45) au cœur du produit, et constitue en cela un bon révélateur du déroulement de la maturation. Ainsi, trop peu d'ouvertures sont le révélateur d'un développement bactérien limité, qui influencera le produit fini en termes de goût et d'aspect. À l'inverse, trop d'ouvertures est le signe d'un développement bactérien anormal et engendre en outre des problèmes lors de la manutention des produits : avec l'apparition d'ouvertures dites mécaniques par les technologues (ou cracks), qui consistent en une agglomération de bulles de petite taille, des ruptures de blocs ou de meules peuvent se produire lors de la manutention.

Malgré l'importance de la croissance de bulles dans le fromage, du procédé de fabrication jusqu'à la vente, il est paradoxal de constater que la connaissance des phénomènes impliqués lors de la croissance de bulles reste actuellement essentiellement empirique. La multiplicité des phénomènes, aussi bien de microbiologie, de biochimie, de rhéologie, de transport de matière ou de quantité de mouvement, ainsi que leur

possible couplage, expliquent sans doute le peu d'études aujourd'hui disponibles sur le sujet. Cependant, il est important pour l'industriel d'augmenter les connaissances scientifiques autour de la croissance de bulles afin d'améliorer la conduite du procédé de fabrication, et en particulier dans un contexte d'optimisation multicritères où les critères de qualité organoleptique (ouvertures, arômes) peuvent rentrer en compétition avec des critères de qualité nutritionnelle (apport en matière grasse, en minéraux, etc.), ou de maîtrise de critères énergétiques liés à l'affinage du produit (niveau de température, durée).

La modélisation de la croissance de bulles dans les produits agroalimentaires a fait l'objet d'un regain d'intérêt au cours des dix dernières années, avec comme produit cible les produits panifiés ou similaires. Ces études se situent à plusieurs stades du procédé de fabrication, dans des démarches expérimentales, de modélisation ou d'une combinaison de ces deux approches. Cependant, pour des raisons ayant trait aux dynamiques considérées, à la taille et au nombre d'ouvertures dans ces produits, la visualisation et le suivi dans le temps de bulles individuelles est difficile, rendant quasiment impossible la validation expérimentale à l'échelle d'une bulle des modèles utilisés. Pour les études décrivant la croissance individuelle des bulles et incluant une étape de validation, cette dernière s'est faite à une échelle macroscopique (volume total du produit). Dans le cas du fromage, le changement de taille des bulles, allié à une dynamique beaucoup plus lente et à la nature plus rigide de la matrice permettent d'envisager cette étape de validation à l'échelle de la bulle plus aisément. Ce changement d'échelle permet d'instrumenter les bulles en pression ou en température plus simplement que précédemment (plusieurs ordres de grandeur de taille de bulle d'écart) ; le changement d'échelle et de dynamique donne aussi accès à des techniques de tomographie permettant un suivi non-invasif et non-destructif des ouvertures au cours du temps. Ces techniques appliquées à la pâte à pain n'offrent pas la résolution suffisante pour suivre la croissance individuelle de bulles dans un pain de taille réelle ou avoisinante. La meilleure résolution dans le plan de l'image est 1 mm² et combinée avec une épaisseur de coupe très fine comme en RX, elle permet de suivre au mieux les bulles d'un diamètre équivalent voire supérieur (Whitworth and Alava 93). De meilleures résolutions dans le plan peuvent être obtenues sur synchrotron (Babin et al. 7), mais au prix d'une très forte réduction en taille de l'échantillon (de l'ordre du centimètre cube), plus difficilement représentative des conditions réelles du procédé ou au prix de nombreuses astuces expérimentales.

La plupart des phénomènes impliqués dans la croissance de bulle font l'objet d'études parcellaires, les connaissances étant acquises discipline par discipline. Dans un objectif de compréhension des mécanismes associés à la croissance d'ouvertures, la modélisation est un outil précieux. Moyennant l'intégration et la validation de chacune de ces connaissances, elle fournit un moyen d'investigation de l'influence de certains leviers difficilement réalisable expérimentalement. Dans cette optique, la modélisation permet de balayer de façon systématique – et relativement rapide – des situations

qui prendraient beaucoup de temps et de ressources à réaliser via des essais pilotes conduits par un savoir-faire empirique. Encore peu présente dans le domaine agroalimentaire, c'est une approche qui se développe, si ce n'est comme un outil prédictif quantitatif vu la multiplicité des phénomènes étudiés et leur possible couplage – qui englobent très souvent le transport de masse, d'énergie et de quantité de mouvement –, tout du moins comme un moyen de hiérarchisation des phénomènes dominants et d'accompagnement d'une amélioration ciblée du procédé de fabrication.

La présente thèse s'est inscrite au sein du projet de recherche U2M-ChOp *(Understanding, modelling and managing cheese openings)* regroupant deux industriels du secteur laitier (Standa Industries et les fromageries Bel) ainsi que trois acteurs de la recherche publique (équipe IRM-Food de l'Irstea de Rennes, umr 1145, AgroParisTech/Inra/Cnam et l'Ifip de Rennes). L'objectif de ce projet était de mettre en commun des expertises variées sur des problématiques liées à la croissance de bulles dans des fromages à pâte pressée non-cuite. Les domaines d'expertises concernent la conduite de procédés industriels (Bel), la microbiologie (Standa Industries), la rhéologie (umr 1145), la modélisation (umr 1145, Irstea) ou les techniques d'imagerie (Ifip, Irstea). Deux travaux de thèse étaient inclus dans ce projet, ayant tous les deux pour but la hiérarchisation des différents mécanismes impliqués lors de la croissance de bulle, mais construites de façon complémentaire pour mieux couvrir cette problématique. La première (thèse de Delphine Huc, 2013) était positionnée essentiellement à l'échelle du produit entier ($47 \times 23{,}5 \times 9$ cm) et a balayé expérimentalement l'influence de plusieurs paramètres technologiques sur la croissance des bulles et les produits de réactions fermentaires via une méthodologie de type plan d'expérience. Elle a aussi cherché à comprendre le rôle d'éléments structuraux comme les grains de caillé ou les gouttelettes de matière grasse, et développé à cet effet une approche multi-échelle de la phase continue du fromage. La seconde thèse, objet du présent mémoire, était positionnée à l'échelle de la bulle ; en d'autre termes, contrairement à la première thèse, elle n'a pas cherché à prendre en compte l'hétérogénéité spatiale existante à l'intérieur d'un fromage, privilégiant le comportement typique d'une bulle isolée au cœur d'une meule. Ce travail a mis l'accent sur la modélisation des phénomènes impliqués à cette échelle et sa validation expérimentale. Il a été encadré par David Grenier (Irstea) et a bénéficié de l'appui de Christophe Doursat (umr 1145), et co-dirigé par Denis Flick (umr 1145) et Tiphaine Lucas (Irstea).

CONTEXTE BIBLIOGRAPHIQUE

Cette section vise à apporter un regard d'ensemble sur les connaissances liées à la modélisation de la croissance de bulles, pour donner un contexte scientifique général à la thèse. Une étude bibliographique vient introduire chaque chapitre de la thèse pour compléter ce point de vue global.

La croissance de bulles, peu importe le milieu dans lequel elle survient, est conditionnée par : la présence de nuclei ; un apport de gaz depuis le milieu vers la cavité (causé par migration, production, changement de conditions de pression ou de température, etc.) ; et la résistance du milieu à cette croissance de bulle. Les nuclei sont causés par des inhomogénéités de phase dans le milieu, ces inhomogénéités pouvant être subies ou voulues selon les cas. La nucléation sort du cadre de la présente thèse. Cependant le lecteur curieux pourra consulter les travaux d'Akkerman et al. [3] pour plus d'informations sur la nucléation dans le cas de fromages à pâte pressée non-cuite.

Premiers travaux sur la croissance de bulles

La mécanique des fluides est le domaine qui s'est intéressé le premier à l'analyse des cavités. Cette analyse répond à une motivation issue du génie maritime pour lequel les phénomènes de cavitation sont importants. La cavitation est le phénomène de formation et d'évolution de bulles de gaz dans un écoulement de liquide. Ce sont les travaux de Lord Rayleigh en 1917 qui amorcent la réflexion autour du comportement des bulles. La contribution majeure en matière de cavitation est néanmoins celle de Milton S. Plesset, qui a élargi le modèle proposé par Rayleigh (76). Si l'on s'intéresse autant à ce phénomène, c'est que ces cavités sont hautement instables. Dans le cas du génie maritime, la croissance de bulles a lieu au niveau des imperfections des coques ou des hélices, et présente deux conséquences majeures :

1. la nature de l'écoulement est modifiée à mesure que le nombre de bulles augmente (réduisant le rendement des engins) ;
2. l'affaissement ou l'éclatement des bulles a d'une part un effet dévastateur sur les équipements et d'autre part libère des ondes acoustiques favorisant la détection des navires.

On va donc, dans ce cas, chercher à caractériser la croissance de bulles dans le but de la minimiser.

Extension de l'étude de la croissance bulle : le cas des polymères

À la différence de la cavitation, la présence de bulles dans certains procédés de fabrication de polymères est un élément désiré. En effet, les propriétés antichocs de certains matériaux polymères dépendent des propriétés mécaniques de leur phase gazeuse comme la fraction volumique, la densité ou la structure du réseau formé par la mousse (Gibson and Ashby 31). La plupart du temps, la croissance de bulles dans les polymères est provoquée par l'ajout d'un composant en sursaturation dans le milieu, causant ainsi sa migration vers les nuclei, voire dans certains cas l'établissement d'un régime d'ébullition. La production de gaz dans le milieu peut aussi être provoquée par réaction chimique. Dans le cas des polymères, les milieux considérés contiennent un très grand nombre de bulles relativement rapprochées, subissant des déformations importantes, allant jusqu'à la coalescence. La démarche de modélisation reprend les bases établies pour l'étude de la cavitation, mais un formalisme a été adopté par un grand nombre d'études : le modèle de cellule d'Amon et Denson (5). Ce modèle consiste à étudier un motif unitaire représentatif du comportement à l'échelle macroscopique des bulles, et est constitué d'une bulle entourée d'une sphère concentrique de liquide. L'interaction entre la bulle et le domaine qui l'entoure est ensuite considérée et selon les polymères étudiés et le niveau de complexité des études, différents phénomènes sont envisagés. Le comportement mécanique du milieu est le plus souvent considéré comme visqueux (Amon and Denson 5, Venerus and Yala 90), même si certaines études utilisent des lois de comportement viscoélastiques non-linéaires (Ramesh et al. 77, Feng and Bertelo 29). Plusieurs types de transports sont aussi considérés, suivant les procédés de fabrication étudiés. La plupart des études considèrent l'interaction entre le transport de quantité de mouvement et le transport de matière, mais si le procédé étudié nécessite le chauffage du matériau, le transport d'énergie peut aussi être envisagé (Lee et al. 62).

Application au domaine agroalimentaire

La modélisation de la croissance de bulles dans le domaine agroalimentaire doit beaucoup aux produits céréaliers, les extrudés et le pain en particulier. Dans le cas des produits céréaliers, les nuclei sont majoritairement provoqués par l'aération de la pâte lors de l'étape de pétrissage, alors que pour les fromages à pâte pressée non-cuite, les nuclei sont majoritairement provoqués par des imperfections au niveau des jonctions de grains de caillé lors du pressage ou par l'inclusion de bulles d'airs dans le caillé (Clark 18, Akkerman et al. 3). Dans le pain, la fermentation (ou pousse) et la cuisson sont les deux étapes de fabrication les plus remarquables pour la croissance de bulles. C'est l'étape de fermentation qui se rapproche le plus des conditions dans lesquelles se produit la croissance de bulles dans les fromages à pâte pressée non-cuite. En effet, les mécanismes mis en œuvre sont les mêmes, à savoir une fermentation bactérienne

produisant un gaz qui diffuse sous forme dissoute dans la pâte en direction des nuclei, et provoque après dé-solubilisation la croissance d'ouvertures. Dans le cas du pain, il s'agit d'une fermentation alcoolique, alors que dans le cas du fromage, c'est majoritairement la fermentation propionique qui est en cause (Huc 46). Dans les deux cas, la croissance de bulle est dépendante de l'activité fermentaire, qui conditionne en grande partie la production de gaz au cours du temps, mais aussi de la capacité du gaz à diffuser dans la pâte (la diffusion étant modélisée par la loi de Fick) et de la résistance mécanique de la pâte (souvent modélisée par un modèle purement visqueux). Les travaux centrés sur la fermentation de la pâte à pain s'inspirent fortement des travaux sur les polymères, et à raison tant les dynamiques et les tailles de bulles sont proches. En revanche, la fermentation des fromages considérés dans ce travail de thèse se produit sur des temps beaucoup plus longs. La fabrication de pain est de l'ordre de quelques heures, alors que la maturation de fromages à pâte pressée non-cuite s'étale sur plusieurs semaines. De plus, le changement de dimension impose d'adapter les hypothèses de travail, comme par exemple le fait que la tension de surface, importante sur les bulles de petite taille rencontrées dans les polymères et les matrices céréalières, devienne négligeable dans le cas de la croissance de bulle dans le fromage. À l'inverse, la large taille des bulles rencontrées dans les fromages à pâte pressée permet d'envisager une instrumentation à l'échelle d'une bulle, pour apporter une validation plus approfondie des mécanismes supposés et rassemblés dans un modèle de connaissance. Enfin, bien qu'étant tous deux des matériaux viscoélastiques, le comportement rhéologique de la matrice fromagère diffère de celui de la pâte à pain, et il faut signaler que la caractérisation rhéologique du fromage a été très bien traitée dans le domaine élastique mais que les caractérisations viscoélastiques sont rares. Il n'y a à ce jour et à notre connaissance, aucune étude complète portant sur la modélisation de croissance de bulles au sein de fromages à pâte pressée non-cuite.

POSITIONNEMENT DES TRAVAUX DE THÈSE

Les principales originalités des travaux réalisés pendant cette thèse se situent à deux niveaux. Le premier consiste en l'adaptation de la modélisation de croissance de bulle à un nouveau matériau : le fromage à pâte pressée non-cuite. Le modèle développé se rapproche d'autres modèles de fermentation de pâte à pain, mais avec des dynamiques et des échelles différentes. Le second niveau consiste en la mise en place de protocoles expérimentaux de validation du modèle, et au soin apporté à la détermination expérimentale des paramètres du modèle et leurs incertitudes. Rappelons que pour la croissance de bulle survenant dans les mousses polymériques ou les produits céréaliers, il est difficile de réaliser une validation expérimentale à une échelle autre que globale (échelle du produit) et la phase gazeuse est souvent caractérisée uniquement par sa contribution au volume total. D'un autre côté, les valeurs des paramètres d'entrée du modèle sont rarement acquises sur le matériau d'étude, mais repris dans

des études antérieures portant sur des matériaux ou conditions avoisinantes. Un effort particulier du travail de thèse a porté sur l'acquisition de certains paramètres, jugés clé a priori, sur le matériau d'étude du travail de thèse. Le postulat de départ du présent travail de thèse se base sur une prédominance du comportement mécanique de la matrice fromagère sur la croissance de bulle. Ce postulat, doublé par l'insuffisance de la littérature à ce sujet, a motivé une attention particulière à la caractérisation mécanique du produit. Cette caractérisation a fait l'objet d'une validation expérimentale dans les conditions réelles de sollicitation du matériau fromage (extension bi-axiale à l'interface de la bulle), elle-même découplée des effets liés au transport de matière.

ORGANISATION DU TRAVAIL DE RECHERCHE MENÉ PENDANT LA THÈSE

La thèse a été structurée en trois étapes, chacune de ces étapes comprenant une part non négligeable d'études expérimentales :

- la caractérisation mécanique du fromage étudié ;
- la modélisation de la croissance de bulle d'un point de vue mécanique uniquement ;
- la modélisation de la croissance de bulle comprenant le couplage entre comportement mécanique et transport de matière.

1re étape. Caractérisation mécanique du fromage étudié

Elle consiste à acquérir des données rhéologiques sur le fromage étudié, à mettre au point une méthode de détermination des paramètres mécaniques du fromage à partir des tests expérimentaux, et à estimer les incertitudes induites par la méthode sur les valeurs identifiées des paramètres mécaniques. Plusieurs tests de compression-relaxation en conditions lubrifiées ont été réalisés par les partenaires de l'UMR 1145 sur le site de Massy (Antony Hutin, Julien Mottet, Gabrielle Moulin et Camille Michon), ma contribution se situant au niveau de l'établissement et de l'amélioration, à plusieurs reprises, du protocole expérimental. La méthode de détermination des paramètres consiste en la reproduction numérique de ce test de compression relaxation, et à la minimisation des écarts entre les données expérimentales et les prédictions du modèle numérique développé. Le modèle viscoélastique retenu est le modèle de Maxwell généralisé, un modèle viscoélastique linéaire qui a l'avantage de la simplicité. La variation des paramètres au cours de l'affinage et en fonction de la position dans le fromage a été étudiée. Cette étape constitue le premier chapitre du présent mémoire.

2e étape. Modélisation de la croissance de bulle d'un point de vue mécanique uniquement

La seconde étape comprend aussi une approche expérimentale et de modélisation combinée. Tout d'abord un protocole expérimental dédié a été mis au point pour reproduire une croissance de bulle en condition de sollicitations mécaniques connues. Ensuite, un modèle numérique de croissance de bulle se basant sur le modèle mécanique mis en œuvre lors de la première étape et reproduisant au plus près le dispositif de validation expérimental a été implémenté. Le dispositif expérimental a consisté à

faire croître une bulle isolée dans un cylindre de fromage en maitrisant les conditions de contraintes à l'intérieur de la bulle ainsi qu'aux autres limites du système fromage, et en mesurant les changements sur la bulle au cours du temps grâce l'imagerie par résonance magnétique (IRM). La présentation du dispositif expérimental, mis au point par un de mes encadrants de proximité, David Grenier, et par Dominique Le Ray (assistant ingénieur de l'équipe IRM-Food de l'Irstea) fait l'objet du deuxième chapitre du présent mémoire. Ma contribution se situe au niveau de la discussion des effets observés expérimentalement et leur interprétation sur le comportement mécanique du fromage, ainsi que sur des questions d'incertitude de mesure. Le 3^{e} chapitre présente quelques redondances avec le chapitre suivant mais présente *in extenso* le dispositif expérimental utilisé dans ces deux chapitres.

Le modèle numérique développé a ensuite été confronté aux données expérimentales dans le but de valider l'adéquation du modèle de Maxwell (et de son paramétrage) en configuration de sollicitation réelle, lors d'une croissance de bulle. Il a aussi servi à la réalisation d'études de sensibilité donnant un regard critique sur l'influence des paramètres du modèle mécanique sur la croissance d'une bulle. Les incertitudes sur la détermination des paramètres d'entrée du modèle – issues du travail présenté dans le 1er chapitre – ont été propagées avec le modèle, permettant de présenter les résultats de simulation sous forme d'un « domaine de confiance ». Les résultats de l'étude de sensibilité ont été obtenus avec l'aide d'un stagiaire de master 2 (David Houeix), que j'ai encadré. L'ensemble des résultats de modélisation de cette étape font l'objet du troisième chapitre du présent mémoire.

3^{e} étape. Modélisation de la croissance de bulle comprenant le couplage entre comportement mécanique et transport de matière

Le modèle développé dans la seconde étape a été repris pour y ajouter une description des transports et échanges de matière. La validation de ce modèle et de son paramétrage s'est déroulée en deux temps. C'est néanmoins la deuxième configuration expérimentale qui a guidé le développement du modèle, ce qui peut expliquer certaines inadéquations avec la première configuration de validation. On cherchera à montrer que ces inadéquations sont somme toute minimes. Dans un premier temps, les résultats de simulation ont été comparés au comportement moyen d'une bulle dans des blocs de fromage, en se basant sur les données expérimentales acquises sur fromages industriels dans le cadre de la thèse de D. Huc. Une étude de sensibilité a été conduite sur le modèle numérique pour discuter de l'influence respective des différents phénomènes de transport envisagés sur la croissance de bulle. Cette étude a à son tour alimenté une réflexion sur la plage de valeurs attendues ou acceptable pour les paramètres d'entrée non mesurés dans la présente étude, mais estimés à partir de la littérature. Cette partie (modèle et validation) fait l'objet du chapitre 4 du présent mémoire.

Dans un deuxième temps, nous avons cherché à étudier l'interaction entre deux cavités gazeuses. Un nouveau dispositif expérimental, adapté de l'étape 2, a été développé à cet effet. À la différence de la deuxième étape du travail de thèse, le dispositif développé n'envisage pas le suivi de la pression à l'intérieur de la bulle, mais l'observation d'une bulle laissée libre, en maitrisant toujours les conditions aux limites en termes de transport de matière et de quantité de mouvement. Un cylindre de fromage contenant une seule bulle a été placé dans un dispositif hermétique, contenant un espace de tête qui agit comme une deuxième bulle à proximité. Le modèle numérique a été adapté pour correspondre le plus possible à ces conditions expérimentales. Ce dispositif expérimental a nécessité une longue phase de mise au point (nature des gaz des cavités gazeuses, fuites, panne de capteurs, décollement des parois latérales, etc.), que j'ai entièrement gérée, contrairement aux autres étapes. Pour cette phase de mise au point, j'ai bénéficié de l'aide d'une stagiaire d'IUT (Maëlle Gueneugues). Les résultats reportés dans ce mémoire sont préliminaires, car bien que le protocole soit désormais maitrisé, les résultats font apparaître certains enseignements qui incitent à l'amélioration de ce protocole et à la réalisation d'acquisitions supplémentaires. La présentation de cette étape fait l'objet du cinquième chapitre du présent mémoire.

Chaque étape est rédigée sous forme d'une ou plusieurs publications dans un journal scientifique à comité de lecture. La première publication (chapitre 1), a été soumise au journal *Rheologica Acta* fin 2013. Les deux publications suivantes (chapitres 2 et 3) sont prêtes à être soumises en avril 2014, dans *Journal of Materials Science* pour la première et *Journal of the Mechanics and Physics of Solids* pour la deuxième. Le chapitre 4 sur le comportement moyen des bulles dans les blocs de fromage et son approche par modélisation sera soumis à un journal du type *Journal of Food Engineering*. Le chapitre 5, s'intéressant à l'interaction entre deux cavités gazeuses d'un point de vue expérimental, est présentée à titre d'ouverture possible des travaux réalisés. Davantage de travaux sont à envisager pour pouvoir transmettre les résultats et leurs enseignements sous forme de publication. Il est néanmoins rédigé en anglais et en suivant les règles d'une publication à comité de lecture.

Chaque étape a fait l'objet d'une bibliographie spécifique, et relativement découplée des autres étapes, qui se trouve sous une forme condensée en introduction de chaque article. En raison de ce découpage sous forme de publications, toute la nomenclature n'est pas forcément homogène à l'échelle du document. Les références bibliographiques sont en revanches toutes réunies en fin de manuscrit. Enfin, les principaux apports du travail de thèse sont rassemblés dans un dernier chapitre de conclusion.

Chapitre 1

NEW ASSESSMENT METHOD OF THE VISCOELASTIC PARAMETERS OF MATERIALS. APPLICATION TO SEMI-HARD CHEESE.

This paper sets out a method to extract Maxwell model parameters from experimental compression-relaxation tests, and investigates common experimental sources of bias when dealing with viscoelastic materials. Particular attention was given to viscoelastic materials that relax stress quickly. The proposed method differs from the methods usually used in that it takes into account the stress that can relax when a material is submitted to compression before proper relaxation. Among the experimental biases that can affect the tests, this study investigated the impact of the geometry defects of the samples, of the sensitivity of the rheometer used and of the compression speed on the characterisation of the material. The uncertainties caused by these biases were then propagated in the proposed method. The proposed method was used to study the evolution of the viscoelastic properties of semi-hard cheese during ripening. Variability between cheeses proved to be greater than the uncertainty of the proposed method, and no tendency could be established, meaning that the viscoelastic parameters were considered constant during ripening.
Keywords : generalised Maxwell model; viscoelasticity; characterisation; ripening

1 INTRODUCTION

The rate of deformation of foods is high during mastication and deformation is considerable, often to the extent of fracture (O'Callaghan and Guinee 70). Objective characterisation of food properties in this context is important for the food industry, beginning for cheese with the studies of Harper and Baron [41], the various measurement techniques being summarised by Szczesniak in 1963. Interest in the constitutive modelling of the mechanical behaviour of food materials has been more limited. Despite the inspirational work of Peleg that validated the use of the generalised Maxwell model for the description of viscoelastic food products (Peleg 74), modelling studies in food science area are more rare than in the polymer science where the approach was first used during the 50's (*e.g.* Tobolsky 88). As other food products, cheese exhibits viscoelastic behaviour, as modelled successfully by Masi [65] for the first time for Italian cheeses. The results of studies from Goh et al. [34] and Del Nobile et al. [24] showed that cheese (particularly pressed cheese) exhibits a wide range of relaxation times: although part of the stress relaxes quickly (relaxation time of a few seconds at most), there is a slower return to equilibrium due to longer relaxation times (about 1 ks). Cheese is therefore a material that needs both a short compression stage to limit the early relaxation and a long relaxation stage to exhibit the long-term behaviour of the material for adequate characterization of its mechanical parameters, as suggested by Buggisch et al. [13].

Linear viscoelasticity is only suitable for materials which exhibit both elastic and viscous behaviours. The range of applications for viscoelastic materials is wide since it can be used in geophysics and seismology science, polymer and biomedical science and structural engineering (Lakes 56). Although few actual loading situations match the small strain assumption, linear viscoelasticity is easily modelled, the generalised Maxwell model being the most frequently used. A set of material properties can be adjusted after applying a given low level of strain impulse and observing the material stress response according to time in a compression-relaxation test. Many studies have been performed on the subject with the analysis of compression or tension and relaxation tests, dynamic studies and acoustic studies, and there are many ways to approach linear viscoelasticity. However, the compression-relaxation test remains the simplest way to determine the Maxwell model parameters.

Ideally the time needed to reach the maximum level of strain (the compression stage) has to be much shorter than the shortest relaxation time so that elastic and viscous properties can be disentangled as far as possible. When little stress relaxation occurs during compression, it is possible to determine a set of Maxwell model parameters only by fitting experimental data during the relaxation stage with a sum of exponential

decays (Del Nobile et al. 24, Masi 65). The elastic modulus can also be determined from the linear regression of the experimental data from the compression stage only. However, the upper plate speeds which can be applied in compression-relaxation tests are limited by the available machines. As a large amount of stress may relax during compression of specific materials, determination of the shortest relaxation time and the elastic modulus could be biased and relaxation cannot be considered independently from compression and vice versa, and thus models taking into account the whole strain-stress history are required.

Some earlier studies dedicated to food materials have already considered minimisation of the difference between the stress calculated using linear or non-linear viscoelastic models in FEM (finite-element method) computation and the stress measured experimentally in a compression-relaxation or an indentation test. Kim et al. [52] computed the stress generated in a compression-relaxation test as a whole using ANSYS with the built-in non-linear fitting functionality (SUMT algorithm); they assessed the parameter values of a two-element Maxwell model by minimizing the error between the modelled and the experimental stress data. This method made it possible to determine both the elastic and the viscous properties appropriately. The method was validated on agar/agar-gelatin gels and was applied to apple material (Kim et al. 52, 53).

In a large strain indentation test situation, Goh et al. [33] used a visco-hyperelastic model, and the mechanical properties were evaluated by non-linear fitting (implemented by the ABAQUS FEM software). Being a non-linear approach, the large strain behaviour of materials was evaluable up to 15%. Nevertheless, as the model had a greater number of parameters to be adjusted than that in the Maxwell model, a priori assumptions on the relaxation times were required and only the proportions of each element were adjusted by a minimization method.

The sensitivity of the fitting method to experimental conditions was not investigated in these earlier studies, as they failed to evaluate the effectiveness and the limitations of the proposed method. The effects of the experimental noise on the numerical methods may induce error in the determination of parameters, especially for the short relaxation component if the experimental data acquisition frequency is not high enough. The speed of the upper plate can also impact on the way the stress or strain is applied to the material. Finally, a small degree of non-parallelity between the upper and lower surfaces of the material under compression-relaxation can shift the measured stress to lower values than those normally measured when faces are perfectly parallel (Del Nobile et al. 24).

The aims of this study were to model a compression-relaxation test as a whole with the Maxwell model and to propose a method of identification of the Maxwell model parameters. The provided identification method was then used for semi-hard cheese characterisation. In this respect, the main contribution of this study is methodological.

Compared to previous studies, the method implementation was not software-dependent, and the uncertainties were calculated to provide an estimate of its effectiveness under a wide range of operating conditions. Special care was paid to retrieving the stress relaxed during the compression stage, making the proposed method particularly appropriate for materials such as some cheese showing both short and long relaxation times. Instantaneous, linear and non-linear compression conditions versus time during the downward displacement of the upper plate were considered.

In the second stage, the impact of the experimental errors on the uncertainty of Maxwell model parameters was investigated. Uncertainty encompasses systematic error (bias) and variability, which can be approached by standard deviation. The uncertainty of the calculated parameters was also compared to those obtained with a reference method. This reference method included linear and multiple exponential regressions evoked earlier in the introduction and which are considered to be valid in the case where the compression stage is much shorter than the shortest relaxation time. Particular attention was paid to the influence of the level of noise, to the compression stage (the upper plate speed) and to the parallelity of the upper and lower sample surfaces. Such experimental bias are known of the experimenter, but were rarely assessed thoroughly. One outcome of these first two stages of the study was estimation of the overall uncertainty associated with each Maxwell model parameter.

In the third stage, the method was applied to a semi-hard cheese for determination of the viscoelastic properties along a profile in a cheese block at given ripening times and at the core of the cheese block during ripening; observed variations are discussed in relation to the uncertainties estimated previously.

2 MATERIALS AND METHOD

2.1 MODELLING OF THE COMPRESSION-RELAXATION TEST

The underlying hypotheses of compression-relaxation test modelling are first presented in the following subsection and are only discussed in the light of the experimental conditions later on when presenting the experimental method. The mechanical approach and the momentum equation to be solved are then presented. The initial compression stage of the compression-relaxation test is then examined theoretically according to the three possible configurations of downward motion of the upper plate of the rheometer. The method which was developed in this study to determine the Maxwell model parameters from the force-time and force-strain experimental data during both the compression and the relaxation stages is then presented, as well as the classical reference method to which it was compared. As no ideal Maxwell material was available to check the ability of the proposed and the reference methods to determine the Maxwell model parameters, a simulated set of data from fictive reference Maxwell material was computed. Finally the experimental device and procedure used for the measurement of the material reaction force, upper plate displacement and time are presented in the last subsection.

2.1.1 *Modelling hypotheses*

A typical experimental result is presented in Figure 1.12. The uniaxial compression-relaxation test for a vertical cylindrical sample of cheese was modelled. In view of the symmetry of the sample, a 2-D axisymmetric domain was considered except when the upper and lower surfaces of the cylinder were not parallel (see the section 2.5).

A generalised Maxwell model was used to model the linear viscoelastic behaviour of the cheese. The cheese studied was also assumed to be a nearly-incompressible material. Cheese was assumed to be homogeneous and isotropic.

Roller boundary conditions were hypothesised for the upper and lower surfaces of the cylinder and the lateral surface of the cylinder was free. No initial stress was considered inside the cheese.

Inertia, convection terms, vorticity and gravity were ignored conservation of momentum law, that was thus reduced to a quasi-static equilibrium.

2.1.2 *Governing laws*

For quasi-static equilibrium the conservation of momentum law is written

$$\nabla \cdot \boldsymbol{S}(t) = 0 \tag{1.1}$$

where $\boldsymbol{S}$ is the stress tensor and can be expressed as the sum of the viscoelastic stress tensor $\boldsymbol{\tau}$ and the elastic stress tensor $\boldsymbol{\sigma}$. The former is governed by the generalised n-element Maxwell model (Eq. 1.11), while the latter is governed by the tensor form of Hooke's law

$$\boldsymbol{\sigma}(t) = \boldsymbol{C} : \boldsymbol{\epsilon}(t) \tag{1.2}$$

where $\boldsymbol{C}$ is the tensor of rigidity, and $\boldsymbol{\epsilon}$ the strain tensor. Assuming isotropy, expressing Eq. (1.2) in terms of shear and bulk modules yields

$$\boldsymbol{\sigma}(t) = \boldsymbol{C}_d \left(\boldsymbol{\epsilon}(t) - \frac{1}{3}\mathrm{tr}\left(\boldsymbol{\epsilon}(t)\right) \boldsymbol{I} \right) + K\mathrm{tr}\left(\boldsymbol{\epsilon}(t)\right) \boldsymbol{I} \tag{1.3}$$

where $\boldsymbol{C}_d$ is the rigidity deviator tensor defined as

$$G_0 \begin{pmatrix} 4/3 & -2/3 & -2/3 & & & \\ -2/3 & 4/3 & -2/3 & & & \\ -2/3 & -2/3 & 4/3 & & & \\ & & & 2 & & \\ & & & & 2 & \\ & & & & & 2 \end{pmatrix} \tag{1.4}$$

$\boldsymbol{I}$ is the identity matrix, and K is defined as

$$K = \frac{2G\left(1+\nu\right)}{3\left(1-2\nu\right)} \tag{1.5}$$

and G is the total shear modulus, defined as

$$G = G_0 + \sum_{i=1}^{n} G_i \tag{1.6}$$

where ν is the Poisson's ration, and G_0 the time-independent shear modulus.

Taking advantage of the axisymmetry, assuming no vorticity and small strain, Cauchy's infinitesimal strain tensor is written

$$\boldsymbol{\epsilon}(t) = \begin{pmatrix} u_{r,r}(t) & & \\ & u_r(t)/r(t) & \\ & & u_{z,z}(t) \end{pmatrix} \tag{1.7}$$

where u_r is the r-component of the displacement field, u_z its z-values and the comma denotes the partial derivative ($u_{\theta\theta} = 0$ due to axial symmetry). The roller boundary conditions mean that there is no shear stress at the cheese-plate interfaces. The displacement field can therefore be considered as linearly dependent on the space coordinates ($u_r = ar$ and $u_r = -bz$). Assuming this linearity, Eq. (1.7) yields

$$\boldsymbol{\epsilon}(t) = \begin{pmatrix} a(t) & & \\ & a(t) & \\ & & -b(t) \end{pmatrix} \tag{1.8}$$

All the horizontal sections of the vertical cylinder are submitted to the same deformation. In perfectly lubricated conditions, the strain and stress tensor values are independent of the position inside the sample and depend only on time. Given the form of the strain tensor, Eq. (1.3) becomes

$$\boldsymbol{\sigma}(t) = \frac{2}{3}G_0 \begin{pmatrix} 2 & -1 & -1 \\ -1 & 2 & -1 \\ -1 & -1 & 2 \end{pmatrix} \begin{pmatrix} a(t) - \frac{1}{3}(2a(t) - b(t)) \\ a(t) - \frac{1}{3}(2a(t) - b(t)) \\ -b(t) - \frac{1}{3}(2a(t) - b(t)) \end{pmatrix} + K(2a(t) - b(t))\,\boldsymbol{I} \tag{1.9}$$

For the generalised Maxwell model, the global form is

$$\boldsymbol{\tau}(t) = \sum \boldsymbol{\tau}_i \tag{1.10}$$

so that the following equation has to be solved for each Maxwell element i

$$\boldsymbol{\tau}(t) + \lambda_i \dot{\boldsymbol{\tau}}(t) = G_i \lambda_i \dot{\boldsymbol{\gamma}}(t) \tag{1.11}$$

where G_i and λ_i are the shear modulus and relaxation time, respectively, of each element $i \in \{1, \cdots, n\}$, the dot ($\dot{}$) denotes the time derivative and the strain deviator tensor $\boldsymbol{\gamma}$ is defined as

$$\boldsymbol{\gamma}(t) = \boldsymbol{\epsilon}(t) - \tfrac{1}{3}\mathrm{tr}\,(\boldsymbol{\epsilon}(t))\,\boldsymbol{I} = \tfrac{1}{3}(a(t) + b(t)) \begin{pmatrix} 1 & & \\ & 1 & \\ & & -2 \end{pmatrix} \tag{1.12}$$

Given the form of the strain deviator tensor, $\tau_{rr}(t) = \tau_{\theta\theta}(t) = -1/2\tau_{zz}(t)$. This also yields $S_{rr}(t) = S_{\theta\theta}(t)$. In view of the previous hypothesis, the axisymmetric form of Eq. (1.1) reduces to

$$\begin{cases} S_{rr,r}(t) &= 0 \\ S_{\theta\theta,\theta}(t) &= 0 \\ S_{zz,z}(t) &= 0 \end{cases} \tag{1.13}$$

Moreover, Eq. 1.13 combined with the absence of radial stress on the side of the cylinder (free lateral boundary condition) becomes $S_{rr}(t) = S_{\theta\theta}(t) = 0$. Thus the following system is obtained:

$$\begin{cases} S_{rr}(t) &= \frac{2}{3}G_0\left(a(t)+b(t)\right) + K\left(2a(t)-b(t)\right) - \frac{1}{2}\tau_{zz}(t) &= 0 \quad (i) \\ S_{zz}(t) &= -\frac{4}{3}G_0\left(a(t)+b(t)\right) + K\left(2a(t)-b(t)\right) + \tau_{zz}(t) & \quad (ii) \end{cases} \tag{1.14}$$

Subtracting Eq. 1.14*ii* from Eq. 1.14*i* gives the following expression of the stress:

$$S_{zz}(t) = \tfrac{3}{2}\tau_{zz}(t) - 2G_0\left(a(t)+b(t)\right) \tag{1.15}$$

No time-independant elasticity was considered for the material studied (see Chapter 2), thus $G_0 = 0$. The stress is then reduced to:

$$S_{zz}(t) = \tfrac{3}{2}\sum_{i=1}^{n}\tau_{zz}^{i}(t) \tag{1.16}$$

where $\tau_{zz}^{i}(t)$ can be calculated from Eq 1.11:

$$\tau_{zz}^{i}(t) + \lambda_i\dot{\tau}_{zz}^{i}(t) = -2G_i\lambda_i\dot{b}(t) \tag{1.17}$$

The global shear modulus G and the proportion of each element in terms of shear modulus α_i are written:

$$G = \sum G_i \tag{1.18}$$

$$\alpha_i = \frac{G_i}{G} \tag{1.19}$$

2.2 IDENTIFICATION OF THE MAXWELL MODEL PARAMETERS

In the compression-relaxation test, the compression cannot be assumed to be instantaneous. A small amount of stress is relaxed during the compression stage. Three relationships between the upper plate displacement and time were considered in the theoretical approach of the compression stage. The proposed fitting method takes into account the loss of stress during the compression in the cases of linear and non-linear compression.

2.2.1 *Instantaneous compression*

When the compression is considered as instantaneous, the upper plate reaches its final position instantaneously and no stress relaxation occurs; the solution of Eq. 1.16 is written

$$S_{zz}(t) = -3\frac{d_c}{H_0}G\sum_{i=1}^{n}\alpha_i \exp\left(-\frac{t}{\lambda_i}\right) \tag{1.20}$$

where H_0 is the initial height of the cylinder and d_c the maximum displacement of the upper surface of the sample (*i.e.* its value at the end of the compression stage).

2.2.2 *Linear compression*

In the case where the downward displacement of the upper plate is linear with time followed by holding the upper plate position, the height of the sample according to time is defined as

$$\begin{cases} H(t) &= H_0 - \frac{t}{t_c}d_c & , t \leq t_c \\ H(t) &= H_0 - d_c & , t > t_c \end{cases} \tag{1.21}$$

where t_c is the time taken to achieve the maximum displacement. This leads to the following expression of the z-component of strain

$$b(t) = \begin{cases} \frac{t}{t_c}\frac{d_c}{H_0} & & , t \leq t_c \\ \frac{d_c}{H_0} &= b(t_c) & , t > t_c \end{cases} \tag{1.22}$$

For $t \leq t_c$, the solution of Eq. 1.17 is written

$$\tau_{zz}^i(t) = -2\lambda G_i \frac{b(t_c)}{t_c}\left(1 - \exp\left(-\frac{t}{\lambda_i}\right)\right) \tag{1.23}$$

This can be re-written in order to highlight the proportion of stress that did not relax during compression

$$\tau_{zz}^i(t) = -2G_i b(t_c) p_i(t) \tag{1.24}$$

where p_i is defined as

$$p_i(t) = \frac{1 - \exp\left(-\frac{t}{\lambda_i}\right)}{\frac{t_c}{\lambda_i}} \tag{1.25}$$

If $p_i(t_c)$ remains close to 1, no stress has been relaxed during compression. The more $p_i(t_c)$ diminishes, the more stress has been relaxed. The combination of Eqns. 1.16 and 1.24 gives the overall form of the stress during the compression stage

$$S_{zz}(t) = -3Gb(t_c)\sum_{i=1}^{n}\alpha_i p_i(t),\ t \leq t_c \tag{1.26}$$

For $t > t_c$, Eq. 1.17 has a null right-hand term, so that the solution is written

$$\tau_{zz}^{i}(t) = -2G_i\frac{b(t_c)}{t_c}\lambda_i\left(1-\exp\left(-\frac{t_c}{\lambda_i}\right)\right)\left(\exp\left(-\frac{t-t_c}{\lambda_i}\right)\right) \tag{1.27}$$

Combining Eqns. 1.27 and 1.16 yields the overall expression of the stress

$$S_{zz}(t) = -3Gb(t_c)\sum_{i=1}^{n}\alpha_i p_i(t_c)\exp\left(-\frac{t-t_c}{\lambda_i}\right),\ t > t_c \tag{1.28}$$

The first step in the determination of Maxwell model parameters was applied to the relaxation stage. The stress was divided by the state of stress at the beginning of the relaxation stage

$$S_{zz}^{*}(t') = \frac{S_{zz}(t'+t_c)}{S_{zz}(t_c)} = \sum_{i=1}^{n}\frac{\alpha_i p_i(t_c)}{\sum_{j=1}^{n}\alpha_j p_j(t_c)}\exp\left(-\frac{t'}{\lambda_i}\right) = \sum_{i=1}^{n}c_i\exp\left(-\frac{t'}{\lambda_i}\right) \tag{1.29}$$

where c_i are the proportions of the stress in Maxwell elements at the beginning of the relaxation stage, starting at $t^{'} = t - t_c = 0$. However, relaxation already occurs during the compression stage (Eq. 1.24), and therefore the c_i are not directly equal to the true proportions α_i of the moduli. Instead, c_i and α_i are related according to the following equation

$$c_i = \frac{\alpha_i p_i(t_c)}{\sum_{j=1}^{n} a_j p_j(t_c)} \tag{1.30}$$

which can be re-written as the following system

$$\forall i \in \{1,\cdots,n\},\ \alpha_i(1-c_i)p_i(t_c) - \sum_{\substack{j=1\\ j\neq i}}^{n} c_j\alpha_j p_j(t_c) \tag{1.31}$$

where c_i and $p_i(t_c)$ can be estimated by regression from the stress measurements during the relaxation stage (Eq. 1.29).

2.2.3 *Non-linear compression*

In the case where the compression has no specific form, the general solution of Eq. 1.11 is written

$$\tau_{zz}^{i}(t) = -2G_i \int_0^t \dot{b}(\xi) \exp\left(-\frac{t-\xi}{\lambda_i}\right) d\xi \tag{1.32}$$

The proportion of stress $p_i(t_c)$ that did not relax during compression is written

$$p_i(t_c) = \frac{1}{b(t_c)} \int_0^{t_c} \dot{b}(\xi) \exp\left(-\frac{t_c-\xi}{\lambda_i}\right) d\xi \tag{1.33}$$

Expression of the stress at the end of compression then becomes

$$S_{zz}(t_c) = -3Gb(t_c) \sum_{i=1}^{n} \alpha_i p_i(t_c) \tag{1.34}$$

During the relaxation stage, Eqns. 1.29 to 1.31 apply as previously. This third non-linear case was used for the numerical computation.

2.3 IMPLEMENTATION OF THE PROPOSED METHOD

First, the relaxation times λ_i and the proportions c_i were calculated by a least squares minimisation of the difference between computed and experimental force-time data during the relaxation stage. The computed force F_{sim} was calculated from the expression of the simulated stress S_{zz} as

$$F_{sim}(t) = S_{zz}(t)\mathcal{A}(t) = S_{zz}(t)\pi R^2(t) \tag{1.35}$$

where the area $\mathcal{A}(t)$ is a function of the experimental cylinder radius $R(t)$

$$R(t) = R_0\left(1 - \nu b(t)\right) \tag{1.36}$$

where R_0 is the initial radius, ν the Poisson's ratio, and $b(t)$ the strain in the z-direction defined as

$$b(t) = 1 - \frac{H(t)}{H_0} \tag{1.37}$$

The force was normalised by the maximum value of the force to provide direct access to the proportion values using Eq. 1.29.

To reduce the effect of the uncertainty induced by the experimental noise on force data when the force values were low (a little higher than the order of the rheometer sensitivity), the proportion and the relaxation time of the last Maxwell element c_n and λ_n were first evaluated by a linear regression of $\ln\left(F/\max(F)\right)$ against time, where F can be either the experimental force values or the simulated values. Given that

the regression was performed at the end of the relaxation stage, and given that the relaxation times were at about one order of magnitude from each other, all the Maxwell elements except the last had almost totally relaxed and the bias on the parameters of the last Maxwell element resulting from the linear regression applied to data at long relaxation times was ignored. The conditions minimising this effect and the effects of signal to noise ratio will be discussed in the Results and Discussion section.

The coefficients resulting from linear regression were related to the Maxwell model as follows

$$\lambda_n = -\frac{1}{A} \tag{1.38}$$

$$c_n = \exp(B) \tag{1.39}$$

where A is the slope of the linear regression and B the intercept of the y-axis.

The built-in `fminsearch` function of the Matlab software (The MathWorks, USA) was then used to fit the Maxwell parameters c_i and λ_i, $\forall i \neq n$. On initiating this fitting process step, the values of c_n and λ_n were set to those obtained by the previous linear regression. The proportion of stress $p_i(t_c)$ that did not relax during compression was computed using Eq. 1.33.

A linear piecewise approximation was used to calculate $b(t)$ from experimental compression data.

Eq. 1.31 was used to assess the α_i values using the c_i and p_i values. As the system has an infinite number of solutions, one of the equations was replaced by the constraint

$$\sum_{i=1}^{n} \alpha_i = 1 \tag{1.40}$$

Finally, the elastic shear modulus G was determined at the end of the compression stage, when the maximum amount of stress was reached, using Eq. 1.34:

$$G = -\frac{S_{zz}(t_c)}{3b(t_c)\sum_{i=1}^{n} \alpha_i p_i(t_c)} \tag{1.41}$$

Young's modulus E is written

$$E = 2G\,(1+\nu) \tag{1.42}$$

which, in the case of incompressible materials, reduces to $E = 3G$.

2.4 IMPLEMENTATION OF THE REFERENCE METHOD

It is usually admitted that the Young's modulus can be determined by simple linear regression of stress-strain data, even on viscoelastic materials, so long as the test is carried in the linear region. For such a method, called in the present paper "reference method", Young's modulus E is the slope of the linear regression on the compression stress-strain experimental curve.

In practice, the linear regression was performed using Matlab software; only the last 20 data points of the compression stage were used in order not to take into account the curve of the force-time observed at the beginning of the compression stage. This curve will be presented and discussed further in the Results and Discussion section.

Relaxation is also usually studied in the case described by Eq 1.20 where the compression stage is considered instantaneous. For such a method, called in the present paper "reference method", the modulus proportions are directly estimated from the relaxation stage, *i.e.* $\alpha_i \approx c_i$, whereas the proposed method applies a correction step in order to reach as close as possible the true values of the proportions.

The basic difference between the reference method and the proposed method is therefore that the reference method does not take into account the proportion of stress that relaxed during compression.

2.5 3-D MODELS

In the experiment, despite all the care taken, the upper surface of the sample was not fully parallel to its lower surface. The 0-D analytical model first presented was inappropriate to evaluate the effects of such non-parallelity on determination of the Maxwell model parameters. A 3-D version of the model was therefore implemented using the FEM software COMSOL Multiphysics (COMSOL AB, Sweden). The geometry was half a cylinder with an adjustable angle between the upper and the lower surfaces of the sample, denoted as the inclination (β). The geometry was meshed with 4,790 tetrahedral elements. Computation time depended on the angle between the two surfaces, but did not exceed one hour (Intel Core i5 at 3.1 GHz, 4GB RAM).

The lateral boundary of the domain was left free to move and roller conditions were applied on the upper and the lower surfaces. To take into account the angle of the upper surface of the sample, the following specific downward displacement function was applied to the upper boundary of the domain

$$d(t, r) = -\max\left(0, H_0\left(1 - b(t)\right) - r\tan(\beta)\right) \tag{1.43}$$

where $H_0\left(1 - b(t)\right)$ is the same displacement as that used in the analytical model and r the position along the radius.

Angles were set at 0 (the reference configuration), and 2 degrees (which represented a difference in height of 420 µm between one border of the upper surface and the other).

2.6 SIMULATED DATA SETS

Maxwell model parameters were identified with the two types of method applied separately on force-time data originating from a reference Maxwell material of known (true) values. As such a reference material does not exist, the force-time data of this material was computed. The discrepancy between adjusted and true values was estimated and served as the evaluation of the effectiveness of each method. Effectiveness and uncertainties evaluated from this analysis (see Results and Discussion section) will therefore be applicable in the case of cheese.

2.6.1 *Reference material*

In order to have a reference that was representative of the material under study, the values of the reference material (of known proportions α_i and known relaxation times λ_i) were set at the average values determined on cheese samples when applying the proposed method.

The number of Maxwell elements was set at 5 as it proved to reproduce satisfactorily the mechanical behaviour of cheese under compression-relaxation, and has already been used in the literature for a similar type of cheese (Goh et al. 32, 33, 34). Comparison of the fitting of a typical experimental force-time with 3, 4, and 5 elements is presented in Figure 1.1.

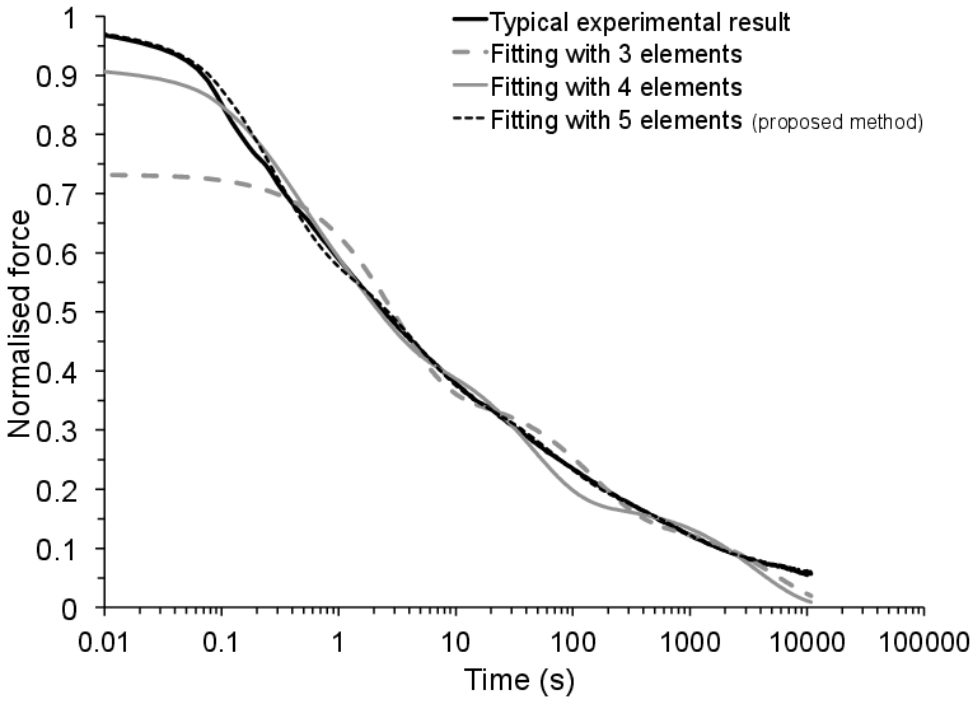

Figure 1.1: Experimental relaxation curve and step responses calculated with 3, 4, and 5 Maxwell elements.

The reference set of entry parameters used for the model can be found in Table 1.1 and Table 1.2. However, it is quoted here for convenience. E was set at 150 kPa; λ_1 to λ_5 were set at 0.15, 3, 40, 600, and 10,000 s, respectively; and α_1 to α_5 were set at 0.58, 0.20, 0.12, 0.07, and 0.03, respectively.

Simulated data sets of force against time were computed (Matlab, The MathWorks, USA) using Eq. 1.11. The geometry used for the force-time computation was close to that used in the experiments: cylinder 6 mm in height and 6.5 mm in radius. When reproducing biases due to the angle of the sample surfaces, the FEM software COMSOL Multiphysics (COMSOL A. B., Sweden) was used to generate the curves. Sampling frequency of the signal was the same as in the experiment. Noise was added to these data; it was normally distributed, with mean 0 and standard deviation 0.002 N. This standard deviation corresponded to the resolution of the rheometer used for the tests. Noise was randomly drawn from this distribution and attributed to the force at each time of measurement. m sets of noised data were developed following this procedure; these sets could be considered as replicates of the same test on the reference material. The set of data without noise was also considered as representative of the case of a highly sensitive rheometer.

2.6.2 *Application of the methods to replicates of simulated solicitation trials and estimation of their effectiveness*

Linear regression of $\ln(F/\max(F))$ against time was applied separately to the m set of noised data in order to estimate c_5 and λ_5. The period of time $[t^{lin}_{start}, t^{lin}_{end}]$ over which linear regression was applied was varied and the optimal pair $[t^{lin}_{start}, t^{lin}_{end}]$ was determined by minimising the error:

$$\sqrt{\left(\frac{\overline{\lambda_5} - \lambda_5}{\lambda_5}\right)^2 + \left(\frac{\sigma_{\lambda_5}}{\overline{\lambda_5}}\right)^2} \tag{1.44}$$

where λ_5 is the true value of the relaxation time of the last Maxwell element, $\overline{\lambda_5}$ the mean value of λ_5 estimated from the m values after linear regression and σ_{λ_5} the associated standard deviation. The same errors were computed for the other parameters (*i.e.* the combination of the systematic error and the random error). When no noise was added to the simulated data (*i.e.* $m = 1$), only the systematic error was considered.

2.7 COMPRESSION-RELAXATION TESTS OF SEMI-HARD CHEESE

2.7.1 *Experimental procedure*

The semi-hard cheeses (7 × 25 × 45 cm of parallelelipedic shape) came from four separate batches produced at an industrial site (four different productions). After their arrival, cheeses were then ripened in temperature-controlled rooms (Grand Cru, Liebherr, France). They were initially stored in a cold room at 12 ± 1°C for 10 days, then stored in a warm room at 20 ± 1 °C for 15 days. The first and second productions were used for the study of the ripening time; the compression-relaxation experiments took place at: 1 day before the change of room, on the day of the room change and 1, 2, and 7 days after the room change for the first production, and 2, 6 and 13 days after the room change for the second production. A new cheese block was used for each compression-relaxation experiment. The effect of the spatial location in the cheese block was studied using he third and fourth productions, the samples were taken 5, 6, 7, and 8 days after the room change.

2.7.2 *Sample preparation*

At a given time of ripening, one cheese was taken from the cold or warm room, unwrapped and two samples were cut from the cheese with a 14 mm diameter cork borer. For the study during ripening, one to two samples were taken from a parallelepiped of 22 × 16 × 1.5 cm^3 at the core of the cheese block. For the study of the location in the cheese block, samples were taken regularly across the width (or x-direction) at the core of the cheese block (± 1 cm in the y- and z-directions). Two samples were taken from each block: one at the core, the other at a given x-position. As four different x-positions were considered, four cheese blocks, at close ripening times, were used.

The cork borer must be used very slowly in order to avoid unwanted permanent strain. A dedicated apparatus operating with two parallel blades (Figure 1.11 in section 4) was then used to cut the upper and lower surfaces of the sample and to ensure the best possible parallelity between the two surfaces.

The initial radius of the sample was measured with a Vernier caliper. Uncertainty on the measurement of the radius was estimated at 0.1 mm due to the softness of the material, although special care was taken not to compress the cylinder when measuring it.

The samples were immediately submerged in a silicone oil bath (at 20 °C) to limit dehydration of the sample during the experiment and to ensure lubricated conditions between the rheometer plates and the cheese sample.

All the experiments were performed at 20 °C. The cheese samples were placed on the lubricated, temperature-controlled Peltier plate and a waiting period of at least 45 min was applied to reach thermal equilibrium in the sample. Thermal equilibrium could also be achieved in a crystallizer before placing it on the Peltier plate. Rheological analysis was started just afterwards.

2.7.3 *Measurement of force-position-time data: compression-relaxation experiment*

The compression-relaxation experiments were performed with a rheometer MCR301 (Anton Paar, Austria). For study during ripening, two distinct rheometers MCR301 were used in order to study two duplicates from the same cheese block at each time of measurement. Each rheometer was equipped with a Teflon Peltier lower plate (diameter 100 mm) and a quartz glass upper plate (diameter 43 mm). The upper plate was placed in contact with the sample, taking care that the resulting force was no greater than 0.02 N, the displacement of the upper plate at that moment being considered as the initial height of the sample (with an accuracy of 0.1 mm corresponding to the irregularity of the sample upper surface). The cross-head speed of the upper plate was set at 3 $mm \cdot s^{-1}$ and deformation was not pursued beyond 10% of the initial height. The

deformation was maintained for 15 h, which represented about 5 times the longest relaxation time of the material. The resulting force and upper plate displacement were measured at the following sampling times: 0.01 s from 0 to the end of the compression stage, 0.06 s from the end of the compression stage to 500 s, 1 s from 500 s to 3,600 s and 60 s from 3,600 s to the end (54,000 s). The force resolution was 0.002 N.

2.7.4 *Validity of the modelling hypotheses and numerical applications*

A typical experimental set of force vs. time is presented in Figure 1.12. For the cheese on which the model was applied (see the last subsection of the Results and Discussion section), no relevant remaining stress was observed after a long period of relaxation (15 h), meaning that the hypothesis of the absence of time-independent elasticity was considered valid.

As the displacement of the upper surface did not exceed 10% of the initial sample height, the theory of small strain could be considered.

Cheese could be considered as incompressible, as demonstrated for hard and semi-hard cheeses (Calzada and Peleg 14). The Poisson's ratio ν was therefore set very near to 0.5 but not equal to 0.5 ($\nu = 0.499$) to avoid indetermination in the 3-D implementation of the model.

As the plates were larger than the sample, the volume of cheese was constant underneath the upper plate throughout the experiment (Engmann et al. 26, Launay and Michon 59).

The lubricated condition at the cheese-plate interfaces allowed us to assume boundary roller conditions at the upper and lower surfaces of the cheese cylinder. The lateral surface of the cylinder remained straight in the experiment.

The samples dimensions were height 6.9 $\pm$ 0.2 mm and radius 6.6 $\pm$ 0.3 mm (standard deviation taking into account both the sensitivity of the measurement method, which was of 0.1 mm, and the reproducibility among 30 samples). These were also small enough to avoid any gradient in composition (water, salts, etc.) within the sample. The thickness of the curd grains was less than 1 mm on average in the final cheese and in the direction of curd pressing. The dimensions of the curd grains in the perpendicular direction (*i.e.* in the radial direction of the samples) were higher (6 mm on average, Huc et al. 44), which was of the same order of magnitude as the diameter of the sample. However, the curd grain has not proved to be the major mechanical structuring element so far, and the mechanical structure governing the compression and relaxation behaviour of the cheese in a small strain approach is probably smaller (*e.g.* at a molecular level). The material was hence considered to be homogeneous throughout the sample. The number and size of bubbles increased at prolonged ripening times, yet the small dimensions of the sample ensured that the samples were free of bubbles, with fixed geometry.

The velocity and acceleration fields were justifiably ignored, due to the relatively slow dynamics involved. Compared with the load applied to the cheese samples, gravity was also ignored.

3

RESULTS AND DISCUSSION

In the first subsection, determination of the parameters of the last Maxwell element by the proposed method was presented. A generalised criterion that could be applied in the study of materials other than cheese was proposed for choosing the time interval on which the regression of $\ln(F/\max(F))$ against time should be performed.

In the second subsection, the sensitivity of the proposed and reference methods to experimental bias (noise, compression time relative to the shortest relaxation, parallelity of sample surfaces) were presented, as well as the resulting overall uncertainty resulting from these methods of identification. This is called the sensitivity study to the experimental protocol of sample preparation and measurement.

In both subsections, the efficacy of the methods was evaluated against simulated sets of force-time data generated for a reference material of known (true) mechanical parameters. Values for these parameters were set close to those of the cheese studied in the third subsection. These sets were synthesised with different operating conditions depending on the subsection, noise being part of these varying conditions. Each condition was varied separately from the other; hence the addition of noise was not combined to the variation of another condition.

In the third subsection, the variations in the Maxwell model parameters of semi-hard cheese during ripening or with the location inside the cheese block and determined with the proposed method were discussed in the light of the overall uncertainty.

3.1 OPTIMISATION OF THE CONDITIONS FOR IDENTIFICATION OF PARAMETERS OF THE LAST MAXWELL ELEMENT WITH THE PROPOSED METHOD

The linear behaviour of the logarithm of the force may be polluted by the relaxation of the other elements and by the decrease in the signal-to-noise ratio. These sources of pollution imply the choice of high values of t_{start}^{lin} so that the contribution of the first Maxwell elements is negligible and low values of t_{end}^{lin} to reduce the effect of noise on the results. The time interval $[t_{start}^{lin}, t_{end}^{lin}]$ was first optimised by adopting a numerical approach.

When the proposed method was applied to simulated data with noise, minimisation of the error defined in Eq. 1.44 led to the optimised time interval $[4,000; 7,500\,s]$. Within that interval, the global error on λ_5 was 7.7% (Table 1.1). With lower (5,000 s) and higher (20,000 s) true values of λ_5, the error was at most 12%. When applied to other materials, it is therefore recommended that the value of t^{lin}_{start} corresponds to at least 3 times the value of λ_4; and that the value of t^{lin}_{end} corresponds to at most twice the value of λ_5.

The true proportion of the last Maxwell element α_5 was found with a 4.4% error (Table 1.1).

The optimised time interval was used in the subsequent sections and 7.7% was retained as the maximum uncertainty for λ_5. Without noise on the force-time data the proposed method provided the true value λ_5 and the true value of α_5 with an error of at most 0.3%.

3.2 ESTIMATION OF THE UNCERTAINTY ASSOCIATED WITH THE PROPOSED METHOD

3.2.1 *Effects of experimental noise*

Applied to the force-time data before the addition of noise, the proposed method (Table 1.1) provided the true values of parameters with less than 0.5% of error whatever the parameter. Even without noise, the reference method presented high levels of error (> 25%) for E, and α_i, explained by the fact that the compression stage is not taken into account in the characterisation of the relaxation step, and vice versa (see the introduction section). Table 1.1 presents the errors computed in Eq. 1.44 depending on the noise level for $t_c = 0.22$ s and $b(t_c) = 0.1$.

In the presence of noise in the force-time data, the proposed method (Table 1.1) provided the true values of all the Maxwell model parameters with a systematic error of at most 8%. The reference method yielded higher levels of error, ranging from about 25 to 45% for E, and α_i (Table 1.1).

Although the Maxwell model parameters determined with the proposed method were still sensitive to the presence of noise (up to 8%, Table 1.1), the step response determined with the proposed method fitted satisfactorily the step response of the reference material (Figure 1.2).

The reference method was less sensitive to the presence of noise (Figure 1.2 and Table 1.1) than the proposed method, but the reference method was in both cases (with and without noise added to the force-time data) not sufficiently accurate to reproduce the reference material step response (Figure 1.2).

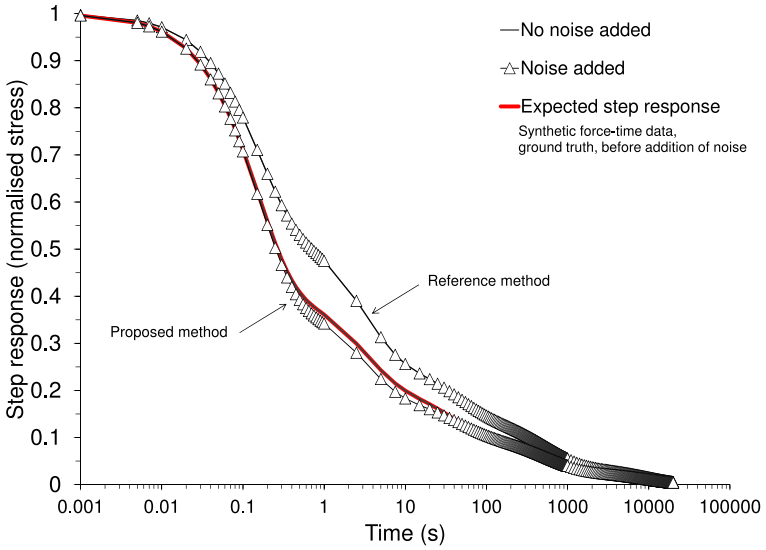

Figure 1.2: Simulated force-time step responses generated from the reference material (see Table 1.1) before the addition of noise, and its comparison with the best adjustment provided by the proposed and the reference methods performed on the force-time simulated dataset for the reference material, with and without noise added.

Table 1.1: Mean values of parameters adjusted by both methods and deviation of the mean values from the expected values on 1000 simulated sets of data (in the case of noise). $t_c = 0.22$ s, $b(t_c) = 0.1$.

		E			α_1			α_2			α_3			α_4			α_5		
noise	method	expected (kPa)	calc (kPa)	error (%)	expected (-)	calc (-)	error (%)	expected (-)	calc (-)	error (%)	expected (-)	calc (-)	error (%)	expected (-)	calc (-)	error (%)	expected (-)	calc (-)	error (%)
0	proposed	150.0	149.9	< 0.1	0.58	0.58	< 0.1	0.20	0.20	< 0.1	0.12	0.11	5.0	0.07	0.07	< 0.1	0.03	0.03	0.3
	reference	150.0	101.1	32.6	0.58	0.42	27.8	0.20	0.27	35.8	0.12	0.17	40.5	0.07	0.10	41	0.03	0.04	41.4
0.002 N	proposed	150.0	149.9	0.4	0.58	0.58	0.2	0.20	0.20	2.8	0.12	0.11	5.2	0.07	0.08	7.3	0.03	0.03	4.4
	reference	150.0	102.4	31.7	0.58	0.42	27.4	0.20	0.27	35.1	0.12	0.08	39.2	0.07	0.11	44.5	0.03	0.04	42.2

	λ_1			λ_2			λ_3			λ_4			λ_5		
noise	expected (s)	calc (s)	error (%)	expected (s)	calc (s)	error (%)	expected (s)	calc (s)	error (%)	expected (s)	calc (s)	error (%)	expected (s)	calc (s)	error (%)
0	0.15	0.15	0.2	3.0	3.0	< 0.1	40.0	40.0	0.1	600	598	0.4	10000	9970	0.3
0.002 N	0.15	0.15	0.5	3.0	3.0	0.3	40.0	40.0	1.0	600	522	12.8	10000	9794	7.7

Table 1.2: Calculated values of parameters adjusted by both methods and deviation from expected values in the simulated data with varying angle (without noise). $t_c = 0.22$ s, $b(t_c) = 0.1$.

		E			α_1			α_2			α_3			α_4			α_5		
angle	method	expected (kPa)	calc (kPa)	error (%)	expected (-)	calc (-)	error (%)	expected (-)	calc (-)	error (%)	expected (-)	calc (-)	error (%)	expected (-)	calc (-)	error (%)	expected (-)	calc (-)	error (%)
0	proposed	150.0	149.9	< 0.1	0.58	0.58	< 0.1	0.20	0.20	< 0.1	0.12	0.11	5.0	0.07	0.07	< 0.1	0.03	0.03	0.3
	reference	150.0	101.1	32.6	0.58	0.42	27.8	0.20	0.27	35.8	0.12	0.17	40.5	0.07	0.10	41	0.03	0.04	41.4
2 deg	proposed	150.0	132.0	12.0	0.58	0.58	0.4	0.20	0.18	7.6	0.12	0.13	8.0	0.07	0.07	3.2	0.03	0.03	0.3
	reference	150.0	110.9	26.1	0.58	0.43	25.4	0.20	0.25	22.7	0.12	0.18	48.9	0.07	0.10	42.7	0.03	0.04	43.9

	λ_1			λ_2			λ_3			λ_4			λ_5		
angle	expected (s)	calc (s)	error (%)	expected (s)	calc (s)	error (%)	expected (s)	calc (s)	error (%)	expected (s)	calc (s)	error (%)	expected (s)	calc (s)	error (%)
0	0.15	0.15	0.2	3.0	3.0	< 0.1	40.0	40.0	0.1	600	598	0.4	10000	9970	0.3
2 deg	0.15	0.15	2.2	3.0	2.6	13.0	40.0	36.1	9.9	644	522	7.3	10000	10078	0.8

3.2.2 *Effects of cross-head speed of the upper plate of the rheometer*

For this study, the same compression conditions applied, *i.e.* $b(t_c) = 0.1$, but t_c varied depending on the compression speeds. As the different sources of uncertainty are combined in the following sections, no noise was added to the simulated data.

In the range of cross-head speed values from 0.05 to 10 mm/s under consideration, the error in the Young's modulus determination did not exceed 0.1% with the proposed method (Figure 1.3) whereas the error in the reference method reached 90%. As expected, the error decreased as the cross-head speed increased, because the amount of stress that relaxed during compression at high speeds was less than the amount of stress that relaxed at low speed. The reference method was appropriate only when the compression time did not exceed one tenth of the true value of λ_1, the error was then lower than 15% in the determination of Young's modulus.

Determination of the relaxation times and proportions with the proposed method was only slightly affected by the cross-head speed of the upper plate of the rheometer (Figure 1.4), with an error of at most 2% even at speed values as low as 0.1 mm/s. The error was less than 0.5% at 3 mm/s, the value retained for the experimental study. In the range of compression times under consideration, the reference method reached errors in the proportions ranging from 67 to 1,000%. The error was at most 42% at 3 mm/s, the value retained for the experimental study. Due to the inertia of the rheometer engine and to the small dimensions of the samples, it can take time to reach high speeds, so that in practice a speed threshold can be observed, and a constant speed during the experiment could not be guaranteed for higher speed values.

When the compression time is greater than about one tenth of the smaller relaxation time of the material (Figure 1.3), a method that takes into account both the compression and the relaxation stages should be used; the usual linear regression on the stress-strain data being inappropriate for determination of Young's modulus.

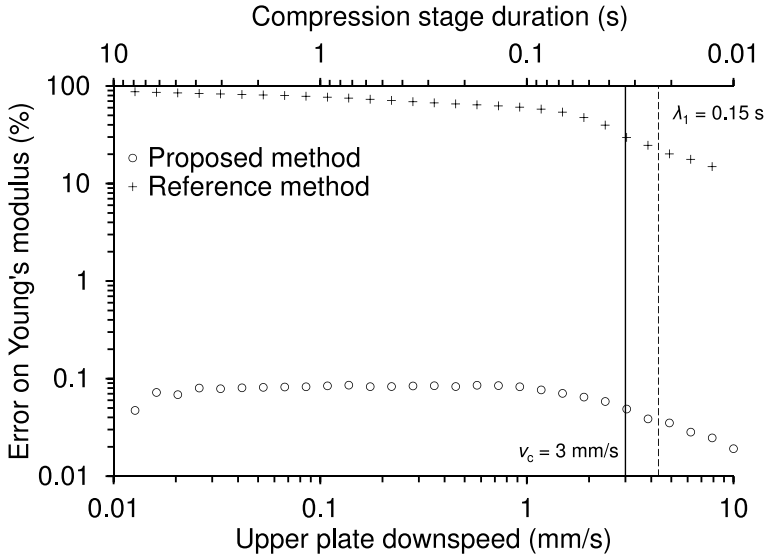

Figure 1.3: Effects of cross-head speed of the upper plate of the rheometer on the determination of Young's modulus with the reference and the proposed methods; errors calculated from Eq. 1.44 using simulated sets of force-time data generated from the reference material without noise (see Table 1.1).

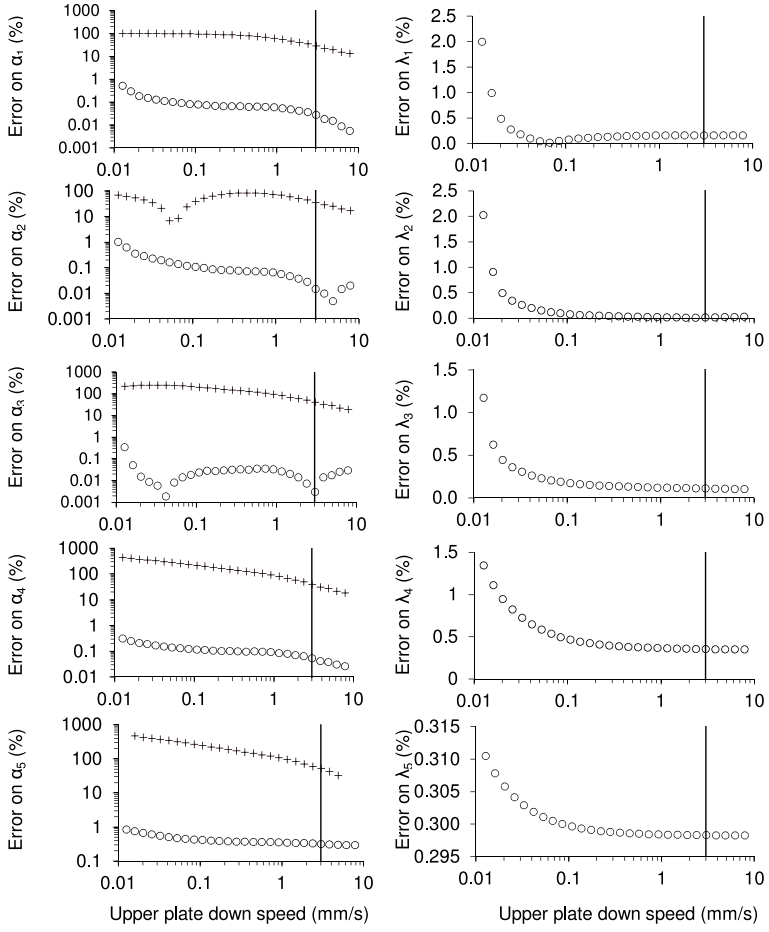

Figure 1.4: Effects of cross-head speed of the upper plate of the rheometer on the relaxation parameters with the reference method (+) and the proposed method (o); errors calculated from Eq. 1.44 using simulated sets of force-time data generated from the reference material without noise (see Table 1.1). Vertical line at 3 mm/s indicates the value retained for the experimental study.

3.2.3 *Effects of non-parallelity between the upper and lower surfaces of the sample*

For this study, the same compression conditions as for the noise study were applied i.e. $t_c = 0.22$ s and $b(t_c) = 0.1$. Simulations of the compression stage with angle of the upper surface of the sample partially explained the experimental concave shape observed in the stress-strain data (Figure 1.5). In reality, imperfections in the surface were probably far from linear with the diameter, the reason why the modelling conditions failed to simulate the experimental behaviour perfectly. When disregarding this discrepancy, it is of note that the experimental concave shape was covered with a maximal angle of 2°. Note that this concave shape was observed in one third of the experiments (over a total of 16 experiments), despite the special care in the preparation of the sample and the development and use of a specific device involving two parallel blades (Figure 1.11).

Two contradictory effects governed the shape of the simulated stress-strain curve. On the one hand, the partial relaxation during the compression stage produced a downward concave stress-strain curve (Figure 1.5, for $\beta = 0°$), on the other hand the non-parallelity produced an upward concave stress-strain curve.

Indeed, the angle of the upper surface of the sample produced a contact surface between the upper plate of the rheometer and the upper surface of the sample that increased as the plate moved downward. The reaction force of the sample increased in the meantime, resulting in an induction period in the force-time curve and an upward concave stress-strain curve, this effect partially compensating for the downward concavity produced by the short relaxation time (see 1 and 2 degree angles in Figure 1.5).

As the linear regression in the reference method was performed on the 20 last force data points, in the domain where the downward concave shape was partly compensated for by the upward concave effect, the reference method yielded better Young's modulus results for $\beta = 2°$ than when the upper and the lower surfaces of the sample were parallel (Figure 1.6): the higher the angle, the more linear the stress-strain data at the end of compression (Figure 1.5). While sensitive to the angle, the proposed method was even better than the reference method, with a maximum error of 12% compared to errors between 26% and 32% with the reference method on the determination of Young's modulus (Table 1.2).

Looking at the relaxation part of the results, the proposed method gave better results than the reference method. The relaxation parameters λ_i were affected by the angle with levels of error reaching about 10-30% for λ_2 and λ_3 and about 1-10% for the other λ_i. Errors in α_i ranged from 0.4% to 19% (Table 1.2) with the proposed method and from 15% to 54% with the reference method.

Moreover, two very distinct types of step response were obtained, depending on the method used (Figure 1.7). The reference method produced step responses that did not fit that of the reference material whereas the proposed method fitted the reference satisfactorily for all three angles. This ensured that the behaviour during relaxation could be reproduced, this despite errors in individual relaxation parameters λ_2 and λ_3, that were at times substantial (Table 1.2).

The angle did not have any relevant effect on the determination of the step responses with either method (Figure 1.7).

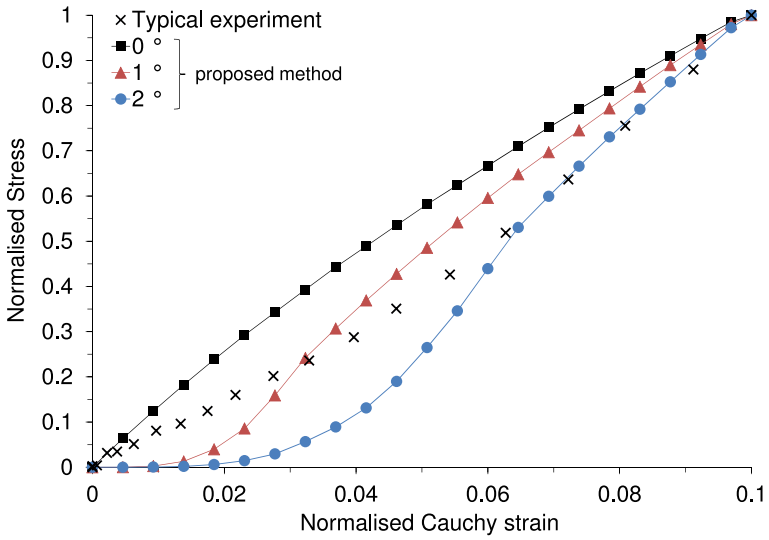

Figure 1.5: Stress-strain curves computed with the reference material (see Table 1.1) with the angle β (0°, 1° and 2°) formed by the upper surface of the sample with the horizontal line; comparison with a typical experimental stress-strain curve from a compression-relaxation test performed on semi-hard cheese.

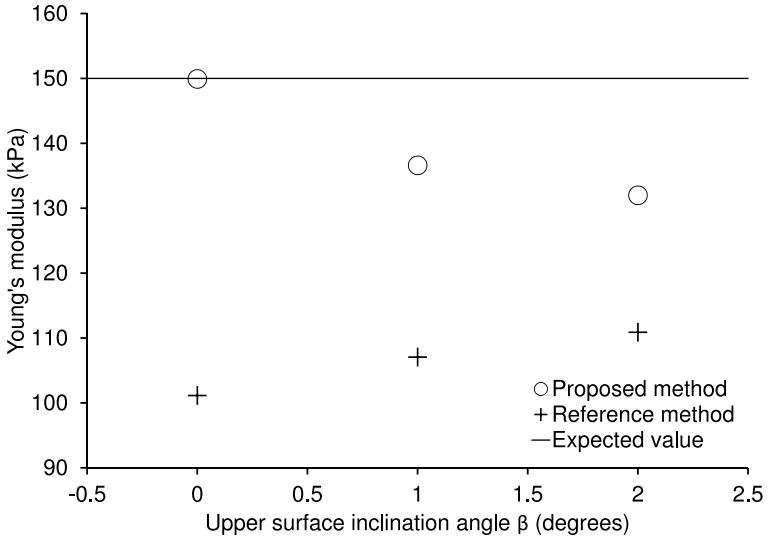

Figure 1.6: Effects of the angle β (0°, 1° and 2°) formed by the upper surface of the sample with the horizontal line,on the determination of the Young's modulus by the proposed and reference methods applied to simulated sets of force-time data generated from the reference material without noise (see Table 1.2). The horizontal line indicates the Young's modulus of the reference material.

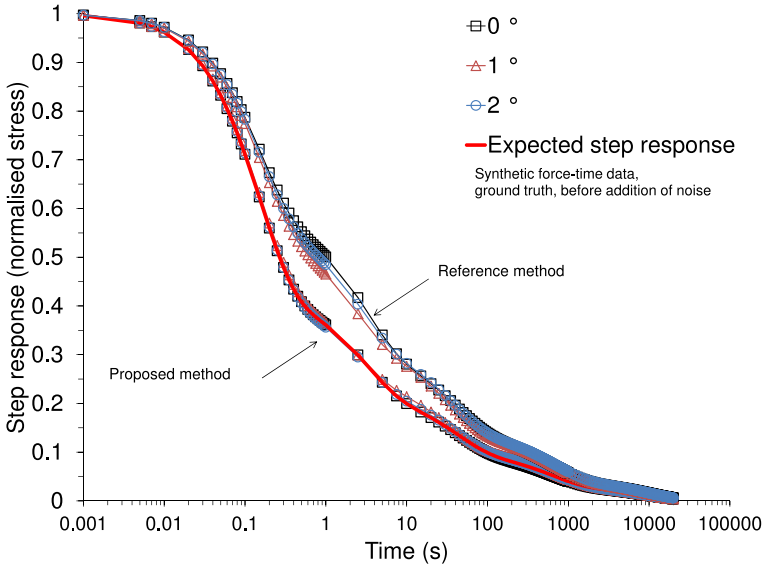

Figure 1.7: Step responses obtained with the proposed and reference methods applied to the step response simulated for the reference material, with noise added. Effects of the angle β (0°, 1° and 2°) formed by the upper surface of the sample with the horizontal line. Solid red line indicates the step response obtained with the reference material parameters.

3.2.4 *Estimation of the overall uncertainty in the determination of the Maxwell model parameters*

The overall uncertainty (u) was calculated as the combination of the previous major sources of error:

$$u = \sqrt{\sum u_k^2} \tag{1.45}$$

where u_k are the errors for each source of error (noise, angle and cross-head speed) and ignoring the possible covariances between them (AFNOR 1999). Since the estimations from the proposed and reference methods were not corrected for systematic errors (see Eq. 1.44), the latter had to be considered as uncertainties.

For the numerical application, the worst case was considered as a combination of the errors due to:

- the presence of noise in the force-time experimental data (Table 1.1) (0.002 N in standard deviation);
- the lowest cross-head speed of the upper plate of 0.05 mm/s;
- the highest angle of 2 degrees between the upper and lower sides of the samples.

The overall values of uncertainties and the contributions of the different sources of uncertainties are shown in Table 1.3. For the proposed method, the most likely contributing source of uncertainty was the non-parallelity of surfaces in the sample; for the reference method, it was the speed of the upper plate (although the reference method also remained fairly affected by the angle of the surfaces).

Table 1.3: Overall uncertainty for the Maxwell parameters determined by the proposed and reference methods; contributions of the different sources of uncertainty tested in the sensitivity study to the experimental protocol of sample preparation and measurement.

parameter		E		α_1		α_2		α_3		α_4		α_5	
method		reference	proposed	reference	proposed	reference	proposed	reference	proposed	reference	proposed	reference	proposed
overall uncertainty (%)		96.4	12.0	105.3	0.7	79.4	8.2	224.7	9.5	444.0	8.0	468.8	6.1
explained by (%)	noise	21.9	2.9	18.1	22.3	28.0	24.8	12.9	38.2	8.4	67.3	7.7	47.6
	angle	18.0	96.7	16.8	32.8	18.1	66.4	16.1	59.3	8.1	29.8	8.0	43.4
	low speed	60.1	0.4	65.1	44.9	53.9	8.8	71.0	2.5	83.5	2.9	84.3	9.0

parameter		λ_1	λ_2	λ_3	λ_4	λ_5
overall uncertainty (%)		3.0	13.2	10.0	14.8	7.8
explained by (%)	noise	10.6	1.8	8.3	59.8	87.6
	angle	47.4	85.0	82.0	33.9	8.8
	low speed	42.0	13.2	9.7	6.3	3.6

These uncertainties are discussed with the results on cheese and characterization of an effect of ripening time and location of samples in the cheese block.

3.3 APPLICATION TO SEMI-HARD CHEESE

Determination of Young's modulus yielded results in the same order of magnitude as the results found in the literature for similar cheeses. Del Nobile et al. [24] found a Young's modulus of 102 kPa for ripened cheese, whereas it was 140 to 240 kPa for Swiss-type cheese (Rohm and Lederer 81), and up to 600 kPa for Cheddar (Goh et al. 34).

In the few studies on relaxation, relaxation times were fixed a priori, with one decade between each element, ranging from 0.1 to 1000 s (Goh et al. 32, 33, 34). The number of elements used in this study as well as the order of magnitude of the parameter values corresponded to those found in our study.

3.3.1 *Effects of ripening on the viscoelastic parameters of the Maxwell model*

Figures 1.8 and 1.9 present the evolution of Young's modulus and relaxation parameters during ripening, respectively. The error bars correspond to the overall uncertainty of the proposed method (see previous section).

Variability between the duplicates (easily noticeable for the Young's modulus in Figure 1.8) might be explained by spatial variability in the rectangular slice (14 × 17 × 1.5 cm) extracted from the core of the cheese block and used for sampling. It should be remembered that the dimensions of the sampling area were imposed by the presence of bubbles in the cheese from which the sample was taken. Variability in Young's modulus between batches included this spatial variability, and obviously variability in the milk composition and/or in the cheesemaking process.

In view of the variability between the samples (experimental variability), the parameters did not evolve in a significant way during ripening (Table 1.4). Under these conditions, no effect of ripening time could be detected; Young's modulus was on average 162 ± 39 kPa (overall uncertainty due to the method, sample location and batches).

Table 1.4: Average values of Maxwell parameters (as if there was no effect of the ripening time) determined by the proposed method on experimental data obtained from core samples of semi-hard cheese, overall uncertainties and contributions of the different sources of uncertainty. The variability in the sampling location (different between duplicates at a given day of ripening, different between days of sampling also), the cheese making (two productions were used) and the rheometer used (one for each duplicate) were of experimental nature (refer to the text for more details).

Parameter		E	α_1	α_2	α_3	α_4	α_5	λ_1	λ_2	λ_3	λ_4	λ_5
Mean experimental value		162 kPa	0.54	0.21	0.13	0.07	0.03	0.15 s	3 s	39 s	577 s	6750 s
Overall uncertainty (%)		24.1	8.5	17.7	20.0	16.4	30.7	22.9	33.9	45.7	40.1	34.5
Explained by (%)	Experimental variability	63.5	92.7	65.7	64.9	64.2	83.2	88.2	70.4	81.7	71.6	81.3
	Method	36.5	7.3	34.3	35.1	35.8	16.8	11.8	29.6	18.3	28.4	18.7

A slight decrease in high relaxation times (with the ripening time) was noticeable. However, at that stage it was impossible to discuss the impact of such a decrease on consumer perception or on bubble growth without knowing the sensitivity to such parameters.

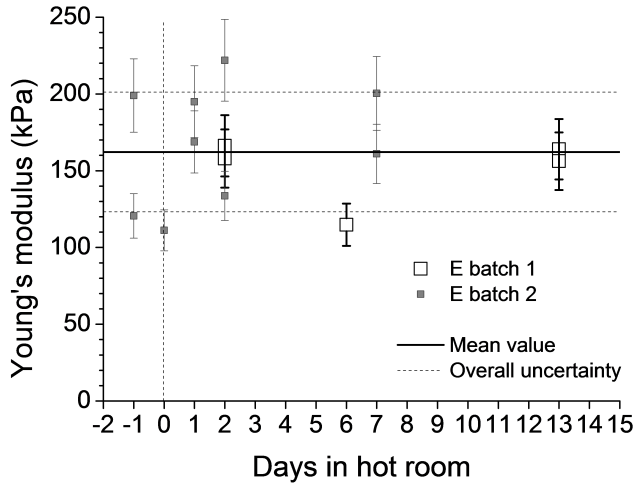

Figure 1.8: Evolution of Young's modulus at core of cheese block during ripening. The error bar is the overall uncertainty due to the proposed method. Vertical lines at $d = 0$ denote the change in room temperature. The horizontal plain and dotted lines represent the mean value calculated over all values and the overall uncertainty (see values in Table 1.4).

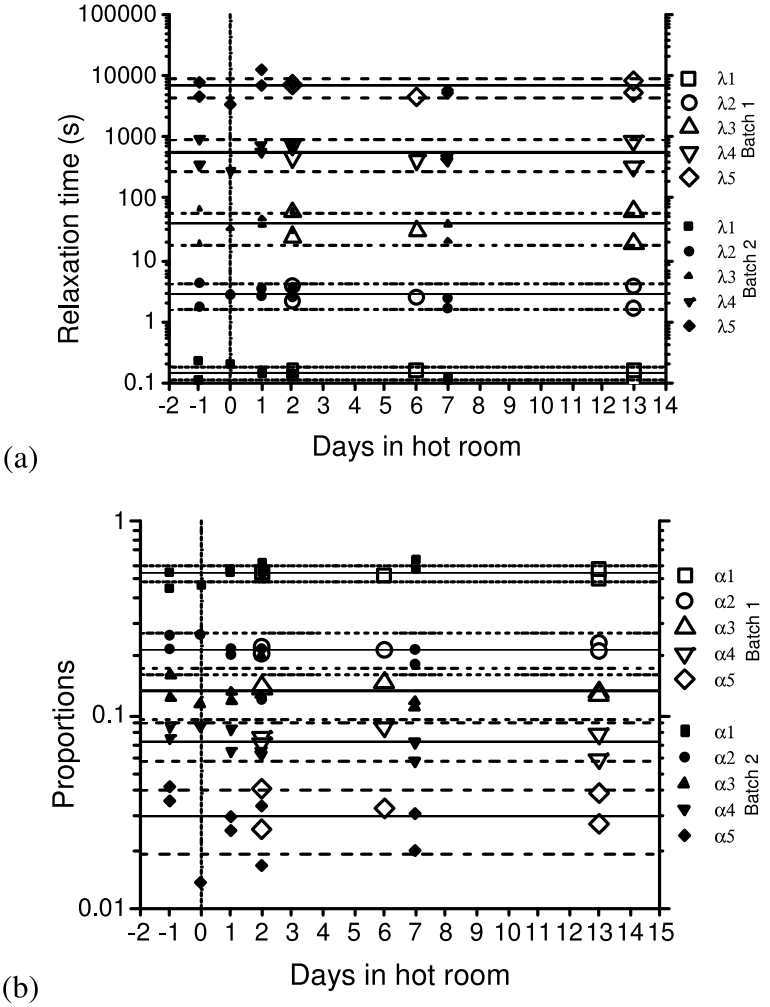

Figure 1.9: Evolution of relaxation times (a) and proportions (b) of core samples of cheese material during ripening (vertical line at $d = 0$ refers to change from cold to warm storage rooms). The horizontal plain and dotted lines represent the mean value calculated over all values and the overall uncertainty (see values in Table 1.4).

3.3.2 *Effects of location in the cheese block on the Maxwell model viscoelastic parameters*

The location of the samples taken from a border to the core along an axis is indicated in Figure 1.13. Differences in mechanical behaviour (Figure 1.10) were found between the samples located near the surface of the cheese block (lower x-values) and the samples from the core (higher x-values). Young's modulus values presented a steep gradient within an area 3 to 4 cm beneath the block surface (Figure 1.10a), the values near the surface of the cheese block being roughly twice as high as the values in the core. For higher x-values (*i.e.* $x > 4$ cm), the difference between the Young's modulus values proved to be of the same order of magnitude as the variability between batches. Young's modulus could thus be considered homogeneous in the $x > 4$ cm area.

However, the stress relaxed more quickly in the core than near the surface of the cheese block (Figure 1.10b).

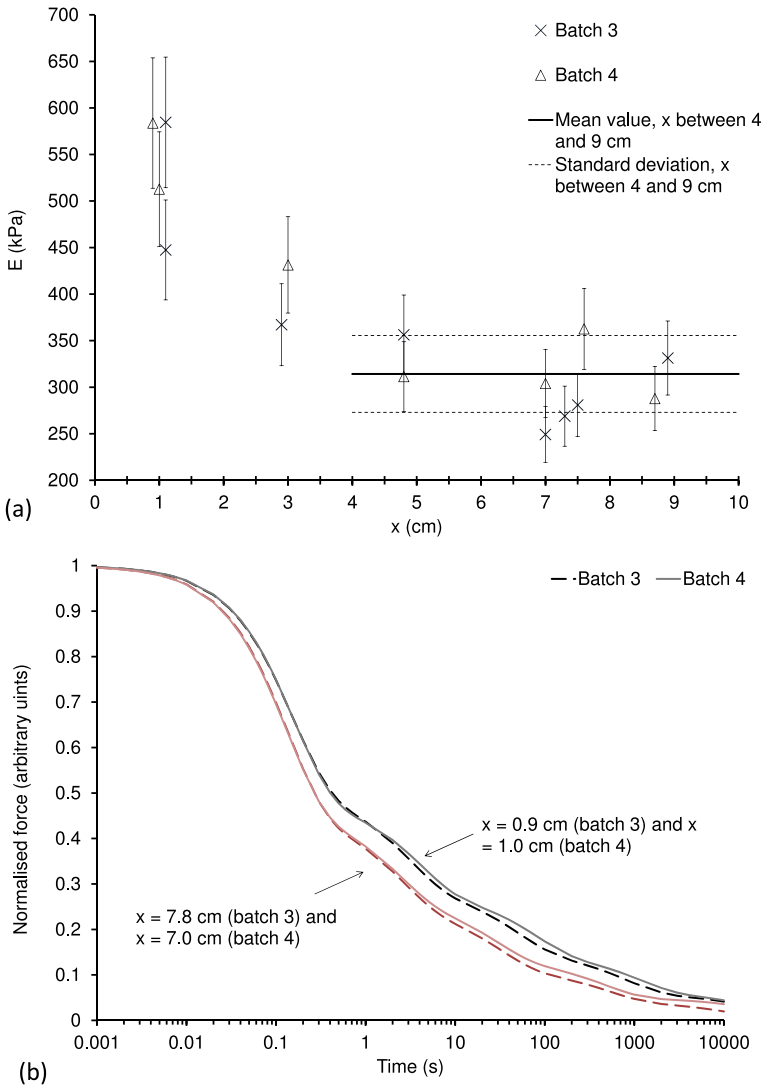

Figure 1.10: Effects of x-position in the cheese block on (a) Young's modulus, and (b) step responses. The error bar in (a) is the overall uncertainty due to the proposed method. The horizontal plain and dotted lines in (a) represent the mean value calculated over all values for $4 \leq x \leq 9$cm and the overall uncertainty (experimental variability and uncertainty produced by the identification method).

4

CONCLUSION

When dealing with viscoelastic materials that can relax part of the stress quickly, special care must be taken in the method used to determine the rheological properties of the material. The usual methods applied to a compression-relaxation test based on a generalised Maxwell model might be inappropriate to estimate the parameters of such a model and might lead to considerable errors, even in Young's modulus. Depending on the parameter and on the error sources, the error can reach several times the expected values (up to 6 times).

A software-independent method still involving the generalised Maxwell model was proposed to identify the stress relaxed during the compression stage and to minimise these errors. The accuracy of the proposed method was analysed through the three major sources of uncertainty in the uniaxial compression-relaxation experiment. The following recommendations were established, and constitute major outcomes of this study.

In order to avoid the beginning of the relaxation in the compression stage, the strain should be applied over a significantly shorter time than the shortest of the relaxation times of the material. However, although it can be considered theoretically that the higher the speed, the better the estimation, in practice high speeds can cause several experimental issues. The criterion of a compression stage that lasts at most one tenth of the smallest relaxation time was proposed. Under such conditions, errors produced by the reference method were minimized but still high; 15% for E, 12 to 20% for the proportions associated with the relaxation times. On the other hand, the proposed method makes it possible to envisage a wide variety of experimental conditions (from 0.05 to 10 mm/s) for the assessment of Maxwell model parameters (machines used, sample dimensions, etc.) with very low levels of error (at most 2%). The step responses were also better reproduced than with the reference method.

When preparing experimental samples, care should be taken to make sure that the upper and lower surfaces of the sample in contact with the rheometer plates are as parallel as possible. Although the proposed method is sensitive to the non-parallelity of the upper and lower surfaces of the sample, the study showed the ability to reproduce the behaviour of an ideal Maxwell material satisfactorily. For an angle of the upper surface of the sample in relation to the rheometer plate of 2°, E and the parameters from the 2^{d} and 3^{d} elements were estimated with less than 13% error, and parameters from the 1^{st}, 4^{th} and 5^{th} elements with less than 8%. A specific device that operates two blades was also proposed, limiting the effects of non-parallelity of surfaces in two thirds of the trials.

Finally, the proposed method was applied to the characterisation of the rheological behaviour of a semi-hard cheese. The study showed that *(i)* the adequacy of the Maxwell model was appropriate for modelling the mechanical behaviour of cheese, *(ii)* the proposed method of parameter identification was sufficiently accurate to describe the product, its uncertainties in relation to the spatial variability of the samples from the surface of the cheese block and its centre being negligible. It also showed that with regard to the overall uncertainties of measurement and reproducibility, the viscoelastic properties of the semi-hard cheese sampled at the centre of the block studied did not evolve significantly during ripening. This was considered as a non-negligible result in regard of the current knowledge on viscoelastic properties of cheeses.

Lastly, this study showed higher values of Young's modulus (two times higher) and slower relaxation in the outer layers of the cheese block than at core. Similar mechanical properties were reported in an area comprised between the mid-width to the core, for the tested direction.

ACKNOWLEDGMENTS

The authors wish to thank Anthony Hutin, Julien Mottet, Gabrielle Moulin and Michel Loubat for technical assistance. This study was carried out with financial support from VALORIAL and the Regional Councils of Bretagne, Pays de Loire and Basse-Normandie. First author, Yannick Laridon, is the holder of a grant from INRA and Irstea.

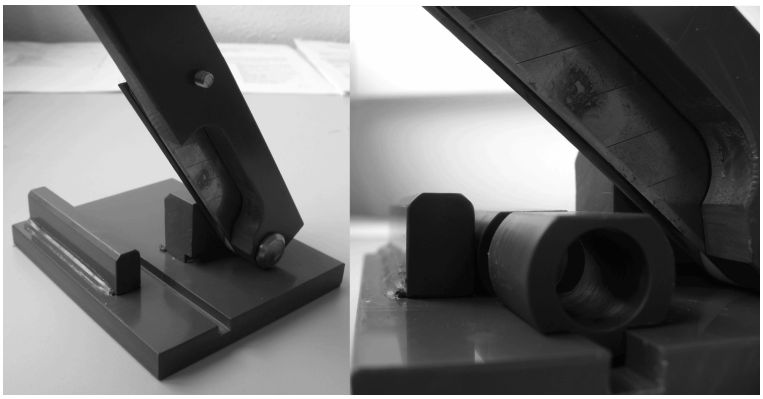

Figure 1.11: Experimental set-up for cutting the samples. The boring cylinder was placed inside the cylinder to avoid strain when lowering the blades.

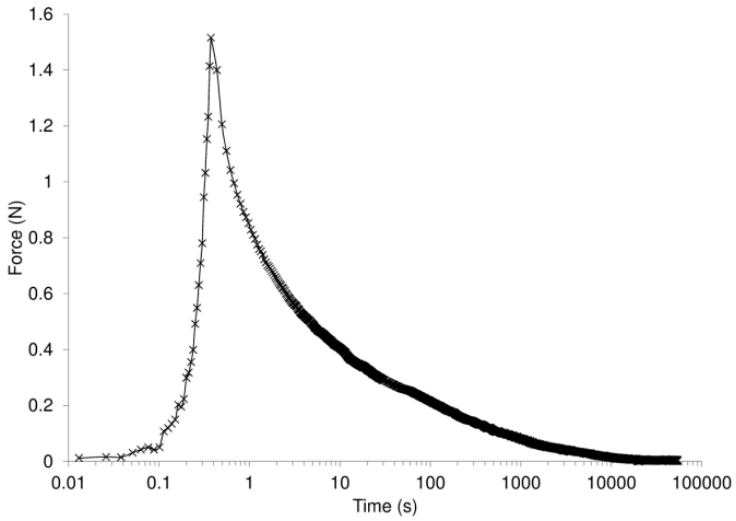

Figure 1.12: Typical experimental force-time curve from a compression-relaxation test performed on a semi-hard cheese sample.

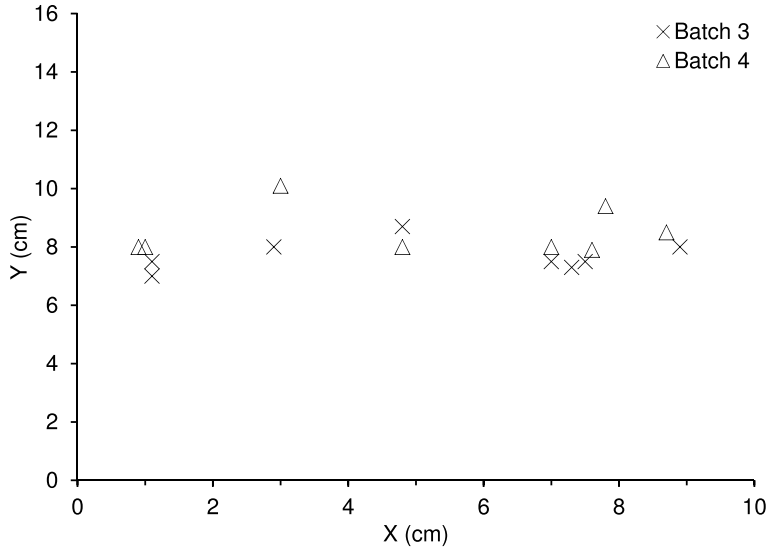

Figure 1.13: Location of samples in the cheese block. The XY plane is located at the middle of the cheese block height.

Chapitre 2

MONITORING A SINGLE EYE GROWTH UNDER KNOWN GAS PRESSURE: MRI MEASUREMENTS AND TEACHINGS ABOUT THE MECHANICAL BEHAVIOUR OF A SEMI-HARD CHEESE

A dedicated setup was developed to measure both pressure and volume simultaneously in a single eye within a cylinder of semi-hard cheese. Air pressure was applied within the cheese eye and the resulting eye inflation was monitored using Magnetic Resonance Imaging (MRI). Image analysis methods were developed not only to measure the eye volume but also the horizontal and vertical diameters of the eye and the upside deflected shape of the cylinder of cheese. The uncertainty on each parameter was estimated. Two amounts of pressure were applied so to attempt to reproduce a creep-recovery experiment in situ. In a last stage, a lowering in pressure was applied in order to discuss a time-independent elasticity. The core of the semi-hard cheese under processing was found to show no relevant time-independent elasticity on a 90 h experiment. Low amount of pressure (< 3.5 kPa), together with slow pressure variations, was found to be able to inflate eyes in semi-hard cheese within the linear domain.
Keywords: creep-recovery; viscoelasticity

1 INTRODUCTION

Bubble growth results from the balance between the increase in gas amount within the bubble (Huc et al. 47) and the mechanical resistance the surrounding cheese opposes to this increase (Laridon et al. [58]). Understanding of cheese mechanics, and the way it reacts to the formation of a gas bubble, is of importance in mastering semi-hard cheese processing because it determines whether to focus on gas production, mechanical properties or a mix of them (Huc et al. 47).

A first step in understanding gas formation in cheese is to monitor the growth of bubbles. The formation of a single bubble and its displacement in a fluid has been studied in either boiling water (Lee et al. 60) or in a molten silica (Mourtada-Bonnefoi and Mader 67, Minami et al. 66) using a high speed camera. The transparent nature of the fluids studied allowed such monitoring, while the high levels of displacement involved in these studies required quite high time frequencies. These conditions are far from thoses involved in the growth of a single bubble in cheese for which bubble motion is slow, and occurs in an opaque medium.

The advances in imaging techniques make it possible to measure bubble volume or displacements continuously in opaque media. The visualisation of a swarm of bubbles in cheese has recently been carried out using X-Ray tomography and MRI in order to evaluate the effect of cheese formulation and processing conditions (Guggisberg et al. 38, Kraggerud et al. 55, Musse et al. 68, Schuetz et al. 83). Bubbles within Gouda cheese of round shape (13.7 cm in diameter and 6.9 cm in height) have been observed with an acquisition time of 28 s using X-ray tomography with a slice thickness of 1 mm and a Field of View of 180 mm (Lee et al. 61). Spatial resolution of 1 mm^3 has been used in parallelepipeds of cheese of 48 cm × 24 cm × 10 cm in dimensions so to assess accurate bubble distributions with an acquisition time of 51 min by MRI (Musse et al. 68). Other techniques such as ultra-sound make it also possible to assess defaults in cheese (Conde et al. 20, Eskelinen et al. 27). However, this technique only reveal the presence or defaults and cannot be used to appropriately monitor the growth of a single bubble for the purpose of discussing mechanics in cheese.

Since the way a material reacts to a mechanical load (gas pressure) depends on the magnitude and the speed at which the load is applied, both volume and pressure measurements, performed simultaneously, are needed to understand the gas expansion. The bubble volume is required to monitor the strain and strain rate, and pressure to evaluate how much resistance is opposed to gas inflation.

In polymer science, Yano and Shimiya [94] monitored pressure and droplet volume simultaneously in order to predict the critical radius of a bubble to shrink at a constant temperature. A droplet of paraffin oil was blown up inside a gelatine gel and pressure was measured using a mercury barometer. The volume was measured photographically, since the medium was transparent. In cheese, known gas pressure was applied in an bubble of Emmental cheese with the use of a needle which basement was glued to insure tightness between the needle and the cheese, but, bubble inflation was only non-continuously and destructively evaluated by slicing cheeses from different batches (Fluckiger et al. 30). No discussion about the relation between the gas pressure and the volume of the bubble was developed. Blowing up a bubble with pressure measurements using an alveograph is a widespread technique used in studying how a bubble would behave during bread making (Codina et al. 19). Apart from these few studies, the growth of an individual bubble under a known gas pressure has poorly been investigated so far and never with the use of imaging techniques in cheese.

In this study, a dedicated setup was developed to sustain a single round bubble within a small cheese cylinder taken from a cheese block under ripening. Special attention was paid to insure a good contact between the cheese and the lateral faces of the sustaining apparatus. The upper surface of the cheese cylinder was let free to move. A level of gas pressure at the bubble-cheese interface was set by gas compression. Pressure and volume in the bubble were monitored continuously. The first objective was to present the methods used for measuring the bubble volume, the horizontal and the vertical bubble radii and the upper surface deflected shape. The expanded standard uncertainties associated with these measurements were estimated. The aim was also to discuss the viscoelastic response in a semi-hard cheese to a solicitation similar to that actually found in an bubble within a semi-hard cheese block during ripening. To do so, three mechanical solicitations were applied; a creep, a recovery and a lowering in pressure.

2 MATERIAL AND METHODS

2.1 CHEESE

A semi-hard cheese block (parallelepiped, length 47 cm, width 23.5 cm, height 9 cm) (Figure 2.1) was picked up from a production batch at the plant and was sent to the laboratory in its foil. The cheese block was ripened for 9 days in a temperature controlled cabinet (Grand Cru, Liebherr, France).

2.2 SAMPLE PREPARATION

On day 9, a Magnetic Resonance Imager (MRI) (Avanto 1.5 T, Siemens, Germany) was used to locate a single bubble surrounded by a volume of plain cheese inside the block of cheese (Figure 2.1a). After being located, the bubble (1) (Figure 2.1b) was extracted from the block of cheese within a cylinder of cheese (54.4 ± 0.15 mm in diameter and 32.3 ± 0.15 mm in height) with the help of a stainless tube (device not shown). The center of the bubble (10.9 ± 0.5 mm in diameter) was set to be as close as possible to the axis of symmetry of the removed cylinder of cheese.

The upper surface (3) of the cylinder of cheese was carefully sliced with a steel wire so to make it as plane as possible and also to adjust the distance of the bubble from the upper surface (3.85 ± 0.85 mm).

The cylinder of cheese was put inside a sustaining apparatus (4) made of plastic (Figure 2.1b). In order to avoid too much stress to appear within the cylinder of cheese when put inside the sustaining apparatus, several sizes of sustaining apparatus were manufactured so to choose the one that best fitted the size of the cylinder of cheese. Without taking this precaution it was quite impossible to appropriately match the size of the cylinder of cheese with that of the sustaining apparatus. Before the beginning of the bubble growth experiment the cheese was let three hours, free of load, in the sustaining apparatus in order to let the possible remaining stress to relax.

The top part (5) of the sustaining apparatus prevented the lateral boundaries of the cylinder of cheese from moving upward. A cap (6) allowed the cheese upper surface not to dry during the experiment. Pressure equilibrium between the gas chamber (7) above the cheese and the atmospheric pressure was insured by a very small hole (8) in the cap. A needle (9), inserted into the bubble on one side and connected to the injection device on the other side (Figure 2.1b), made it possible to increase air

pressure within the bubble. The needle was inserted into the middle of a thread rod (Figure 2.1b) which was screwed into the cheese so to insure as tightness as possible. Indeed, while screwing the thread rod, a cheese cone (10) (Figure 2.1b) was formed at the top of it so the cheese material was squeezed between the rod and the needle so limiting air leaks.

Another cylinder of cheese was extracted from the cheese block symmetrically to the first cylinder (water content Day 9 Figure 2.1a) in order to check up on water distribution at the beginning of the experiment. Figure 2.1.

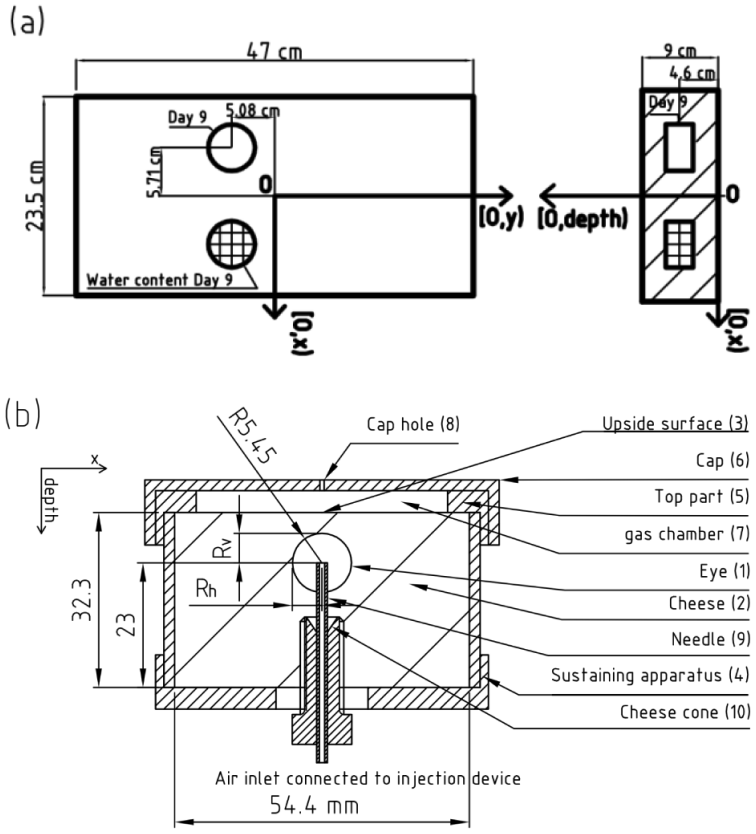

Figure 2.1: Experimental device for the bubble growth experiment. (a) Locations of the cylinders of cheese sampled in the cheese block and used for bubble growth experiment and for water content analysis. The 32 samples used for the analysis of the gradient of water content can be seen using the left and right hand side drawings (the lattices) (b) Cylinder of cheese in its sustaining apparatus. The height of the cylinder of cheese is in the $(O, depth)$ direction of the larger cheese block and the width of the cylinder of cheese is in the (O, x) direction.

2.3 EXPERIMENTAL PROCEDURE

The sustaining apparatus was placed into the knee antenna of the MRI scanner once for all. The experiment of bubble growth was carried out at the ripening temperature (20 ± 1°C) within and around the MRI scanner.

A 3D (300) MRI sequence (see section 2.4.3) was launched before gas pressure was increased in the bubble, in order to measure the upper deflected shape of the cheese cylinder as well as the initial volume and radii of the bubble which may have evolved since the extraction of the cylinder from the cheese block. Three main solicitations were then applied; the creep, the recovery and the lowering in pressure (Figure 2.6):

The creep consisted of different pressure levels (the gray number in Figure 2.6b, c, d), with $P > 0$, P being the relative pressure of the gas in the bubble to the atmospheric pressure;

1. at 0 min, air was injected into the injection device producing a steep increase in pressure in the bubble from 0 up to 7.5 ± 0.3 kPa, and followed by a slight decrease in pressure down to 6 ± 0.3 kPa, (from 0 to 40 min);

2. at 41 min, a steep drop in pressure from 6 ± 0.3 kPa to 3.5 ± 0.3 kPa;

3. from 41 min to 700 min, a constant load with slight and slow linear decrease in pressure from 3.5 ± 0.3 kPa to 2.8 ± 0.3 kPa;

4. at 701 min, a sudden drop in pressure from 2.8 ± 0.3 kPa to 2 ± 0.3 kPa followed by a constant pressure of 2 ± 0.3 kPa (from 701 min to 901 min);

5. the recovery, from 901 min to 4,350 min, consisted of a return to the atmospheric pressure (0 ± 0.3 kPa), $P = 0$;

6. the lowering in pressure, from 4,351 min to 5,300 min, consisted of a slight and sudden decrease in pressure (- 1.4 ± 0.3 kPa) followed by a slow increase in pressure up to the atmospheric pressure, $P < 0$.

A series of six 2D (240) and one 3D (500) sequences was repeatedly launched. At 900 min and 5170 min, a 3D (300) MRI sequence was launched to assess the volume, radii and upper deflected shape with higher accuracy.

2.4 METHODS OF MEASUREMENT

2.4.1 *Water content*

The water content at the beginning of the experiment was measured on the cylinder called "water content Day 9" coming from the same cheese block as that used for the bubble growth experiment (Figure 2.1a). The cylinders were cut horizontally into two slices, and then into 16 small blocks as presented in Figure 2.1a (the lattices in the circle and rectangle representing the water content cylinder). The 32 small blocks were weighed before and after being oven-dried at 104 ± 1°C for 24 h. The water content x_w was calculated.

2.4.2 *Gas pressure measurements within the bubble*

Gas pressure was measured inside an injection device with a calibrated absolute pressure transducer (XCEL-100-25A, Kulite, USA). The injection device was connected to the air inlet of the needle. The acquisition frequency of the pressure measurement was 1 Hz with an adequate resolution on an Ahlborn data logger (Almemo 2590, Ahlborn, Germany). Daily variations in atmospheric pressure inside the laboratory during the experiment were of the same order as the applied gas pressure in the bubble. The atmospheric pressure was recorded using an outside barometer (La Crosse Technology, WS3500, France). The gas pressure in the bubble, denoted earlier as P, relative to the atmospheric pressure inside the laboratory was considered in the present study (Eq. 2.1).

$$P = P_{transducer} - P_A \tag{2.1}$$

where $P_{transducer}$ was the pressure measured by the pressure transducer. The expanded standard uncertainty on gas pressure measurement was estimated following the directions made by the Joint Committee for Guides in Metrology [49]. According to Eq. 2.1 and to standards, the combined standard uncertainty on pressure measurement, $u_c(P)$, was estimated at 0.15 kPa, Eq. 2.2.

$$u_c(P) = \sqrt{u(P_{transducer})^2 + u(P_A)^2} \tag{2.2}$$

with null covariance between the two variables and with

$$u(P_{transducer}) = \sqrt{u_s^2 + u_c^2 + u_r^2} \tag{2.3}$$

where

- $u_S$was due to instabilities in the voltage supplied to the pressure transducer. It was estimated at 0.068 kPa;

- $u_c$was the standard uncertainty on the pressure transducer measurement, estimated with the help of a calibration device developed at the lab. It was estimated at 0.058 kPa;
- $u_T$was due to the sinusoidal temperature variation in the air surrounding the injection device. This uncertainty was estimated at 0.12 kPa;
- $u_{P_A}$was the standard uncertainty on the measurement of the atmospheric pressure, estimated at 0.014 kPa.

These standard uncertainties were estimated based on the premise they behaved symmetrically and uniformly (except for temperature for which an arcsine distribution was considered). They were estimated from the full amplitude of uncertainty (a), Eq. 2.4.

$$u_i(x) = \frac{a_i}{2\sqrt{3}} \tag{2.4}$$

where i is a given source of uncertainty on the variable x. Variations in air temperature contributed to 80% of the combined standard uncertainty. Special care was so given not to have too much temperature fluctuations around the injection device by adjusting the thermostat setting. As the distribution laws of the uncertainties were considered as well known, the resulting combined standard uncertainty, $u_c(P)$, was multiplied by a factor of two so as to obtain the expanded uncertainty as recommended by standards. The resulting expanded uncertainty on pressure measurement $u(P)$ was 0.3 kPa.

2.4.3 *MRI measurements*

Based on the work of Musse et al. 68, three specific Spin Echo sequences were set up to measure the volume, radii and the upper deflected shape of the cylinder of cheese, with either a good spatial resolution or a good time resolution.

3D (300)

Time of echo (TE) of 12 ms, Time of repetition (TR) of 400 ms, Echo Train Length (ETL) of 6, bandwidth = 296 Hz, 1 scan, voxel size = 0.3$\times$ 0.3 $\times$ 0.3 mm^3, 88 slices (images to be processed), Signal Noise Ratio = 27, acquisition time 1 h 08 min.

3D (500)

Time of echo (TE) of 10 ms, Time of repetition (TR) of 400 ms, Echo Train Length (ETL) of 6, bandwidth = 296 Hz, 1 scan, voxel size = 0.5$\times$ 0.5 $\times$ 0.5 mm^3, 52 slices (images to be processed), Signal Noise Ratio = 53, acquisition time 8 min 45 s.

2D (240)

Time of echo (TE) of 13 ms, Time of repetition (TR) of 400 ms, bandwidth = 296 Hz, 2 scans, pixel size = 0.24 mm², slice thickness 4 mm (image to be processed), acquisition time 2 min 47 s.

2.5 IMAGE AND DATA ANALYSIS

2.5.1 *Bubble volume*

The bubble volume V_b was obtained from the images of 3D sequences only, by adding all the voxels (elementary volumes) of low signal selected after image thresholding using Otsu's method (Otsu 71). At the place of the thread rod, voxels were also of null intensity, hence the thread rod was masked not to overestimate the number of voxels belonging to the bubble (Figure 2.2c).

The application of a threshold for isolating the bubble from the cheese bulk resulted in the omission of voxels of partial volume, leading to a systematic underestimation of the bubble volume. The cheese-bubble interface was resolved by two voxels maximum. The underestimation along each radius R could not exceed the dimension of one pixel; this extreme configuration was retained for the estimation of the volume uncertainty.

The standard uncertainty due to partial volume was evaluated assuming a normal distribution, Eq. 2.5.

$$u_{partialV}(V_b) = \frac{\frac{4}{3}\pi\left((R+\Delta x)^3 - R^3\right)}{2\times 3} \tag{2.5}$$

where Δx was the voxel size, respectively 0.3 mm and 0.5 mm for 3D (300) and 3D (500) sequences.

High levels for the echo strength length may provoke some geometrical distortions; however the comparison between the bubble volumes determined on the same cheese blocks using MRI and X-Ray images showed good agreement (Musse et al. 68) and hence no additional bias was taken into account.

The expanded standard uncertainties associated with the methods for determining the bubble volume (for an bubble radius of 5.45 mm) are presented in Table 2.1.

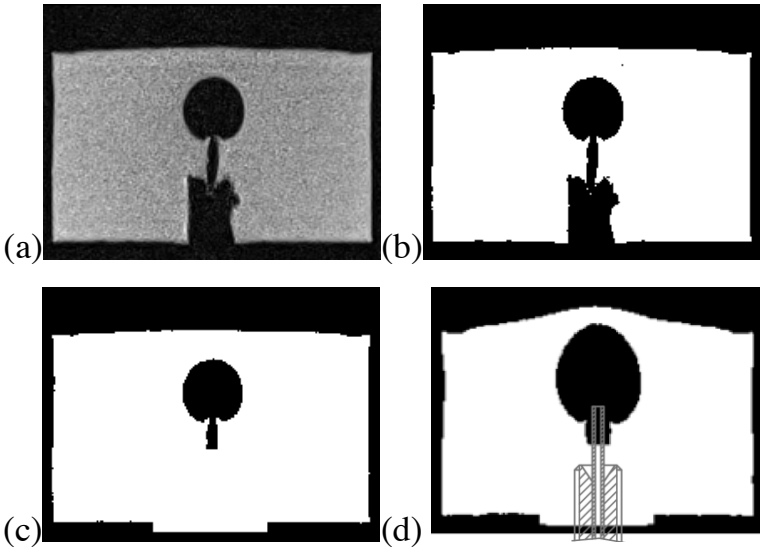

Figure 2.2: Typical MRI image and associated processed inages. (a) Raw MRI image containing the largest section of the bubble (largest horizontal lines constituted by the voxels in the bubble) amongst the 88 images of the 3D reference sequence (300) before the creep. (b) Thresheld image of the image presented in (a). (c) A mask was applied in order to make the thread rod disappear in the image (b). (d) Masked and thresheld image at the end of the creep.

2.5.2 *Radii*

The horizontal and vertical radii were estimated on images issued from the three sequences listed above (see section 2.4.3). The image containing the largest section of the bubble (*i.e.* the highest horizontal radius in the $[0, x)$ direction) was detected amongst the 52 images of the 3D (500) sequence, and amongst the 88 images of the 3D (300) sequence (Figure 2.2a). The image from the 2D (240) sequence was used directly since it was acquired in the plane of symmetry of the cylinder of cheese. The selected image was thresheld with Otsu's method (Figure 2.2b) as for the determination of the bubble volume. The thread rod was masked (Figure 2.2c). The largest diameters and the last voxel belonging to the bubble in the vertical direction at the top of the bubble (Figure 2.3) were located using an automated algorithm. The horizontal radius R_h was calculated according to Eq. 2.6.

$$R_h = \frac{(x_2 - x_1)}{2} \tag{2.6}$$

where x_2 and x_1 were the x-coordinates of the voxels delimiting the largest horizontal diameter (Figure 2.3).

The vertical radius R_v (Figure 2.3) was determined according to Eq 2.7.

$$R_v = y_2 - y_1 \tag{2.7}$$

where y_2 was the y-coordinate of the highest voxel belonging to the bubble in the vertical direction and y_1 was the y-coordinate of the largest diameters of the bubble (Figure 2.3). Because of voxellisation, the outlines of the bubble at the largest width were vertical-like rather than curved. y_1 was evaluated according to Eq. 2.8.

$$y_1 = \frac{y_t - y_b}{2} \tag{2.8}$$

where y_b and y_t were the bottom and the top y-coordinates of the largest bubble diameters (Figure 2.3). $y_t - y_b$ was the region of non-decision about the largest horizontal diameter.

For the horizontal radius, the standard uncertainties $u(x_2)$ on x_2 and $u(x_1)$ on x_1 coordinates were estimated according to Eq. 2.4 with an amplitude of uncertainty (a) equalled to the voxel size. The resulting combined standard uncertainty on R_h was estimated, Eq. 2.9 (JCGM 49).

$$u_c(R_h) = \frac{1}{2}\sqrt{u(x_1)^2 + u(x_2)^2} \tag{2.9}$$

where covariance between the measurements of x_i was neglected. For the vertical radius, the standard uncertainty $u(y_2)$, $u(y_b)$ and $u(y_t)$ on the y_2, y_b and y_t coordinates was estimated according to Eq. 2.4 with an amplitude of uncertainty (a) equalled to the voxel size. The combined standard uncertainty on y_1 was estimated, Eq. 2.10.

$$u_c(y_1) = \frac{1}{2}\sqrt{u(y_t)^2 + u(y_b)^2} \tag{2.10}$$

The combined standard uncertainty on R_v was estimated, Eq. 2.11.

$$u_c(R_v) = \sqrt{u(y_2)^2 + u_c(y_1)^2} \tag{2.11}$$

The resulting expanded standard uncertainties $u(R_h)$ and $u(R_v)$ in the horizontal and vertical radius were considered to be twice the combined standard uncertainty. They are reported in Table 2.1.

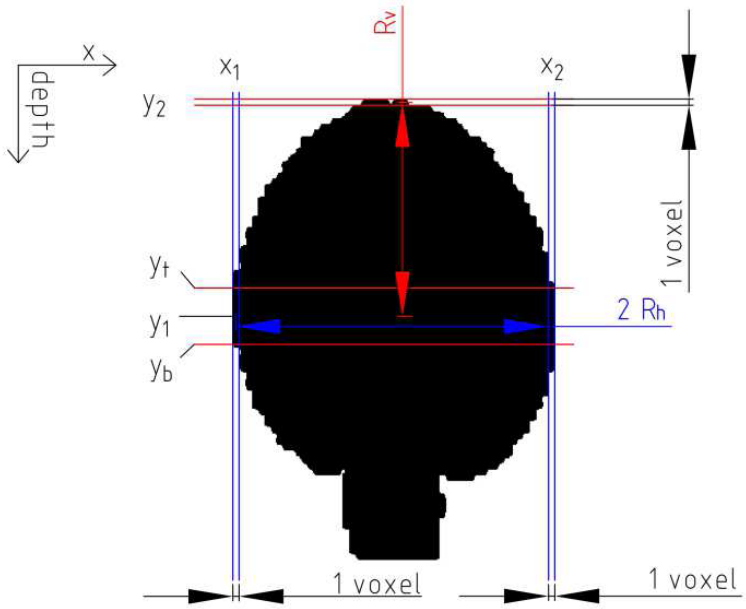

Figure 2.3: Dimensional calculations applied to a typical bubble in cheese, with their uncertainties. Calculations were applied onto the image presenting the largest dimensions for the bubble, and after thresholding and labeling of the MRI image. The bubble presented here was acquired with the 3D (500) sequence, at the end of the creep. The pixel indetermination on x_i and y_i are presented. y_b and y_t are the lowest and highest positions of the largest diameters in the image.

2.5.3 *Upper surface deflected shape*

The upper surface deflected shape (Figure 2.7c, d) was determined using the same image as for the radii determination. Special care was adopted to set the plane of acquisition where the largest bubble diameter was found at the beginning of the experiment. The cheese upper surface was located at the position linearly interpolated between the positions of the voxels of which intensities were just above and just below Otsu's threshold.

The MRI method for estimating the deflected surface was validated by using a "true" reference that consisted of a known cheese upper surface deflected shape measured with a comparator gauge. The cheese surface that served for this validation was cut roughly with a knife. In the followings the uncertainty on the reference was first estimated.

A comparator gauge was first checked on 10 gauge blocks. The gauges ranged from 1 to 1.9 cm with 100 µm between each. The gauge blocks were put on a marble stabilized table. The gap in height between the 1.9 cm gauge and the others was measured down to 1 cm using the comparator gauge. The difference (a) between the true reference and the measurement was 20 µm at most. The uncertainty associated to the comparator measurement gauge was so estimated at $u_{comp\,ref}(ref\,deflected\,shape) = 6$ µm according to Eq. 2.4.

Then, the reference upper deflected shape was measured three times at 18 positions along a diameter using the comparator gauge (Figure 2.4). The average over the three measurements of the upper surface, y_{comp}, and its standard deviation, $\sigma(y_{comp})$ were determined at each of the 18 point positions. The vertical bar in Figure 2.4 combined $u_{comp\,ref}(deflected\,shape)$ and the standard deviation, $\sigma(y_{comp})$.

The standard uncertainty on the horizontal comparator position was evaluated at 0.28 mm, and is represented as the horizontal bars in Figure 2.4. Since the mean difference to the standards was not corrected in the MRI method, it was considered as an uncertainty of the MRI method in itself. The combined standard uncertainty on the vertical position of the upper deflected shape was evaluated according to Eq. 2.12.

$$u_c(deflected\,shape) = \sqrt{\sigma\left(y_{im} - \overline{y}_{comp}\right)^2 + \sigma\left(\sigma\left(y_{comp}\right)\right)^2 + u^2_{comp\,ref}(ref\,deflected\,shape)} \tag{2.12}$$

where $\sigma(y_{im} - \bar{y}_{comp})$ was the standard deviation of the distance between the upper deflected shape position y_{im} determined with image analysis and the averaged upper deflected shape position y_{comp} determined with the comparator gauge. $\sigma\left(\sigma\left(y_{comp}\right)\right)$ was the standard deviation of the standard deviation of the upper deflected shape measured with the comparator gauge at each of the 18 positions.

2.5.4 *Bi-extensional strain rate and strain within the cheese cylinder*

In order to estimate whether the bubble growth occurred in a small or large elastic strain condition, the bi-extensional strain rate ($\dot{\epsilon}_b$) (Eq. 2.13) and the maximal strain encountered in the cylinder of cheese (ϵ_h) were calculated

$$\dot{\epsilon}_{b_i} = \frac{1}{R_i}\frac{dR_i}{dt} \tag{2.13}$$

$$\epsilon_h = \frac{dR_h}{L} \tag{2.14}$$

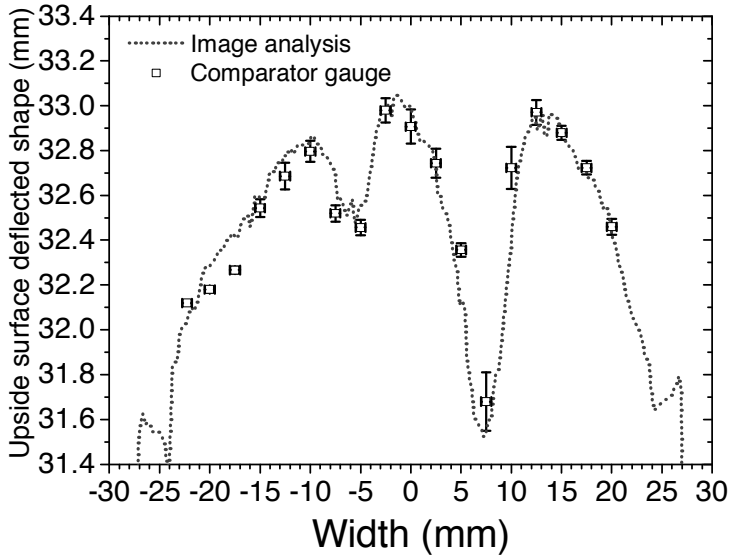

Figure 2.4: Comparison between the MRI method and a comparator gauge applied to a reference upside surface of a cheese cylinder roughly cut with a knife. The vertical bar depicted the combined standard deviation on the comparator measurement (including three measurements at each of the 18 points) and the horizontal bar, the standard uncertainty on the horizontal position of the comparator gauge.

where dR_i was the variation in bubble radius along whether the horizontal $(i = h)$ radius or the vertical radius (v) (between time $t0$ and $t1$) and L was the distance between the outline of the bubble and the lateral side of the cheese cylinder at $t1$ along the horizontal radius. The strain (ϵ_h) was only estimated in the region where the higher cheese compression was likely to occur.

Table 2.1: Expanded standard uncertainties on volume, radii of the bubble and the upper deflected shape of the cheese cylinder for the different MRI sequences used in the study.

	3D (300)	3D (500)	2D (240)
Volume for $R = 5.45$ mm (mm^3)	40	70	-
Vertical radius (mm)	0.22	0.36	0.17
Horizontal radius (mm)	0.12	0.20	0.10
Upper surface deflected shape (mm)	0.25	0.42	0.20

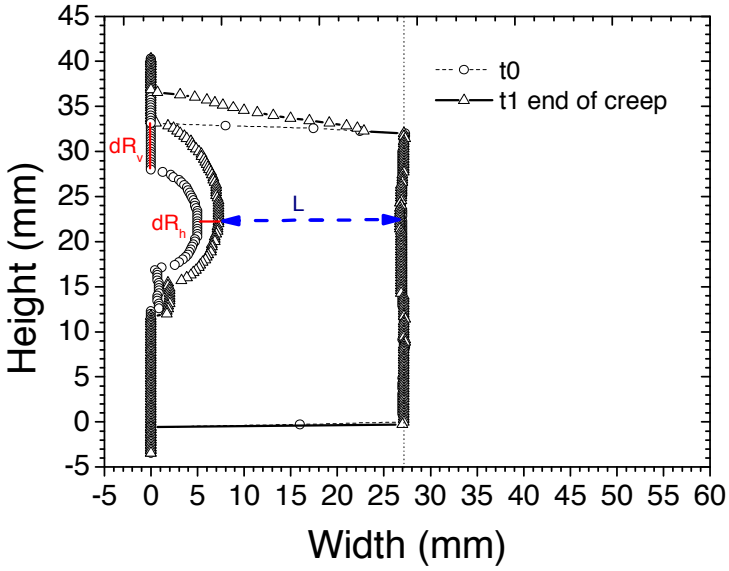

Figure 2.5: Contours were obtained with the 3D (300) on the cylinder of cheese. The initial contour at $t0$ was the contour obtained just before the creep and the contour at the End of the creep (at $t1$) was obtained just after the beginning of recovery. dR_h an dR_v were variations in horizontal radius between $t0$ and $t1$. L was the distance between the right-hand side of the bubble and the right-hand side of the cylinder.

3 RESULTS

3.1 WATER CONTENT

The water content within the cylinder of cheese was 41.1 ± 0.43% in average within the 32 slices at the beginning of the experiment. No difference was found between the bottom and the top of the cylinder (along the $[O; depth)$ axis) since averages were not different; respectively 41.04 ± 0.47% and 41.16 ± 0.40%. The water content increased from 40.54 ± 0.15% to 41.48 ± 0.23% from the left to the right of the cylinder of cheese along the $[0; x)$ axis (Figure 2.1b). The mechanical properties might have been a little affected (Laridon et al. 57) but were considered to be sufficiently homogenous not to affect the bubble growth behavior in a relevant manner.

3.2 BUBBLE VOLUME

Figure 2.6 presents typical changes in volume and pressure inside the bubble isolated in the cheese material. Sudden variations in volume increase were measured when steep variations in pressure were applied as at 0 min (Figure 2.6b 1 increase in pressure), at 41 min (Figure 2.6b 2 drop in pressure), and at 700 min when the pressure suddenly decreased due to gas leaks (Figure 2.6b 4 drop in pressure).

The volume of the bubble was 677 ± 40 mm^3 initially. At the very beginning (1), the volume increased almost instantaneously from 677 ± 40 mm^3 to 900 ± 82 mm^3 (the black line in Figure 2.6b 1). Then, the volume linearly increased from 900 ± 82 mm^3 to 1290 ± 102 mm^3 (the red line in Figure 2.6b 2) at a speed of the order of $8.7 \cdot 10^{-11}$ m^3/s while pressure was almost constant. When the pressure stabilized at about 2.7 times as much as the natural pressure in cheese (Figure 2.6b 3) the volume increase, from 1290 ± 102 mm^3 to 2200 ± 145 mm^3, was linear and of the order of $2.6 \cdot 10^{-11}$ m^3/s (the blue line in Figure 2.6b 3). Such a linear response in the bubble volume increase to a constant load has observed repeatedly (from other runs) with a standard deviation of the slope of $1.1 \cdot 10^{-11}$ m^3/s. When the atmospheric pressure (5) was applied, the volume decreased exponentially (Figure 2.6c). At the end of the recovery, the volume still slightly decreased but seemed to tend to a horizontal asymptote.

When the lowering in pressure was applied (6), the volume decreased first and then increased slightly when the pressure returned to the atmospheric (in Figure 2.6d). The volume tended to an asymptote and not to return to the volume the bubble had at the beginning of the experiment.

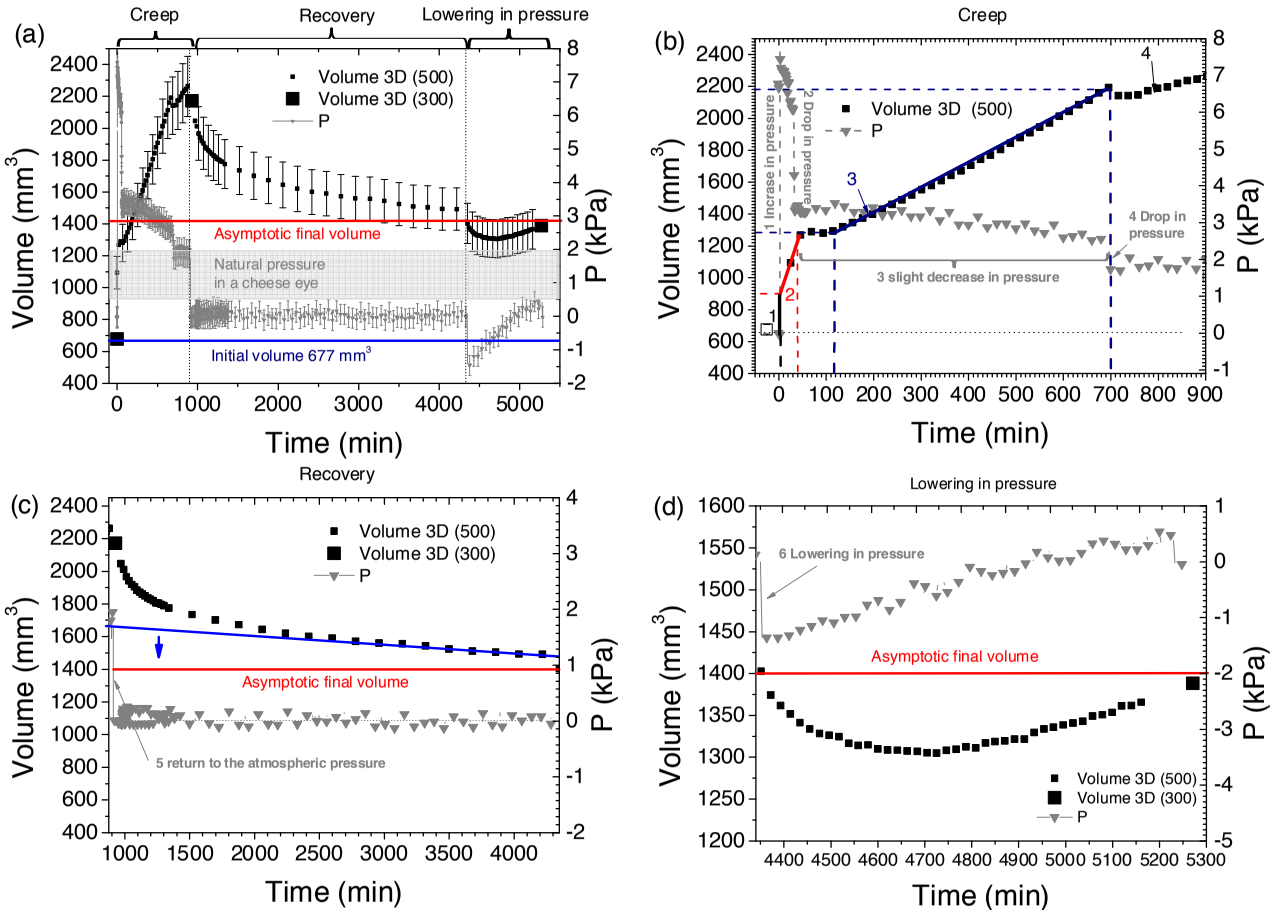

Figure 2.6: (a) Volume and air pressure according to time; creep, $P > 0$, recovery, $P = 0$, lowering in pressure, $P < 0$. The natural pressure in semi-hard cheese (Grenier et al. 37) is indicated by the grey area in (a). Bars are the expanded standard uncertainties on the pressure (0.3 kPa) and on the volume (as a function of the volume see section 3.1). (b) Details of the volume and pressure according to time for the stages of creep, (c) the recovery and (d) the lowering in pressure.

3.3 BUBBLE RADIUS AND UPPER DEFLECTED SHAPE

Except for the horizontal radius during the recovery period, the total changes observed in radius were much higher than the uncertainties estimated (ratio of 5 at least). Changes in the deflected surface at the highest point were three to twenty times higher than the uncertainty estimated during the recovery and creep periods respectively. The vertical and horizontal radii were initially 5.7 ± 0.22 mm and 5 ± 0.12 mm (Figure 2.7a), yielding an almost spherical bubble ($R_v = 1.14R_h$).

When the first steep increase in pressure (1) was applied, both the horizontal and the vertical radii increased (the small white circles and triangles with bars in Figure 2.7a). At 40 min, the vertical and the horizontal radii were 7.3 ± 0.17 mm and 6.3 ± 0.10 mm. The vertical radius increased in a slightly higher extent than the horizontal radius, 1.6 ± 0.27 mm instead of 1.3 ± 0.16 mm. The subsequent upward displacement of the middle of the upper surface was 1.4 ± 0.20 mm (The two lowest black upper deflected shapes in Figure 2.7c).

At constant load (3), the linear increases in vertical and horizontal radii were $6.6 \cdot 10^{-8}$ m/s and $3.2 \cdot 10^{-8}$ m/s. The upper deflected shape deformed toward the outside of the cylinder of cheese at the same pace as the increase in vertical radius, $6.7 \cdot 10^{-8}$ m/s (The blue upper deflected shapes in Figure 2.7c). At the end of the creep the vertical and horizontal radii were 9.7 ± 0.17 mm and 7.3 ± 0.10 mm. The bubble started to elongate in the vertical direction ($R_v = 1.33R_h$) and was no more spherical.

The maximal strain encountered during the experiment, as defined in section 2.5.4, was evaluated on the widest range of radius between 0 min, just before the increase in pressure (1) was applied, and 900 min (2.3 mm). The distance (L) was evaluated at 21.8 mm. The maximal strain was 10.6%. When sudden variations in pressure were applied, the maximal strain did not exceed 3%. Beside the elastic response, the maximal steep increase in radii was encountered between 5 s and 40 min when the highest pressure was applied. At that time, the maximal strain rate was $7.9 \cdot 10^{-5}$ s^{-1}, evaluated considering the horizontal radius variation (see section 2.5.4). The same calculation on the vertical radius led to $9 \cdot 10^{-5}$ s^{-1} as the increase in vertical radius was the fastest.

During recovery, both vertical and horizontal radii decreased simultaneously. The vertical radius decreased, from 9.7 ± 0.17 mm to 8.2 ± 0.17 mm, in a higher extent than the horizontal radius that only decreased from 7.3 ± 0.10 mm to 6.4 ± 0.10 mm. The upper deflected shape moved down (from 36.6 ± 0.20 mm to 35.9 ± 0.20 mm) (the red shapes in Figure 2.7d) simultaneously until 1698 min. Then, the upper deflected shape stabilized and did not move anymore (the blue shapes in Figure 2.7d).

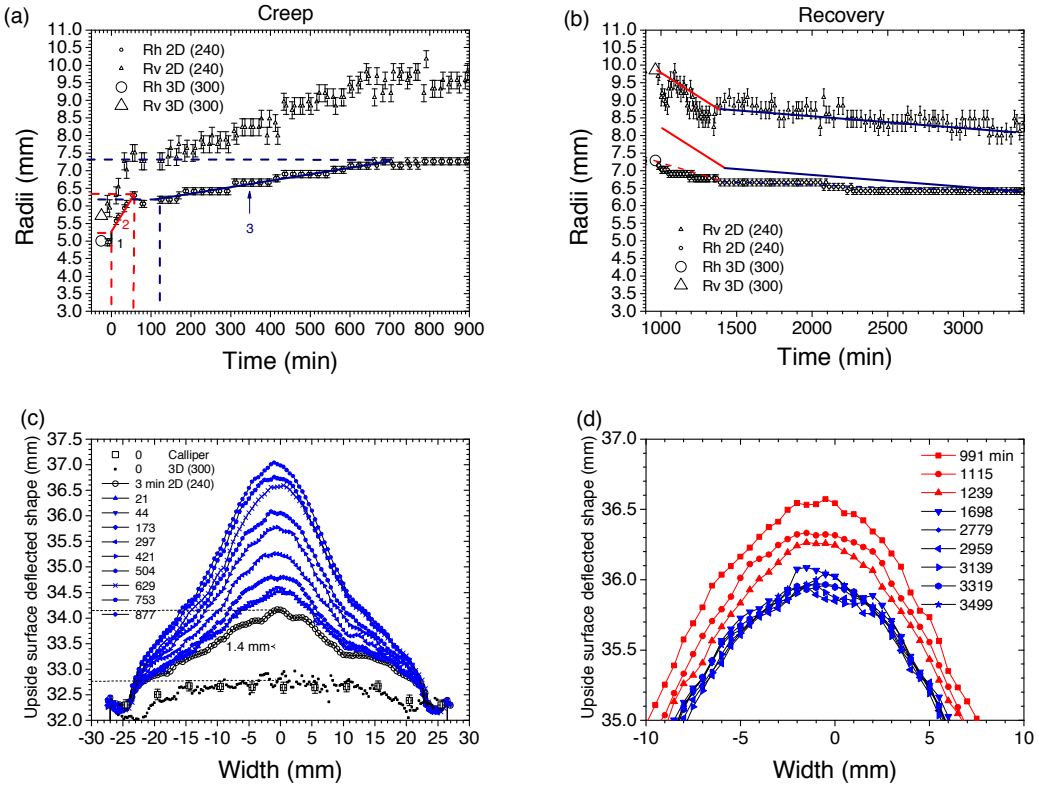

Figure 2.7: (a) Horizontal and vertical radii according to time (creep); (1) Instantaneous increase in horizontal radius, (2) $3.7 \cdot 10^{-7}$ m/s, (3) linear increase in horizontal radius, $3.2 \cdot 10^{-8}$ m/s deflected shapes according to time (c) creep (d) recovery. The expanded standard uncertainty (not shown) on the upper surface deflected shape was evaluated at 0.20 mm (see Table 2.1 and section 3.1).

4 DISCUSSION

4.1 ABILITY OF MRI AND ASSOCIATED IMAGE ANALYSIS TO DESCRIBE THE GEOMETRY OF BUBBLE AND CHEESE DYNAMICALLY

For an bubble radius of 5.45 mm, the method developed in this study made it possible to measure the volume with an accuracy of 6% and 10% with voxel sizes of 0.3^3 mm^3 (acquisition time of 1 h 08 min) and 0.5^3 mm^3 (acquisition time of 8 min 45 s). This relative uncertainty decreased with the increase in bubble volume. Experiments where the initial volume of the bubble was too small (namely diameters between 4 and 6 mm) and levels of pressure were too low (because of early leakage) were not considered for the present analysis since variations in volume were not enough large compared to the uncertainties reported above.

Likewise, the increase in accuracy with the decrease of the voxel size from 0.5^3 mm^3 to 0.3^3 mm^3 was low regarding the increase in the time of acquisition from 8 min 45 s to 1 h 08 min. Except when steep variations in pressure (within a few seconds) were applied, the acquisition time of 8 min 45 s was satisfactory to follow the variations in volume (of the order of $8.7 \cdot 10^{-11}$ m^3/s) and images did not present any blurring. Note that assessing bubble volume within a few seconds would have dramatically deteriorated the spatial resolution. This point will be further discussed in the Discussion section.

The development of the method for determining the upper deflected shape was a step forward compared to the use of a comparator gauge. It allowed us not to remove the setup from the MRI table to measure it with the comparator gauge on a separate table, by the way decreasing the risk in gas leaks.

4.2 LOW PRESSURE WAS FOUND TO BE ABLE TO INFLATE THE CHEESE BUBBLE

At the very beginning of the experiment (1), the applied pressure (7.5 kPa) was higher than that actually measured in cheese (1.3 kPa, Grenier et al. 37) and that found to be able to inflate an bubble in Emmental cheese (5 kPa, Fluckiger et al. 30).

After 41 min, the pressure was between half and twice as much as that found in real cheese. These results showed that level of pressure of the order of 3.5 kPa was able to inflate an bubble in semi-hard cheese. Measurements of bubble volume carried out within real cheese blocks (Grenier et al. 37) were influenced by the outer ring, possibly including spatial variability in mechanical properties and the effect of the foil surrounding the cheese. In this study, only the proximate surrounding cheese was controlling the bubble growth.

Such a level of pressure remains very low and of the order of the atmospheric pressure variations; in the meantime the bubble inflated a lot (up to 3.2 times as much as the initial volume). Both low pressure and high volume increase were pieces of evidence that bubble growth was poorly controlled by mechanics in that experiment and that semi-hard cheese mostly flowed around the bubble. Low pressure seems typical so far of bubble growth in food materials; internal pressure during the fermentation of bread dough (closed bubbles) was 6 times as low as that found in cheese during the first days of hot room (Grenier et al. 35).

4.3 QUASI-ABSENCE OF TIME-INDEPENDANT ELASTICITY AND SMALL ELASTIC STRAIN IN CHEESE DURING BUBBLE GROWTH

During the recovery, the volume and both horizontal and vertical radii decreased simultaneously, chiefly due to the stress relaxation and in a less extent to the gravity. On a duration of 3,450 min (57.5 h), *i.e.* 21 times as much as the highest time of relaxation of the cheese (of the order of 10,000 s,Laridon et al. 57), the volume still slightly decreased. This slight decrease in volume did not make possible to evidence the absence of time-independent elasticity by itself. However, the slight increase in volume found after the lowering in pressure was applied, evidenced that no time-independent elasticity was driving the mechanical behavior of the cheese in the area where the cylinder of cheese was taken from, *i.e.* not too close to the surface whereby lower water content could have possibly modified this behaviour. Such a result was in agreement with the low level of stress encountered in a semi-hard cheese after a 15 hours' compression-relaxation experiment (Laridon et al. 57). However results from Laridon et al. [57] has been obtained on a duration 3.7 times as high as that used in an experiment of compression-relaxation. During an experiment of compression relaxation such as that performed in Laridon et al. [57], the small sample involved is very likely to dry on a long duration even when embedded in an oil film and drying can eventually interfere with the measurement. In this bubble growth experiment the water content did not evolve (section 3.1) and the conclusion of time-independent elasticity was even more reliable.

The extent of strain and extensional strain rate can also be analyzed more thoroughly to evaluate if small elastic strain can be considered for describing the bubble growth in semi-hard cheese.

The growth rate of the bubble, $8.7 \cdot 10^{-11}$ m^3/s, was of the same order of magnitude than that found in real cheese; $7.7 \cdot 10^{-11}$ m^3/s evaluated during ripening, between 10 and 13 days of hot room (Huc et al. 47). In the meantime, the cheese between the bubble and the sustaining apparatus was squeezed at a maximum linear strain of 10.6%. It can be concluded that when the volume increase was of the same order than that really measured in cheese blocks, the strain imposed to the cheese material was within the limit usually admitted for being linear in a purely elastic material. Note that it happened over a period equal to 5.4 times as much as the longest time of relaxation of the cheese (Laridon et al. 57). The bubble growth involved small elastic strains as soon as the deformations applied to the cheese were not too brief and too large. Consequently, the bubble growth in cheese is very unlikely to be described by nonlinear models and generalized Maxwell's model for instance can be applied for describing the bubble growth in cheese.

4.4 LINEAR RESPONSE OF THE CHEESE AND LOW BI-EXTENSIONAL STRAIN RATE

The maximal bi-extensional strain rate, $9 \cdot 10^{-5}$ s^{-1}, was about 40 times as much as that encountered during cheese ripening when estimated from the evolution of bubble diameters between day 8 and 12 of hot room ripening ($1.9 \cdot 10^{-6}$ s^{-1}, Grenier et al. 37). The conclusion of the experiment can be hence extended to the bubble growth in real cheese. Note that the lowest strain rate usually applied to cheese samples in rheological testing are 20 to 100 times as much as this maximal bi-extensional strain rate (Goh et al. 32, Masi and Addeo 64, Culioli and Sherman 21) and 5 times as much as the bi-extensional strain rate encountered in bubble growth during bread dough proofing (Babin et al. 7). The small strain rate involved in the experiment was also a piece of evidence that linear models are very likely to fit the bubble growth in cheese.

The linear increases in volume against an almost constant load (3 in Figure 2.6b, Figure 2.7a and c), as well as the progressive evolution of the upper deflected shape, were the evidence of a mainly viscous behavior. Viscosity was of the order of the ratio of the relative gas pressure to bi-extensional strain rate *i.e.* $\frac{3{,}500\,\mathrm{Pa}}{9 \cdot 10^{-5} \mathrm{s}^{-1}} = 3.9 \cdot 10^7$ Pa·s.

5

CONCLUSION

Gas pressure and gas volume inside a cheese bubble were continuously and simultaneously measured for the first time. A specific maintaining apparatus was developed in order to produce non-destructive, dynamic but accurate information about the size (volume and radii) of a gas bubble in cheese and about the shape of the upper surface of a cylindrical cheese sample. Calculation of the expanded standard uncertainty made it possible to give confidence in the variations that were reported and discussed.

Low amount of pressure (< 3.5 kPa) was proved to be able to inflate an bubble in cheese and evidenced that low resistance was opposed to gas inflation in cheese. The quasi-absence of time-independent elasticity was evidenced close to the core of the cheese block. Note that near the surface of the cheese block, the higher salt content and the lower water content could have modified this behavior and this result can only be considered close to the core of a semi-hard cheese. On a time scale close to that of the actual bubble growth in cheese, the bubble growth was driven by the viscous part of the viscoelasticity in a low elastic strain and low bi-extensional strain rate situation. Linear viscoelasticity is hence applicable to describe bubble growth in the semi-hard cheese under study.

The setup developed in this study and the MRI opens a way to connect information about geometry to known mechanical loads and further analysis of formulation changes on the mechanical behaviour of cheese.

Chapitre 3

MODELLING OF THE MECHANICAL DEFORMATION OF A SINGLE BUBBLE IN SEMI-HARD CHEESE, WITH EXPERIMENTAL VERIFICATION AND SENSITIVITY ANALYSIS

The aim of the study presented here was to investigate the momentum transport occurring during bubble growth in a viscoelastic material. The mechanical behaviour was modelled with a 5-element Maxwell model, implemented with the finite elements method, and a sensitivity analysis of the model parameters was undertaken. Air was injected into the bubble and growth was monitored with pressure sensors and by MRI image analysis. The experiment was repeated three times. Each time mechanical parameters were characterised on the same material as that used for the validation of the model. Simulations were conducted in conditions as close as possible to those of the experiment, and yielded good agreement with the experimental results.
Keywords: generalised Maxwell model; viscoelasticity ; ripening; momentum transport; relaxation times; elasticity ; bubble growth ; eye

1 INTRODUCTION

Bubble growth is a phenomenon occurring in various fields of application; it is caused by different dynamics and different mechanical behaviours of the material surrounding the bubble. The majority of scientific studies have considered rapid phenomena such as cavitation in liquids (Plesset 76), foaming of polymers (Ramesh et al. 77) and growth of bubbles in magma (Navon et al. 69). These studies have generated a variety of results in terms of bubble size (from the micrometre to the centimetre) and in terms of overall porosity of materials (up to 75% for polymer foams). The polymer industry has benefited from numerous studies on this subject and this has led to other developments, in particular in the food science area.

Amon and Denson [5] proposed a 1-D bubble growth model made of a single bubble surrounded by a small spherical amount of liquid polymer, constituting a cell unit that was considered to be representative of average bubble growth. Their approach had the advantage of being relatively simple, and included the modelling of mass transport from the polymer to the bubble (Patel 72, Elshereef et al. 25), but did not cover any interaction between bubbles and the possible coalescence of neighbouring bubbles. The notion of cell-based model was then extended to compressible materials (Arefmanesh et al. 6), viscoelastic materials (Ramesh et al. 77), and generalised to 3-D (Bruchon and Coupez 12). These studies duplicated the cell unit to take multiple bubble growth into account. Some of these models were reviewed by Lee and Ramesh [63]. Feng and Bertelo [29] showed that the influence of the viscoelastic material on bubble growth depends on the duration of the loading: for process times shorter than the characteristic relaxation time, viscoelasticity enhances bubble growth, whereas for process times longer than or of the same order of magnitude as the characteristic relaxation time, viscoelasticity slows the bubble growth down. Venerus et al. [89] studied several non-linear viscoelastic models (Oldroyd-B, upper convected Maxwell and Phan-Thien-Tanner models) and showed that the nonlinearity of the models was of little importance for bubble growth, since the deformation rate was significant at the beginning of the process but very rapidly decreased afterwards.

There are few modelling approaches for the bubble growth in food products, and they are almost exclusively confined to sparkling drinks or cereal products (Campbell and Mougeot 15). There are two main approaches for the study of bubble growth in food products. The first considers bubble growth mainly from a mass transport point of view, where bubble growth is controlled only by the transport of dissolved gas from the material into the bubble (Handleman and Lyons 40, Huang and Kokini 43, Shah et al. 85), the mechanical reaction of the bubble being controlled only by sur-

face tension. The mathematical model developed to describe a single bubble growth in bread dough (Shah et al. 85) was later extended to multiple bubbles in a continuum approach (Chiotellis and Campbell 16, 17). The second approach considered coupled modelling within a continuous domain, where bubble growth is controlled by the interaction between several phenomena such as momentum and mass transport. Additional coverage of heat transport phenomena is often needed to cover the baking process. de Cindio and Correra [23] and Hailemariam et al. [39] considered the case of a viscoelastic material (bread dough) modelled by linear or nonlinear viscoelastic models. Bikard et al. [9] and Bikard et al. [8] investigated a similar approach for coupling mass and momentum transport, where the material (bread dough) was modelled with a purely viscous law. The choice of a particular mechanical behaviour model was rather a postulate and was not discussed in these previous studies.

While more realistic, multiphysics approaches (coupling between momentum transport and mass and heat transport) require a large number of model parameters. These can be difficult to assess experimentally, and are often extracted from other studies in the literature, and are not appropriate for the specific experimental validation conditions used by the modellers. Input parameters can also be determined by comparison between simulated and experimental data, with either trial and error or numerical optimisation. Moreover, the scale of observation is rarely consistent with that of the description of phenomena in previous models, rendering the validation of low value. In the case of bubble growth in food, experimental validation, when included in the study, often takes place at a macroscopic level, *i.e.* total volume and total mass loss (Fan et al. 28, Feng and Bertelo 29). Validation on the bubble scale is rare (Kontopoulou and Vlachopoulos 54, Yano and Shimiya 94). Moreover, with the growing numbers of mechanisms and parameters, critical analysis of the influence of each mechanism or parameter on the model becomes more difficult, and analysis of the couplings is not straightforward. Generally, the experimental and simulated results are compared from an overall point of view (Ramesh et al. 77). The acquisition of experimental data, when appropriate, in conditions involving a single transport phenomenon, separately from the others, should improve the quality of the fitting and adjustment of the few, specific entry parameters, thus contributing to a higher quality validation/invalidation procedure for the complete model. Together with observation at the bubble scale, this is the global approach applied in this study. Observation on the bubble scale has been made possible by the recent advances in imaging techniques, *e.g.* Aguilera and Lillford [2].

Compared to the phenomenon investigated in the present study, previous studies performed on polymers have presented two main drawbacks: the bubbles were small with diameters lower than 10^{-5} m, whereas bubbles in cheese are in the order of 10^{-3} m (Huc et al. 44); and the processes were relatively fast, several minutes for polymer foaming compared to several days for cheese ripening. Their conclusions cannot easily be extrapolated to the present study.

On the other hand, because of the large size of bubbles in cheese under ripening, the isolation and instrumentation (pressure measurement) of a single bubble are possible experimentally (Grenier et al. 37), and provide consistency between the scales of observation and theory. Slow dynamics allow the use of tomographic techniques for monitoring the volume of the bubble despite the opacity of the material. Finally, by controlling the boundary and load conditions, the mechanical behaviour can be studied separately from mass production and transport.

The aims of the present study were:

- To extend the study of bubble growth in viscoelastic material to semi-hard cheeses. There are no studies in the literature to our knowledge that deal with the modelling of bubble growth in semi-hard cheeses. Prior focus has been limited to nucleation and early bubble growth with major contribution of surface tension ; it did not include any experimental verification (Akkerman et al. 3).
- To test the suitability of the generalised Maxwell mechanical model by implementing a finite element model to reproduce the mechanical deformation of a single bubble as observed experimentally; three repetitions were used to meet this aim.
- To characterise the effects of different model parameters on mechanical deformation and to provide a critical analysis of these effects by performing sensitivity studies.

2 MATERIALS AND METHODS

2.1 EXPERIMENTAL PROCEDURE

The aim of the experiment was to isolate a single bubble from a semi-hard cheese block in a dedicated maintaining apparatus (Figure 3.1) and to inflate the bubble by adding a given amount of gas, thus increasing the pressure inside the bubble. The whole experiment was monitored with MRI (Magnetic Resonance Imaging) and a pressure sensor.

Three experiments were conducted on three separate bubbles isolated in a cheese cylinder, differing in their load history. In Experiment 1, pressure was maintained relatively constant (slow decrease from 5.5 kPa to 3.7 kPa) for 8 h (Figure 3.7a). For Experiment 2, a 6 kPa pressure peak was applied, followed by holding at a lower pressure value of 3 kPa for 2 h (Figure 3.7c). Finally, slight pressure (1 kPa) was maintained for the remaining time of the experiment (Figure 3.7c). For Experiment 3, successive holdings of pressure were applied, with decreasing pressure levels at each step (Figure 3.7e). Special care was taken that the pressure applied to the bubble was of the same order as that found in real cheeses, from 0.5 ± 0.3 to 3.8 ± 0.3 kPa over the first few days and 0.5 ± 0.3 to 1.5 ± 0.3 kPa thereafter (Grenier et al. 37).

The various loads applied to the bubble interface were intended to mimic plausible situations: the long-term low-pressure was characteristic of bubble growth, while sudden high-pressure changes were representative of handling of cheese blocks or of sudden temperature changes that occur during ripening and that cause the pressure to change accordingly, following the ideal gas law.

Experiments 1 to 3 also differed by the mechanical properties of the cheese material (variability between batches) and the size and position of the bubble inside the cheese cylinder (Table 3.1).

2.1.1 *Sample preparation*

For each experiment, one cheese block was extracted from a production batch at the industrial site, and sent to the laboratory, where it was ripened for nine days in temperature-controlled cabinets (Grand Cru, Liebherr, France). A single bubble surrounded by plain cheese was first located by scanning the whole cheese block using an MRI scanner (Avanto 1.5T, Siemens, Germany). A cylindrical sample containing the bubble placed on the axis of symmetry of this cylinder was extracted with a stainless steel tube. The cheese cylinder was placed inside the maintaining apparatus (Figure 3.1) after the cheese height had been adjusted by cutting its top surface.

The maintaining apparatus was placed in the MRI scanner, at a regulated temperature of 20 ± 1 °C; it was not moved throughout the experiment (7 to 15 hours).

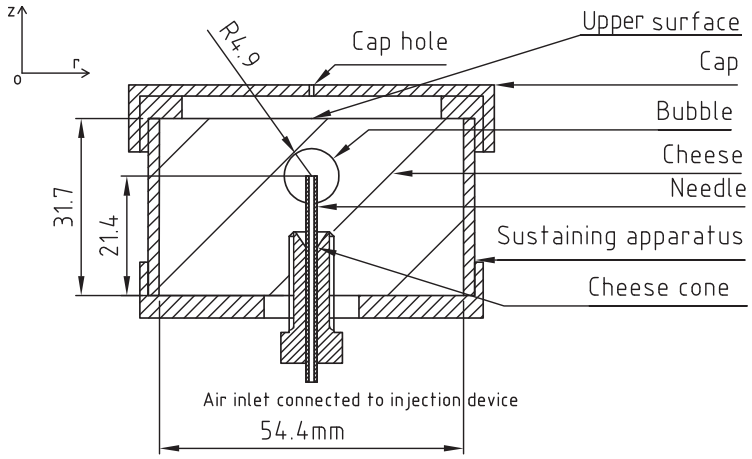

Figure 3.1: Sustaining apparatus (the values given for the heights of the cheese cylinder, the bubble and the radius of the bubble are specific to Experiment 2).

2.1.2 *Measurements*

A needle connected to an air inlet (Figure 3.1) was inserted into the bubble, at its bottom surface. The needle was held in place by a thread rod screwed into the cheese. Screwing in this rod formed a cheese cone (Figure 3.1) that limited gas leakage during positioning of the needle and after gas injection. Pressure in the bubble was measured in the air injection device with a calibrated absolute pressure transducer (XCEL-100-25A, Kulite, USA). The acquisition frequency was 1 Hz, with satisfactory resolution

on an Ahlborn data logger (Almemo 2590, Ahlborn, Germany). The atmospheric pressure outside the device was measured and pressure relative to the atmosphere was obtained by subtracting the atmospheric pressure from the absolute pressure. In this study, pressure is given relative to the atmospheric pressure. For more details see Grenier et al. [36].

MRI sequences were launched before gas injection to characterise the initial geometry of the domain (bubble dimension and upper deflected shape). Gas was injected just after the first MRI acquisition.

A 3-D Spin-Echo sequence was used for this study, with two different sets of parameters. The following set of parameter values was used to monitor bubble volume and upper deflected shape over time: echo time = 10 ms, repetition time = 400 ms, bandwidth = 295 Hz, pixel size = 0.5×0.5 mm², slice thickness 0.5 mm, 1 scan, Signal to Noise Ratio = 53. The acquisition time was 8 min 45 s, and the whole cheese cylinder (52 slices) was acquired. Spatial resolution in the plane was increased for the first acquisition (pixel size = 0.3×0.3 mm², slice thickness 0.7 mm), with a reduced Signal to Noise Ratio (27) and increased number of slices (88), echo time (12 ms) and acquisition time (1 h 08 min). MRI cross-sections are shown in Figure 3.5 for the three experiments, at the beginning and at the end.

2.1.3 *Data analysis and uncertainties*

Bubble volume was obtained from MRI image analysis by adding together all the bubble voxels after thresholding according to the Otsu method (Otsu 71). With such a method, some voxels of partial volume (partially filled with gas and cheese) were not considered, leading to a systematic underestimation of the volume. The uncertainty on determination of the bubble volume was a function of the measured volume, and did not exceed 10% of the measured volume (Grenier et al. 36).

The upper deflected shape was evaluated by image analysis from a single MRI image that contained the axis of symmetry of the cylinder. The Otsu method was used to define the greylevel threshold that made it possible to distinguish between cheese and gas in the MRI images. Smooth interpolation of the greylevel presented by the pixels near the upper surface of the cheese as a function of the z-coordinate was used to locate the upper surface of the cheese cylinder. This MRI method for measuring the deflected shape was validated by comparison with measurements with a comparator performed on the same cheese surface; the deflected shape of the upper surface was determined by MRI with an uncertainty of 0.2 mm (Grenier et al. 36)

The uncertainty associated with the pressure measurement was estimated to be 0.3 kPa (Grenier et al. 36).

2.2 MODELLING

Modelling of the rheological behaviour of semi-hard cheese has been reported in a previous paper (Laridon et al. 57). The modelling briefly outlined in sections 2.2.1 and 2.2.2 was adapted to match a specific geometry (section 2.2.3). Moreover, whereas in the previous study the geometry allowed reduction of the problem to a temporal dimension, the presence of the bubble interface necessitated the use of more complex modelling, and increased the number of model parameters.

2.2.1 *Model assumptions*

The semi-hard cheese studied was considered incompressible (Calzada and Peleg 14), and the domain was considered to be homogeneous. Bubble growth in cheeses is a relatively slow phenomenon, the bubble interface moving at about 10^{-7} m/s (Musse et al. 68), and therefore no inertial terms were considered.

2.2.2 *Governing equations*

Quasistatic equilibrium was expressed by the conservation of momentum:

$$\nabla \cdot \boldsymbol{S} = \rho \boldsymbol{g} \tag{3.1}$$

where $\boldsymbol{S}$ is the stress tensor, ρ the material density, and $\boldsymbol{g}$ the gravity. $\boldsymbol{S}$ was divided into a purely elastic part σ, and a viscoelastic part τ. The former was expressed using the tensor form of Hooke's law and the latter using a 5-element generalised Maxwell model, thus providing:

$$\sigma = \boldsymbol{C} : \boldsymbol{\epsilon} \tag{3.2}$$

where $\boldsymbol{C}$ is the usual fourth-order tensor of rigidity and $\boldsymbol{\epsilon}$ the strain tensor. This elastic part of the stress was split into spherical and deviatoric parts to separate shear and bulk moduli (Voigt notation is used for convenience):

$$\boldsymbol{\sigma} = G_0 \begin{pmatrix} 4/3 & -2/3 & -2/3 & & & \\ -2/3 & 4/3 & -2/3 & & & \\ -2/3 & -2/3 & 4/3 & & & \\ & & & 2 & & \\ & & & & 2 & \\ & & & & & 2 \end{pmatrix} \boldsymbol{\epsilon} + K \mathrm{tr}(\boldsymbol{\epsilon}) \boldsymbol{I} \tag{3.3}$$

where G_0 is the shear modulus, K the bulk modulus and $\boldsymbol{I}$ the identity tensor. The viscoelastic part of the stress is the sum of the stress in each Maxwell element:

$$\boldsymbol{\tau} = \sum_{i=1}^{N} \boldsymbol{\tau}_i \tag{3.4}$$

For each Maxwell element the following equation has to be solved:

$$\boldsymbol{\tau}_i + \lambda_i \frac{\partial \boldsymbol{\tau}_i}{\partial t} = \lambda_i G_i \frac{\partial \boldsymbol{\gamma}}{\partial t} \tag{3.5}$$

where λ_i and G_i are the relaxation time and the shear modulus of the Maxwell element i, respectively, and $\boldsymbol{\gamma}$ is the deviatoric part of the strain tensor.

The generalised Maxwell model usually presents a purely elastic element, that has been expressed here in the deviatoric part of the elastic stress tensor (Eq. 3.3). However, the previous studies did not show any long-term elastic behaviour (Laridon et al. 57, Grenier et al. 36), and therefore G_0 was set at 0. Thus, Eq. 3.1 becomes:

$$\begin{cases} \nabla \cdot \left(K \mathrm{tr}(\boldsymbol{\epsilon}) \boldsymbol{I} + \sum_{i=1}^{N} \boldsymbol{\tau}_i \right) = \rho g \\ \boldsymbol{\tau}_i + \lambda_i \frac{\partial \boldsymbol{\tau}_i}{\partial t} = \lambda_i G_i \frac{\partial \boldsymbol{\gamma}}{\partial t} \end{cases} \tag{3.6}$$

The shear moduli were expressed in terms of proportions α_i of the overall shear modulus G:

$$\alpha_i = \frac{G_i}{G = \sum_{i=1}^{N} G_i} \tag{3.7}$$

2.2.3 *Boundary conditions*

The plain cheese geometry consisted of a cylinder, which is represented by the domain between boundaries 2, 3 and 4 in Figure 3.2a. A 2-D axisymmetric representation was used to take advantage of the symmetry of the geometry (Figure 3.2a - 1). The bubble was located on the axis of symmetry and was represented by the bubble interface 5 in Figure 3.2a. The boundary conditions (Figure 3.2a) were set to match as closely as possible the experimental conditions (see section 2.1). The pressure measured during the experiment was used as the applied pressure $p(t)$ at the bubble interface.

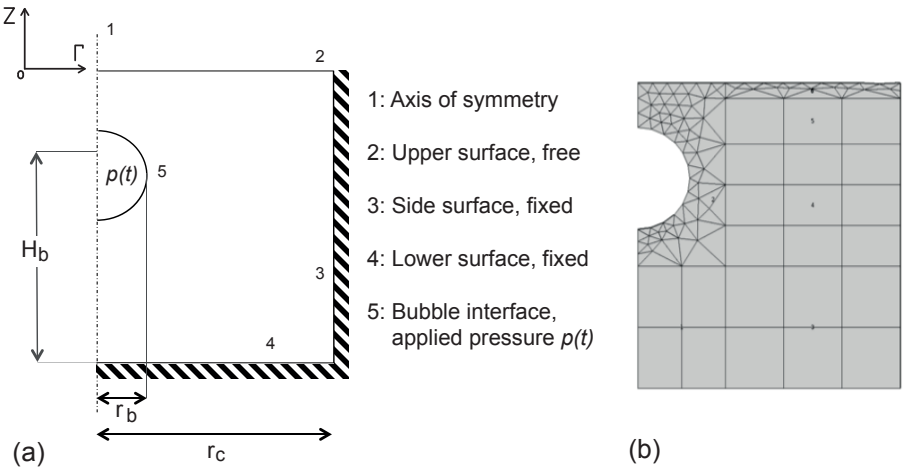

Figure 3.2: (a) geometry and boundary conditions of the domain and (b) the associated mesh retained after mesh sensitivity analysis (see section 2.3 for more details).For each experiment, r_c was set at 27 mm.

2.2.4 *Evaluation of model parameters*

The Maxwell model parameters (see Table 3.1) were determined on compression-relaxation experiments performed on samples from the same cheese block as that used for the bubble growth experiment. These values were therefore specific to each experiment. Assuming that composition gradients (water and salt content mainly) might affect the mechanical behaviour of the cheese material locally and assuming that these were symmetric in width and length at the cheese block scale, compression-relaxation samples were extracted from the cheese block symmetrically (relative to the width or length axis) to those used for the bubble growth experiment. The compression-relaxation tests were performed one day after the bubble growth experiment, but ripening time has been proven to have little effect on the parameter values (Laridon et al. 57). Further details about the measurement method can be found in Laridon et al. [57].

Uncertainty associated with the estimation of parameters was also evaluated for each mechanical parameter in the above cited paper and is reported in Table 3.1; this covers the imperfections of the mathematical method used for estimation of the parameters (imperfections were estimated using synthetic sets of compression-relaxation data), as well as the variability between cheese samples in the same relative position in the cheese block. In contrast to the estimation of uncertainties reported in Laridon et al. [57], it did not, in this experiment, take into account variability between cheese blocks, since measurements were performed on the same cheese block that served for the bubble growth experiment.

Initial values of H_b and r_b were calculated from the first MRI image, with 300 µm resolution in the plane. The uncertainty presented in Table 3.1 for these two parameters is a measurement error, and was evaluated as the standard deviation of at least 10 measurements on the initial MRI image with the image analysis software ImageJ (NIH, USA).

The applied pressure $p(t)$ applied at the bubble interface (Figure 3.2a) was the pressure measured during the experiment.

Table 3.1: Model parameters for the three experiments and estimation of uncertainties. For each experiment, r_c was set at 27 mm.

parameter	Exp 1	Exp 2	Exp 3	$\pm\sigma$ (%)
E (kPa)	259	329	331	12
α_1	0.59	0.55	0.59	0.7
α_2	0.19	0.21	0.20	8.2
α_3	0.12	0.14	0.13	9.5
α_4	0.05	0.05	0.05	8.0
α_5	0.04	0.04	0.03	6.1
λ_1 (s)	0.15	0.16	0.13	3.0
λ_2 (s)	2.30	4.29	3.80	13
λ_3 (s)	29.5	74.3	72	10
λ_4 (s)	579	1,123	1,140	15
λ_5 (s)	8,918	6,735	12,319	7.8
H_b (mm)	20	22	21	3.0
r_b (mm)	4.1	4.9	3.8	5.0

2.3 NUMERICAL IMPLEMENTATION

The model was implemented using FEM software COMSOL Multiphysics (COMSOL A.B., Sweden). A 2-D axisymmetric representation was used to reduce computational costs. The domain geometry was defined according to the experimental set-up (section 2.1) and to the boundary conditions of the model (section 2.2.3).

A backward differentiation formula (BDF) was used to determine the time steps for calculation. This time solver has the advantage of being relatively stable, despite being known to be unsuitable for solving high frequency problems. However, due to the nature of the problem studied here, the BDF was still appropriate. The mesh used for this study was a combination of triangular and quadrangular finite elements (Figure 3.2b). An analysis of the sensitivity of the model output to the mesh size was conducted

to determine the most suitable mesh size. Several mesh sizes were considered and compared to a finer reference mesh of more than 2,500 elements. Finally, 139 finite elements with cubic shape functions were used, comprising about 15,000 degrees of freedom, depending on the size and position of the bubble in the domain. This ensured that the displacement field calculated was within 2% of the values obtained with the finer reference mesh and yielded a computational time that was 75 times shorter.

The average runtime of a calculation was about two minutes on a 4-core Intel processor at 3.1 GHz, with 16 GB RAM.

2.4 SENSITIVITY ANALYSIS

The aims of the sensitivity analyses performed in this study were:

- To determine the input parameters that were most influential on the model output;
- To quantify the impact of the variability of these parameters on the model output and this was also used as a way to propagate the error on the model parameters in the solution of the problem.

Sensitivity analysis based on statistical methods requires a high number of calculations as the number of parameters studied increases. In our case, the input parameters included the Maxwell model parameters, the geometric parameters (such as bubble position H_b) and the pressure applied to the bubble surface. A first screening method was therefore used to rule out the parameters that had the least influence on the model output values (section 2.4.1).

The two model output values that were studied were the bubble volume and the displacement of the center of the deflected shape of the upper surface of the domain (section 2.2.3).

The two types of sensitivity analysis were performed using the above COMSOL Multiphysics model in a script written in Matlab (The MathWorks, USA). This made it possible to script the calculations with a greater level of control over the model parameters.

2.4.1 *Screening method*

Three values were used for each input parameter: the reference value, a lower and an upper value (Table 3.2). The variation range studied for each parameter (Table 3.2) was defined to reproduce variations that could be observed physically and that were caused by variability of the product studied, or errors in the assessment of the parameters, either of experimental nature or originating from calculation and fitting steps. The pressure applied on the bubble consisted of a 3 kPa hold (this is a plausible pressure level observed in cheese) for 10 h followed by null pressure for 17 h. Parameters were ranked according to:

$$I_k = 100 \frac{\left| \frac{f\left(X_k^{max}\right) - f\left(X_k^{ref}\right)}{f\left(X_k^{ref}\right)} \right| + \left| \frac{f\left(X_k^{min}\right) - f\left(X_k^{ref}\right)}{f\left(X_k^{ref}\right)} \right|}{\left| \frac{X_k^{max} - X_k^{ref}}{X_k^{ref}} \right| + \left| \frac{X_k^{min} - X_k^{ref}}{X_k^{ref}} \right|} \tag{3.8}$$

where f is the model output being considered (bubble volume or deflected shape of the upper surface), and X_k^{ref}, X_k^{min}, and X_k^{max} the reference, minimum, and maximum values of parameter k, respectively. The higher the I_k, the higher the sensitivity. f was calculated at a simulated time of 100 ks (27 h) in order to consider only the long-term behaviour. The ranks were considered as a first order approximation of the influence of variation in the parameters on output values.

2.4.2 *Statistical method*

The method was split into two parts: the use of response surface methodology to approximate the solution to the problem, and estimation of the sensitivity indices as defined by Sobol [86].

The output of the model f was approximated by a quadratic response surface y:

$$f(\boldsymbol{X}) \approx y(\boldsymbol{X}) = c + \sum_{i=1}^{n} a_i X_i + \sum_{i=1}^{n-1} \sum_{j=i+1}^{n} b_{ij} X_i X_j + \sum_{i=1}^{n} b_{ii} X_i^2 \tag{3.9}$$

where X is the vector containing the model parameters, n the number of parameters, and c, a_i, and b_{ij} the coefficients that need to be fitted. To determine these coefficients, simulated data were generated using COMSOL Multiphysics, following a 3^n factorial design, and the coefficients were fitted by multilinear regression using the regstats Matlab function. The RMSE between the response surface y and the COMSOL model was 5%.

The first-order sensitivity indices S_i for each parameter were then calculated according to:

$$S_i = \frac{\mathrm{Var}\left(\mathbb{E}\left(y|X_i\right)\right)}{\mathrm{Var}(y)} \tag{3.10}$$

where $\mathbb{E}$ is the mathematical expectation and Var the variance. The second-order sensitivity indices S_{ij} were also calculated to estimate the impact of the interaction between the model parameters X_i:

$$S_{ij} = \frac{\mathrm{Var}\left(\mathbb{E}\left(y|X_i, X_j\right)\right) - \mathrm{Var}\left(\mathbb{E}\left(y|X_i\right)\right) - \mathrm{Var}\left(\mathbb{E}\left(y|X_j\right)\right)}{\mathrm{Var}(y)} \tag{3.11}$$

The variances stated in Eqns. 3.10 and 3.11 were calculated with the Monte-Carlo method on 100,000 drawings of y. Contrary to the screening study, the sensitivity indices were calculated at two separate times: $t = 100$ s and $t = 100$ ks, reflecting both the short- and long-term behaviour of the model.

3

RESULTS AND DISCUSSION

3.1 SENSITIVITY ANALYSES

The results from the screening study (Table 3.2) allowed us to eliminate from the mechanical parameters those that had the least influence on the output levels, namely: α_1, α_2, α_3, λ_1, λ_2 and λ_3.

The remaining parameters were then submitted to a finer sensitivity study.

Table 3.2: Highest and lowest, and reference values for input parameters in the frame of the screening analysis, and selection of the most sensitive parameters (in bold).

Parameter	H_b (mm)	E (kPa)	α_1	α_2	α_3	α_4	α_5	λ_1 (s)	λ_2 (s)	λ_3 (s)	λ_4 (s)	λ_5 (ks)
Reference value	20	150	0.58	0.20	0.12	0.07	0.03	0.15	3	40	600	10
Minimal value	15	125	0.50	0.17	0.08	0.05	0.01	0.10	2	20	400	5
Maximal value	22.5	175	0.65	0.25	0.16	0.10	0.05	0.20	4	60	800	15
I_k (bubble volume)	**18.9**	**34.4**	0.3	0.3	0.3	**4.0**	**46.8**	0.0	0.0	0.54	**2.7**	**37.0**
I_k (deflected shape)	**460**	**92.2**	0.3	0.5	1.9	**25.0**	**74.7**	0.1	0.4	2.7	**7.2**	**14.9**

The first-order sensitivity indices were calculated at two separate times of simulation ($t = 100$ s and $t = 100$ ks) and are presented in Figure 3.3. Handling of cheese blocks during ripening may generate rapid strain of the material; whereas bubble growth during ripening is very slow. This is why results in the short term were considered together with results in the long term.

In the long-term (100 ks):

- The proportion of the 5th Maxwell element – which had the highest relaxation time – did not exceed 5% for the material studied. Despite its small proportion, the sensitivity study showed high influence of the 5th Maxwell element on final bubble volume (Figure 3.3a).
- The 4th Maxwell element and the z-position of the centre of the bubble H_b failed to show any influence on long-term bubble volume.
- The z-position of the centre of the bubble, and the 5th Maxwell element were the parameters that had the most influence on the deflected shape of the upper surface (Figure 3.3b).

- The other parameters failed to show any influence on the deflected shape of the upper surface.

In the short-term (100 s):

- The parameters with the most influence on bubble volume were Young's modulus E and the two proportions α_4 and α_5 (Figure 3.3a). Since the proportions were related to the elastic modulus, this globally confirmed the expected influence of elastic parameters on short-term loads.
- The relaxation times and the z-position of the centre of the bubble showed weak influence on bubble volume.
- The parameters with the most influence on the deflected shape of the upper surface were the z-position of the centre of the bubble and, to a lesser extent, Young's modulus.
- The 4^{th} and 5^{th} Maxwell elements failed to show any influence on the deflected shape of the upper surface.

The second order sensitivity indices showed that, compared to first order indices, the interaction between parameters could be ignored (Figure 3.4). Among the interactions considered, only the interaction between α_5 and λ_5 was significant. This confirmed the relevance of the screening approach, as the parameters can be considered separately from each other.

To conclude, the uncertainties on the 5^{th} Maxwell element, Young's modulus and z-position of the bubble H_b were propagated in the simulations (e.g. in Figure 3.7), as they proved to have high sensitivity indices (Figure 3.3). Their range of variations was consistent with that specified in the material and methods section (Table 3.1) and hence rather smaller thant that used above for the sensitivity study .

3.2 EXPERIMENTAL VALIDATION

Comparison of the simulated and experimental deflected shapes of the upper surface suffers from the initial irregularity of the upper surface (Figure 3.6). It is in fact difficult to obtain a plane, due to the tools used to cut the cheese sample, and the unwanted stress when fitting the sample in the maintaining apparatus that caused vertical strain. For instance, the sample in Figure 3.6b presented a strain at $t = 0$, with a 500 µm shift in z-position for radii comprised between $r = -10$ and $+20$ mm. Therefore, the displacement of the middle of the upper surface ($\Delta z_{us}(r = 0)$) vs. time (Figure 3.7bdf) was used; the initial actual position of the upper surface rather than the expected position was used as reference. This facilitated the comparison between simulated and experimental results on the upper surface.

There was good agreement between the model and the experiment (Figure 3.7). Propagation of uncertainties of input parameters in the simulations yielded variations for the output levels that were as high as 27% for bubble volume (Figure 3.7a) and as high as 53% for displacement at the centre of the upper surface (Figure 3.7f). As discussed in section 3.1, this was explained mainly by the influence of the 5^{th} Maxwell element for the bubble volume, whereas for the displacement at the centre of the upper surface it mainly reflected the influence of uncertainty in the z-position of the bubble. Note that the original uncertainties on the input parameters were amplified on the output values 3- to 4-fold for bubble volume and nearly 10-fold for the upper surface displacement.

Over processing times in the order of 10 hours, the simulated bubble volume did not differ more than 9% on average from that observed experimentally at the same time. The simulated variations in bubble volume followed the variations in bubble pressure in the same manner as the experimental values, showing the ability of the model to reproduce the effects of rapid loads as well as slow loads.

Quantitative agreement on the displacement of the middle of the upper surface was not always reached, but the experimental dynamics were reproduced satisfactorily nevertheless. For Experiment 2, the simulated curve satisfactorily reproduced the behaviour observed experimentally (Figure 3.7d). For Experiment 3, the simulated upper surface followed the same kind of evolution as the experimental measurement, demonstrating again the ability of the model to reproduce the effects of rapid loads (Figure 3.7f). However, the model slightly overestimated the upper surface displacement, while remaining contained within the domain of confidence obtained for the simulations by propagating the uncertainties on the input parameters of major influence. This could be due to the vertical position of the bubble inside the cylinder that may differ between the model and the experiment due to experimental uncertainties. For Experiment 1 (Figure 3.7b) the simulated curve followed the same kind of variations as the variations in bubble volume observed in Figure 3.7a, but the model predicted an upper surface displacement that was more linear than the experimental ones. Nevertheless, there was a rather good agreement for the final displacement.

It should be emphasised that, for the purposes of our study, strict fitting of the curves was not sought for. Our approach aimed at implementing the simplest mechanical model to describe bubble growth in cheese, while keeping good agreement in terms of order of magnitude. Given the uncertainties on the input parameters, quantitative agreement was reached between experiments and simulations for bubble volume, without further need for adjustment of input parameters. Regarding the upper surface, quantitative agreement between experiments and simulations suffered severely from uncertainty on z-position of the bubble, but nonetheless remained in the same order of magnitude.

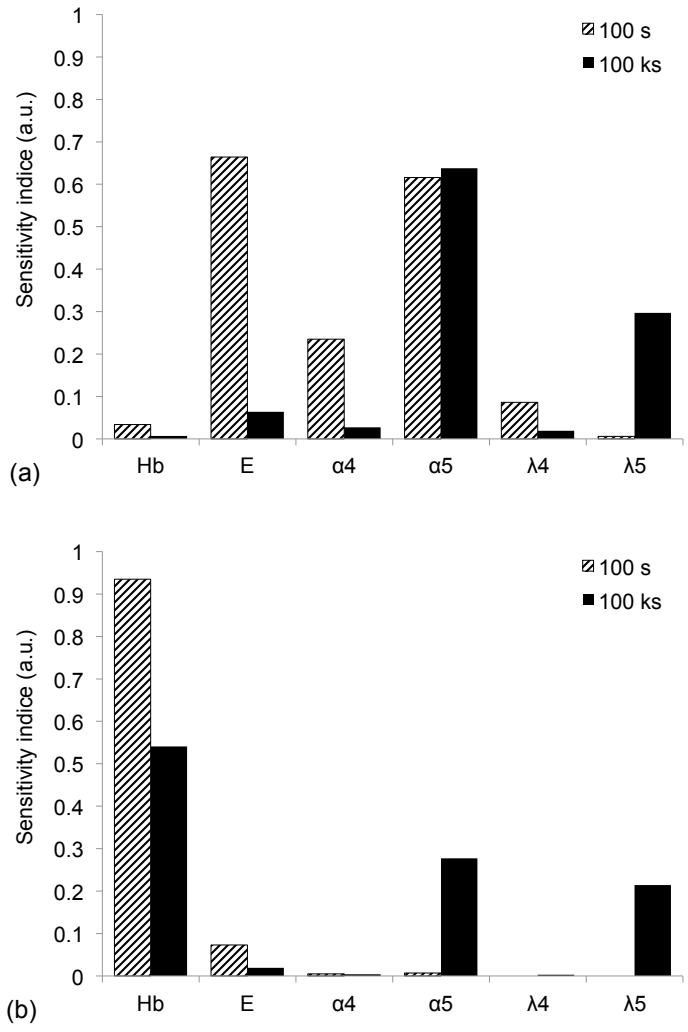

Figure 3.3: Sensitivity indices for the model parameters selected, at different simulation times. (a) sensitivity indices on the bubble volume, (b) sensitivity indices on the upside surface deflected shape. The higher the indices, the greater the influence of the parameter on the model output.

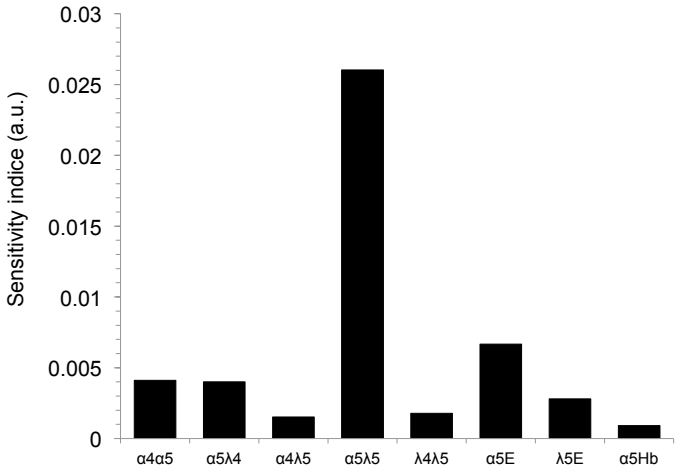

Figure 3.4: Selection of second order sensitivity indices for bubble volume, at $t = 100$ ks.

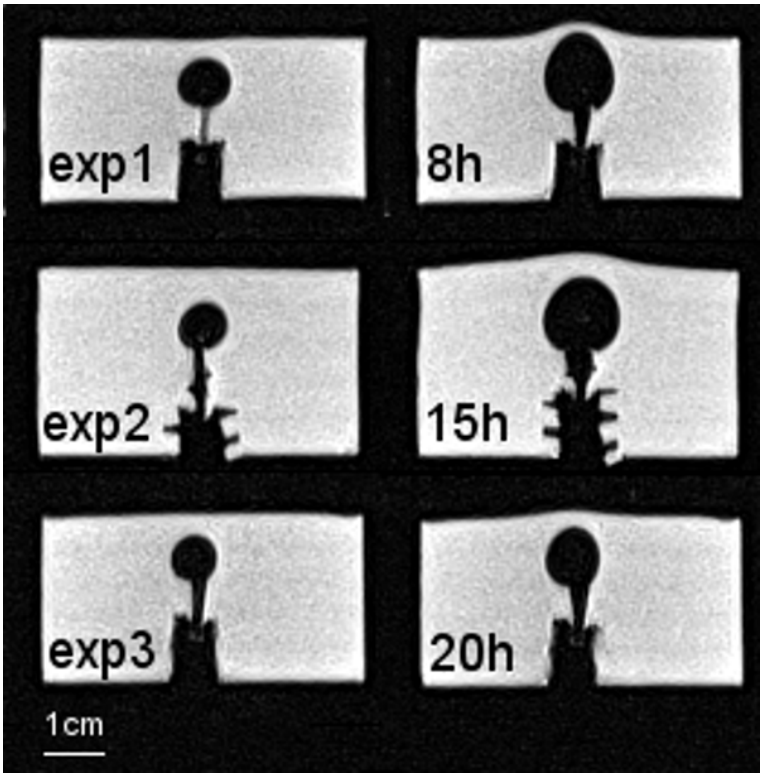

Figure 3.5: MRI cross-sections of the experimental set-up at the beginning (left) and end (right) of the experiment.

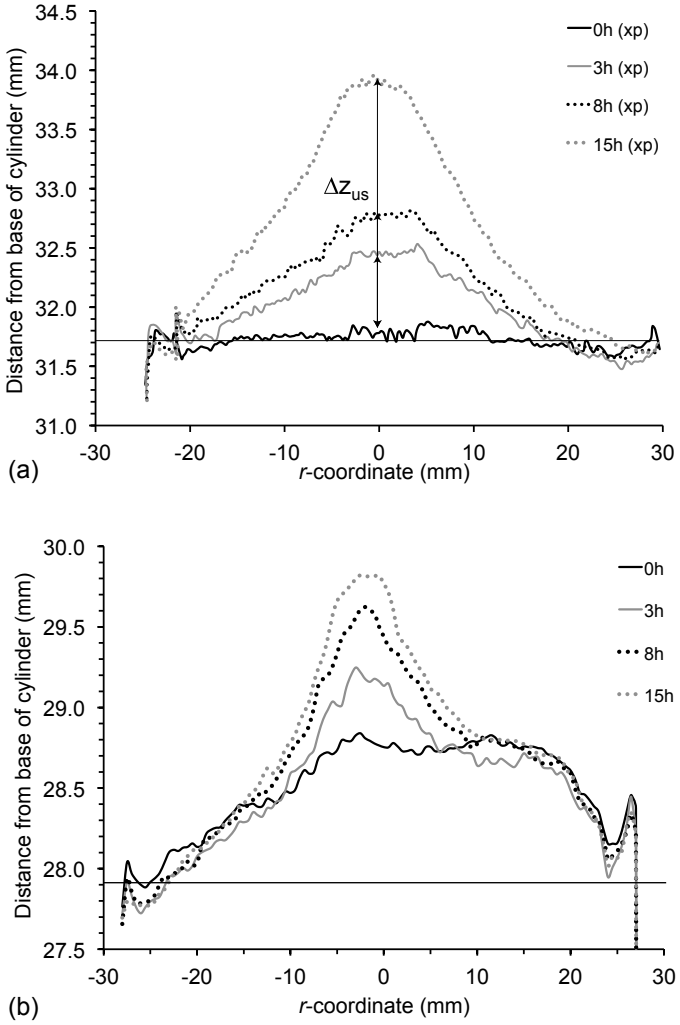

Figure 3.6: (a) Experimental deflected shape of the upside surface of cheese over time, with no apparent initial strain (Experiment 2); (b) Experimental deflected shape over time, with initial strain (Experiment 3). Uncertainties on the upside surface are not shown for clarity, but were estimated at ± 0.2 mm. Plain horizontal line denotes the expected height of the samples.

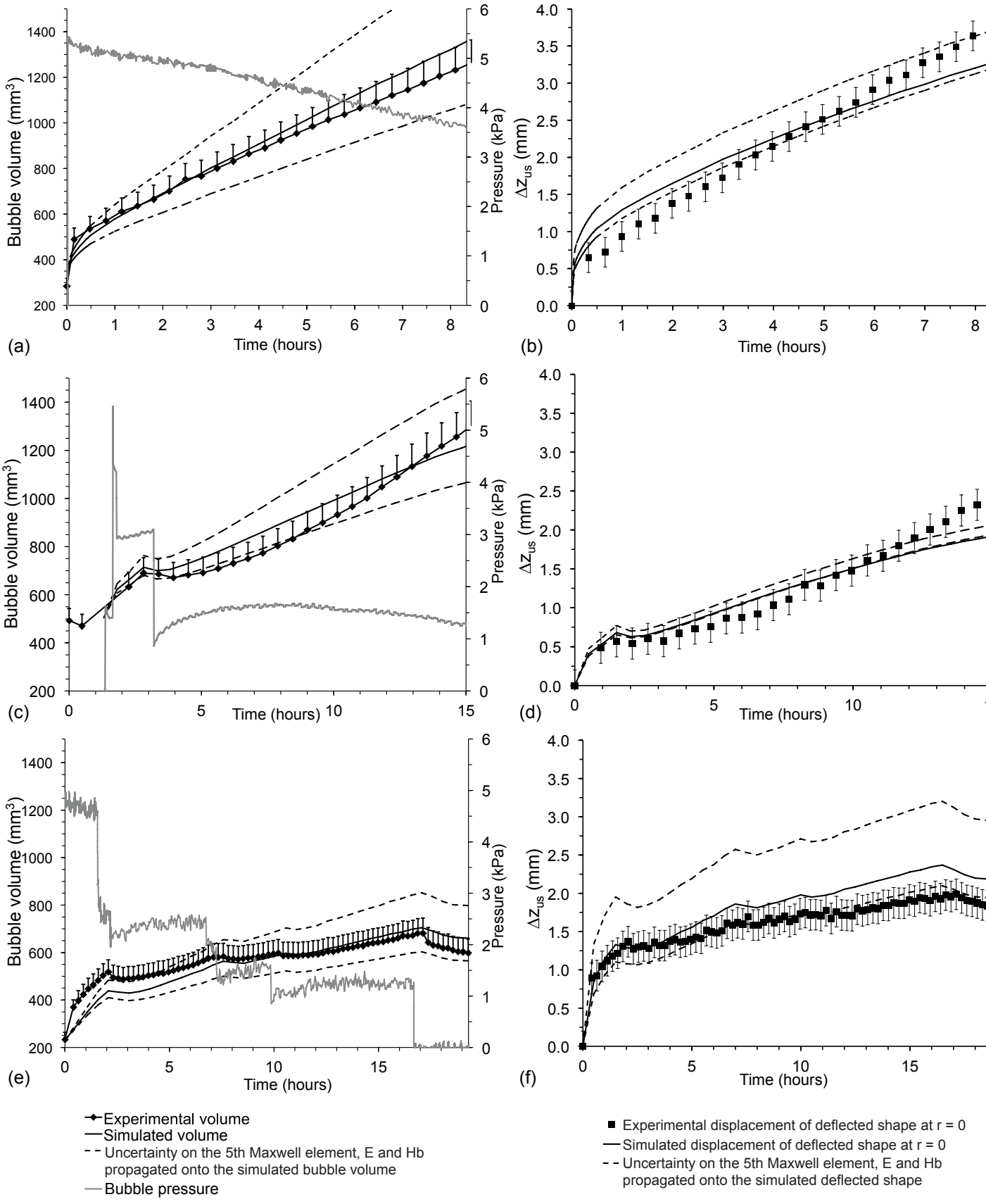

Figure 3.7: Experimental and simulated bubble volumes and headspace pressures (a, c, e) displacement of the middle of the upside surface (b, d, f) for Experiments 1, 2, 3 respectively. Due to combinatory effects, the propagation of uncertainties did not necessarily yield output curves that were centered on the reference ouput, especially for (b, d, f).

4

CONCLUSIONS

A model for mechanical deformation of a single bubble in semi-hard cheese material was proposed. The model was implemented to respect the experimental configuration as far as possible. Two types of output were considered: bubble volume and displacement of the upper surface of the cheese cylinder surrounding the bubble.

A sensitivity study was performed to evaluate the influence of the model input parameters on the model output parameters. It showed that the parameters of the Maxwell element that had the longest relaxation time (α_5 and λ_5) were responsible for the long-term behaviour of the bubble. This was in agreement with the results of Feng and Bertelo [29] on polymer foams, that used an Oldroyd-B model. This also confirmed that special care should be taken when characterising the behaviour of this type of cheese to ensure that the parameters of the Maxwell element that have the longest relaxation time are determined with sufficient accuracy to limit the propagation of uncertainties in the simulated data. Enhancing accuracy could be achieved by considering relaxation experiments of at least 3 to 5 times the order of magnitude of the longest relaxation time. However, such an experiment would require sensitivity in the force measurement, as well as a specific device to guarantee the integrity of the cheese sample for such long durations. The use of a creep-recovery test might complement and increase understanding of the actual meaning of this longest relaxation time.

Rapid and long-lasting loads were imposed on the bubble in order to mimic plausible situations within cheeses: rapid loads mirrored the sudden change on handling in the ripening room temperature while long lasting loads mirrored the natural bubble growth due to microbial activity. Given the uncertainties in the experimental data, the simple model proposed in this study was proved to reproduce the experimental situations satisfactorily, in particular for bubble volume. Validation of this model allows further development of the model to include mass transport phenomena that are responsible for bubble growth in semi-hard cheeses. This stage will include at least four additional input parameters (carbon dioxide diffusivity, Henry's constant, carbon dioxide production rate and initial carbon dioxide concentration in cheeses). Some of these will be characterised in the conditions of the experiment and others taken from the literature. This more complete model will be validated against new sets of data involving free inflation of the bubble. In accordance with the results from the present study, discrepancies between these future experiments and model larger than 10% will be assigned to the physics of mass transport and the associated values of input parameters.

ACKNOWLEDGMENTS

Compression-relaxation tests on cheese were performed at the JRU Genial, Paris, directed by Camille Michon. The authors wish to thank her for this contribution to the work, as well as Gabrielle Moulin for technical assistance.

This study was carried out with financial support from VALORIAL and the Regional Councils of Bretagne, Pays de Loire and Basse-Normandie. The first author, Yannick Laridon, is the holder of a grant from INRA ansd Irstea.

Chapitre 4

SIMULATION OF BUBBLE GROWTH IN SEMI-HARD CHEESE WITH MASS AND MOMENTUM TRANSPORT: COMPARISON WITH EXPERIMENT AND SENSITIVITY ANALYSIS

The growth of a single bubble within a semi-hard cheese cylinder was investigated both experimentally and by numerical simulation. Two transport phenomena were modelled: mass and momentum transport, and simulation results were compared to the average bubble growth in industrial cheeses that were acquired with help of MRI imaging. The proposed model proved to be able to describe the bubble growth in a qualitative manner. A sensitivity study was conducted to determine the most influent input parameters on the bubble growth. The mechanical parameters did not proved to have a significant influence over bubble growth compared to the mass transport properties (carbon dioxide production and carbon dioxide diffusivity), that proved to be the most important parameters.
Keywords: multiphysics modelling, mass transport; sensitivity analysis

1 INTRODUCTION

Whilst bubbles are found in numerous food products (Campbell and Mougeot 15), the modelling of bubble growth for foodstuff is almost exclusively limited to the study of sparkling beverages or cereal products. The studies of the first are heavily inspired by cavitation studies in liquids, while for the latter, the studies are inspired by the works on polymer foaming. The dynamics involved for the growth of bubbles in cheese during ripening encourages considering the present study as a continuation of works on dough proofing.

Bubble growth in polymeric foams is caused by diffusion of gas following a sudden supersaturation of a given gas in a liquid, and can be controlled by several aspects of the foaming process: polymeric reactions, geometric and temperature conditions, blowing agent used, etc. (Amon and Denson 5). Nucleation can be caused either by a boiling regime (homogeneous nucleation), by the presence of nucleating agents (heterogeneous nucleation), or by a combination of both (Jones et al. 50). However, the present study did not consider nucleation but focused on the subsequent bubble growth, with an already significant size in diameter (higher than 4 mm).

Modelling of bubble growth in polymers covers coupling between mass and momentum transport, and often considers multiple bubbles by generalising the 1-D cell model proposed by Amon and Denson (5). If heating is involved in the process under study, energy transport can be included (Alavi et al. 4, Lee et al. 62). Few modelling studies on aerated cereal products went to the extent of characterising the growth in cereal products at the bubble scale (de Cindio and Correra 23, Fan et al. 28, Hailemariam et al. 39, Shah et al. 85), this selection encompassing both modelling studies on proving and baking. The dough is often thought of as a purely viscous material, but some studies considered viscoelastic models. De Cindio and Correra (23) considered the dough with a linear viscoelastic model very similar to that used in the present study. They proved that, contrary to the viscous models, the use of viscoelastic constitutive equations allowed to reproduce cases that had asymptotic bubble volumes due to the time-independent elastic properties of their viscoelastic modelling. Some other studies considered non-linear viscoelastic models, such as the Lodge model used by Hailemariam et al. [39], that give a better description of the material behaviour, but necessitate a more time consuming evaluation of the input parameters (for the Lodge model it enforces the knowledge of memory function for the material). They found that viscoelasticity of the dough tends to prevent bubbles from collapsing.

Mass transfer was proved to be the main contributing factor to bubble growth during proving (Hailemariam et al. 39, de Cindio and Correra 23). Mass transport in the liquid phase can be modelled by Fick's law and applied to the phases where carbon dioxide is soluble (liquid water and liquid fat in the case of cheese, Jakobsen et al. 48). Exchanges at the bubble-material interface are often described using the Henry's law. Shah et al. [85] discussed the influence of the carbon dioxide saturation on the bubble growth, and showed that for subsaturation regime, bubbles were to have an asymptotic size, that was influenced mainly by the initial bubble size and carbon dioxide concentration. For supersaturation regime, they showed that above a critical size, bubble growth would happen indefinitely. No asymptotic bubble size could be observed in the same type of cheese like that studied in this paper (Huc et al. 44) evidencing that supersaturation also happens in the semi-hard cheese under study.

Despite the similarity of the driving phenomena between bread dough proving and cheese ripening, some differences have to be underlined. The growth kinetics are substantially higher for cereal products: the bread making process takes several hours, whereas it takes several weeks of ripening for semi-hard cheese. This discrepancy in the kinetics may be explained by differences in the microbiological phenomena involved. Carbon dioxide production in semi-hard cheese is caused by propionic fermentation, whereas it is caused by alcoholic fermentation for bread dough, and the optimal conditions of carbon dioxide production, in terms of temperature or pH for instance, highly differ between the two processes. The bubble growth kinetics is also influenced by the mechanical behaviour of the material surrounding the bubbles. Although both materials (dough and cheese) are viscoelastic materials with similar relaxation time spectrum (Keentok et al. 51), viscoelasticity of cheese is one to two orders of magnitude higher than that of cereal doughs (Launay and Michon 59). At last, bread dough is also a highly porous product: about 70-80% in porosity, compared to about 10% for semi-hard cheeses; it involves bubbles that are smaller (a couple of millimetres at the end of proving, compared to a couple of centimetres at the end of cheese ripening), and for which surface tension may not be negligible.

Experimental validation of the models focused on dough, when implemented, often took place at a macroscopic level, by using overall morphologic descriptors (Fan et al. 28, Chiotellis and Campbell 16). Both characteristic size of bubble and their rate of growth in cheese are compatible with tomographic monitoring, hence offering the possibility to validate the modelling at a single bubble level.

For appropriate validation, the model of transport has also to be fed with values of several input parameters, specific for semi-hard cheeses, such as carbon dioxide diffusivity, solubility and production rate. Characterisation of these parameters for cheese is sparsely covered in the literature, despite a great interest from the cheese-making community. There is, as far as we know, no paper dedicated to the estimation of carbon dioxide diffusivity in semi-hard cheese. Numerous studies, however, were done on modified atmosphere packaging, and covered the exchange of carbon dioxide at

the product interface. The interest of these studies is to provide data on interfacial transfers for a wide variety of products, for instance the work on Swiss-type cheese by Blanc et al. [10]. If such studies give a hint of the carbon dioxide production within cheese, they fail to disentangle the respective influence of diffusion and production within the product by focusing on the interface only. Rodriguez-Aguilera et al. [80] and Vivier et al. [91] successfully estimated carbon dioxide production rate, but their study was applied to soft cheeses, for which the fermentation mechanism differed from that of semi-hard cheeses. In semi-hard cheeses, the carbon dioxide production originates from propionic fermentation, but also from proteolysis (to a lesser extent, only 20%, Actilait 1). Propionic fermentation is a well-described phenomenon, and the influence of various process-related factors has already been covered, such as salt content (Boyaval et al. 11, Huc et al. 45), type of bacterial strain (White et al. 92) or temperature (Richoux et al. 79). These factors can induce huge variations in the microbial activity, and may therefore, among other parameters, influence the carbon dioxide production within the cheese (Huc et al. 45). At last, some studies have estimated the carbon dioxide solubility in cheese, but on the whole cheese block, and only at the end of the ripening (Seuvre and Mathlouthi 84, Jakobsen et al. 48).

The purpose of the present paper was to model the coupled momentum and mass transport in the case of a single bubble growth in semi-hard cheese. Indeed, the mechanics involved in the bubble growth were already validated on a separate experiment involving known pressure forces (Laridon et al. 58) , allowing the focus of the present study on mass transport and its coupling with momentum transport. The study aimed at sorting out model parameters that are the most influential on bubble growth. This was based on a compilation of literature data for input parameters but also on the measurement of carbon dioxide production rate in our specific case. The bubble growth monitored by MRI (Magnetic Resonance Imaging) and X-Ray Imaging on industrial cheese blocks during ripening (hot room) served as the reference for this discussion.

2

EXPERIMENTAL PROCEDURE AND DATA ANALYSIS

For experimental validation of the model, cheese blocks were taken from the plant at the end of the brining step and ripened in the lab at two successive controlled temperatures: 285 K (during 8 to 10 days) and 293 K (during 15 days). Temperature was maintained constant using maturing cabinets (Grand Cru, Liebherr, France). For all the followings, the initial time $d = 0$ refers to the time at which the temperature of the ripening rooms was changed from 285 K to 293 K.

At each time chosen in the ripening process, one cheese block was taken out of the ripening room and images were acquired, either by X-ray or MRI imaging, on the whole cheese block, following the method developed by Musse et al. [68]. For each experimental campaign, the time-course changes in bubble volume was averaged over two regions of interest (ROI) that are under the rind and at core of the cheese blocks. The dimensions of these regions are 16 × 16 × 1.5 cm, the first one being situated 1 cm under the rind and the second 4 cm. Since the position of the rind evolves with the inflation of bubbles during ripening, the location of these regions changed with respect to the fixed referential. Bubbles were considered to be in a given ROI if their barycentre belonged to it. Bubbles which had volumes lower than 10 mm^3 and presented no growth during ripening were omitted. Standard deviation was of great magnitude (ranging from 8 to 150%), representative of the high variability in bubble size and growth kinetics within the cheese block. More details about the image analysis can be found in Huc [46].

Table 4.1: Experimental configurations

	Run 1	Run 2	Run 3
Imaging technique	X-Ray	MRI	MRI
Replications	3	3	1
Days in cold room	10	8	8
Days in hot room	15	15	15

3

MODEL DESCRIPTION

Excepted when stated, values are given at 293 K and 101325 Pa.

3.1 GEOMETRY

In order to minimise computational cost, modelling was restricted to one bubble surrounded by a cylindrical volume of cheese (representative volume of cheese around one bubble). The bubble is assumed to be initially spherical. An axisymmetric representation of the problem was used (Figure 4.1).

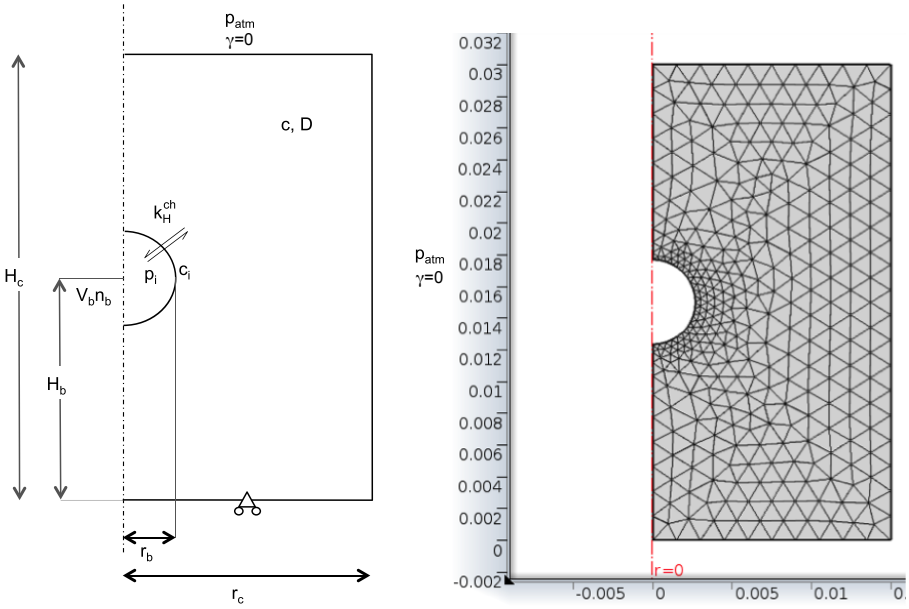

Figure 4.1: Axisymmetrical geometry used for modelling (left), and domain meshing (right)

3.2 HYPOTHESES

Cheese was considered nearly-incompressible, with a Poisson ratio ν at 0.49. Its composition (other than CO_2), mechanical and diffusive properties were considered homogeneous at the scale considered. Carbon dioxide was also considered to be produced homogeneously. Although carbon dioxide is soluble in the fat fraction of the cheese, diffusion of carbon dioxide in fat was considered to be negligible compared to that in the water phase, so that only carbon dioxide in the aqueous phase was considered. Within the bubble, pressure was considered uniform and gases other than carbon dioxide were neglected. Temperature was considered uniform and constant.

3.3 MECHANICAL BEHAVIOUR

The behaviour of the cheese was modelled with a 5-element generalised Maxwell model described earlier in a dedicated paper (Laridon et al. 57). The mechanical equilibrium was expressed through the conservation of momentum:

$$\nabla \cdot \sigma = \rho g \tag{4.1}$$

Stress was calculated as the sum of elastic and viscoelastic parts and the viscoelastic part was described by the Maxwell model. (Laridon et al. 57).

3.4 MASS TRANSPORT

Mass diffusion was described according to Fick's law; mass conservation writes as follows:

$$\frac{\partial c}{\partial t} - D^{ch}_{CO_2} \Delta c = r_{CO_2} \tag{4.2}$$

where c is the number of moles of carbon dioxide in the water phase of cheese by cubic meter of cheese, later denoted as the apparent carbon dioxide concentration in the domain, $D^{ch}_{CO_2}$ the apparent diffusivity of carbon dioxide in cheese (section 4.2) and r_{CO_2} the carbon dioxide production rate within the cheese domain (section 4.1). Carbon dioxide is also dissolved in the fat phase, but it was assumed, as a first approach, that this amount of carbon dioxide did not vary during bubble growth (no exchange with the aqueous and gaseous phases, no diffusion nor production in the fat phase).

The equilibrium at the gas-cheese interface was expressed according to Henry's law:

$$c_i = k^{ch}_H p_i \tag{4.3}$$

where c_i is the apparent carbon dioxide concentration at the interface, p_i the pressure exerted by the gas on the interface and k^{ch}_H the Henry's constant for carbon dioxide in cheese (section 4.3.1).

The atmospheric pressure p_{atm} is used as the reference pressure in the mechanical aspects.

3.5 COUPLING OF TRANSPORT PHENOMENA

The carbon dioxide flux at the gas-cheese interface j_i can be written as:

$$j_i = -D^{ch}_{CO_2} (\nabla c)_i \cdot \boldsymbol{n} \tag{4.4}$$

where $\boldsymbol{n}$ is the normal vector of the interface. This flux was numerically computed as:

$$j_i = \gamma \left(c_i - k^{ch}_H p_i \right) \tag{4.5}$$

where γ is the transfer coefficient at the interface. To ensure that the effect of diffusion in the cheese was limiting, the Biot number for mass transport was set at a high value (10^5):

$$Bi_m = \frac{\gamma L}{D^{ch}_{CO_2}} \tag{4.6}$$

This implied that γ was set at a high value and assured conditions very near to equilibrium ($\gamma \to \infty$ leads to Eq. 4.3). Characteristic length L was set at 20 mm, as it was the typical length between the gas-cheese interface and the boundaries of the domain (Figure 4.1).

The evolution with time of the quantity of CO_2 in the gaseous phase, $\frac{dn_b}{dt}$, was deduced from the CO_2 flux:

$$\frac{dn_b}{dt} = \int_{\Gamma_i} j_i dS_i \tag{4.7}$$

where Γ_i is the gas-cheese interface boundary and S_i its surface. Using Eqns. 4.5 and 4.7, and the ideal gas law, the following ODE was solved at the gas-cheese interface:

$$\frac{dn_b}{dt} = \gamma \int_{\Gamma_i} c_i dS_i - \gamma k^{ch}_H RT \frac{S_i}{V_b} n_b \tag{4.8}$$

where V_b is the volume of the gaseous phase (bubble). The quantity of CO_2 determined with Eq. 4.8 was used to calculate the pressure of the gas at the interface with the cheese domain, following the ideal gas law:

$$p_i = \frac{n_b RT}{V_b} \tag{4.9}$$

The pressure calculated by Eq. 4.9 was used as mechanical boundary condition at the gas-cheese interface (Eq. 4.11), and therefore constitutes the coupling between mass and momentum transports.

3.6 BOUNDARY CONDITIONS

Mechanical boundary conditions

In order to prevent unrealistic displacement of the domain, a roller boundary condition was applied at the lower surface:

$$\boldsymbol{u} \cdot \boldsymbol{n} = 0 \tag{4.10}$$

where $\boldsymbol{u}$ is the displacement field. Pressure calculated through Eq. 4.9 was applied at the bubble-cheese interface:

$$\boldsymbol{\sigma}_i \cdot \boldsymbol{n} = -\left(p_i - p_{atm}\right) \tag{4.11}$$

where σ_i is the stress applied to the gas-cheese interface.
All other boundaries were let free of stress.

Mass transport boundary conditions

There was no flux of CO_2 at the boundaries of the cheese cylinder, except at the interface with the bubble, where the flux calculated by Eq. 4.5 was used.

Under these conditions, the growth of a bubble is considered with no mechanical constraint other than that exerted by the cheese material itself (restricted at the boundaries of the cheese cylinder which contents a representative volume of cheese around one bubble). Mechanical interactions between adjacent bubbles were not reproduced. All the CO_2 produced in the cylinder diffuses toward the bubble; competition for CO_2 between adjacent bubbles, or large-scale diffusion between regions of low and high CO_2 content at the cheese block scale were not taken into account by the model.

3.7 INITIAL CONDITIONS

It is considered that at a time denoted by t_{sat} the cheese is saturated in CO_2. All the simulations began at this saturation time, with t defined as $t = d - t_{sat}$. The initial bubble radius r_b in the simulation was set at the average experimental value observed at that time.

Mechanical initial conditions

Equilibrium at the atmospheric pressure was considered, so that:

$$p_i\left(t = 0\right) = p_{atm} \tag{4.12}$$

Mass transport initial conditions

Following the initial saturation hypothesis, initial carbon dioxide concentration within the domain was defined as:

$$c\,(t=0) = k_H^{ch} p_{atm} \tag{4.13}$$

The initial CO_2 quantity in the bubble was calculated with the help of ideal gas law:

$$n_b\,(t=0) = \frac{p_{atm} V_b\,(t_{sat})}{RT} \tag{4.14}$$

3.8 NUMERICAL IMPLEMENTATION AND CALCULATIONS

The model was implemented in COMSOL Multiphysics (COMSOL AB, Sweden) using a 2-D axisymmetric geometry.

The domain was meshed using triangular elements and was refined near the bubble interface (Figure 4.1). Simulations were conducted from the time at which saturation in CO_2 is reached to the end of hot room ripening (15 days).

Bubble volume was estimated at each time step using the following integral on the gas interface:

$$V_b = -\int_{\Gamma_i} \pi r^2 \boldsymbol{n} \cdot \boldsymbol{e}_r dl \tag{4.15}$$

where $\boldsymbol{e}_r$ is the unitary base vector, in r-direction.

4

ESTIMATION OF VALUES FOR INPUT PARAMETERS

4.1 CARBON DIOXIDE PRODUCTION RATE

Carbon dioxide production rates, r_{CO_2}, were measured on the same type of cheese as that used in the experiment, both at core and under rind (same locations as mentioned in section 2 for the analysis of bubble volume). Cheese blocks used for these measurements were from different batches than those studied according to the protocol defined in section 2 (data for validation of the model); different batches were used to characterise the inter-batch variability.

About 20 cheese disks (2 mm thick at most) were deposited in a sealed bottle onto small grids of large mesh and separated from the other disks by a sustaining stand. The full device is detailed in Huc et al. [45]. The total mass of cheese disks in a bottle, m^{ch} (about 25 g), was measured before each experiment.

The bottles were initially filled with N_2 at atmospheric pressure, and placed in a temperature-controlled ambiance at 293 K. Nitrogen recreated the nonaerobic conditions of bacterial growth during cheese ripening and also avoid the growth of moulds.

The pressure of the gas within the bottle, $p(t)$, was monitored over duration relevant of the ripening process (hot room). The time-course changes in pressure were attributed to the production of carbon dioxide only. Measurements were assumed to be diffusion-independent, because of the very low thickness of the cheese disks.

The gaseous volume, V^{gas}, surrounding the cheese disks was estimated by subtracting the volume occupied by the cheese disks and the sustaining stand to the overall bottle volume. The bottle volume was determined by filling the bottle with water and calculating the volume by weighing the water. The number of moles of CO_2 produced at a given time per volume of cheese was deduced from the pressure, using the ideal gas law:

$$\text{produced } CO_2 = \frac{\rho^{ch}}{m^{ch}} \frac{(p(t) - p_{atm})\, V^{gas}}{RT} \tag{4.16}$$

The amount of CO_2 produced during the experiment relative to the cheese volume is presented in Figure 4.2.

At the very beginning of the experiment (until one day at most), a slight decrease in pressure could be observed and was attributed to the entrance of nitrogen into the cheese.

The carbon dioxide production rate was not constant over time. At the beginning of hot room (until 6 days in Figure 4.2) the production rate was 2 times lower than afterwards, both at core and under rind. Production rates reported in Table 4.2 were calculated by linear regression of experimental data obtained between days 2 and 4 for the first stage, and between days 7 and 14 for the second stage.

Table 4.2: Rate of CO_2 production in cheese ($mol \cdot m^{-3} \cdot s^{-1}$); standard deviations were calculated on 5 and 7 experimental curves for Stage I and Stage II (respectively), originating from two runs, and were attributed to the intra- and inter-batch variability.

$mol \cdot m^{-3} \cdot s^{-1}$	Stage I		Stage II		ratio between stages I and II
	mean	σ	mean	σ	
At core	$1.65 \cdot 10^{-5}$	29%	$3.56 \cdot 10^{-5}$	23%	2.7
Under rind	$5.02 \cdot 10^{-6}$	31%	$1.37 \cdot 10^{-5}$	11%	2.2
Ratio between core and under rind	3.3		2.6		

Several factors were investigated experimentally, the impact of salt content, and moisture content. Cheeses without salt yielded production rates that were up to 2.6 times as much as standard industrial cheeses (Huc et al. 45), whereas for the two moisture contents considered (42 and 46%), there was no impact on the production rate. However, for cheeses that had the highest moisture content, production of carbon dioxide occurred 3 days after the change of room temperature.

Values reported in Table 4.2 were used as input parameter r_{CO_2} in the bubble growth model. Average change of production rate time t_r was calculated over 10 experimental curves, comprising both under rind and core data, at 5.5 ± 1.9 days.

4.2 CARBON DIOXIDE DIFFUSIVITY

Diffusivity of carbon dioxide in cheese $D^{ch}_{CO_2}$ was calculated from carbon dioxide diffusivity in water $D^{w}_{CO_2}$ (Davidson and Cullen 22), weighted by the volume fraction of water in cheese X^w and the tortuosity of the cheese material $\mathcal{T}$:

$$D^{ch}_{CO_2} = X^w \frac{D^{w}_{CO_2}}{\mathcal{T}} \tag{4.17}$$

Tortuosity was assumed to be at $\pi/2$ due to the presence of protein and fat globules. X^w was set at 0.42, considering that all the water present in the cheese material is available for CO_2 diffusion. This yielded $D^{ch}_{CO_2} = 4.51 \cdot 10^{-10} m^2 \cdot s^{-1}$, compared to $1.68 \cdot 10^{-9} m^2 \cdot s^{-1}$ for $D^{w}_{CO_2}$.

4.3 CARBON DIOXIDE CONCENTRATION IN CHEESE AND SATURATION

Here are considered values in cheese material and in pure water.

4.3.1 *Estimation of CO_2 saturation*

CO_2 concentration at saturation can be estimated from the Henry's constant value reported in the literature. Temperature dependency of k_H^w is given by:

$$k_H^w = k_H^w\left(T_{std}\right) \exp\left(-\frac{\Delta H}{R}\left(\frac{1}{T} - \frac{1}{T_{std}}\right)\right) \tag{4.18}$$

where T_{std} = 298 K, T is the temperature of the hot room in the ripening process (293 K), $k_H^w\left(T_{std}\right)$ =2.92·10^{-4} mol·m^{-3}·Pa^{-1} (Sander 82), and ΔH the standard enthalpy set at 1.995·10^{-4} J·mol^{-1} (Sander 82), R is the ideal gas constant (8.314 J·mol^{-1}·K^{-1}). Henry's constant equivalent for the cheese considered can be determined from the Henry's constant for CO_2 in pure water, using Eq. 4.19:

$$k_H^{ch} = X^w k_H^w \tag{4.19}$$

where X^w is the volumetric fraction of water in cheese (0.42).

Total pressure within the bubbles is of the same order of magnitude than the atmospheric pressure, with a slight overpressure (about 2%, Grenier et al. 37), and the bubbles contain mainly carbon dioxide. CO_2 concentration at saturation in pure water s^w under the same conditions is given by:

$$s^w = p_{atm} k_H^w \tag{4.20}$$

where k_H^w is Henry's constant value. This yielded a value of 29.6 moles of CO_2 per m^3 of pure water at 293K. CO_2 concentration expected at saturation in the water phase in cheese s^{ch} was found to be equal to 12.45 moles of CO_2 per m^3 of cheese.

4.3.2 *Estimation of CO_2 concentration directly on cheese material*

In Danish semi-hard cheese after equilibration with carbon dioxide

Carbon dioxide concentration was estimated by a titration method (Jakobsen et al. 48). Cheese samples extracted from semi-hard cheeses ready to be sold (hence for which ripening was advanced and stopped by low temperature) and equilibrated with different levels of partial pressure of carbon dioxide. After equilibration, these samples were put in perchloric acid solution in a Buchner connected to another Buchner containing $Ba(OH)_2$. This stage lasted about 20h, and then the dissolved CO_2 in the precipitate was estimated with HCl titration. Concentration x_{CO_2} was expressed as a volume of

carbon dioxide per mass of cheese. For semi-hard cheeses at 293 K and with a partial pressure of carbon dioxide equals to the atmospheric pressure, they found values of 0.5 10-3 $m^3 \cdot kg^{-1}$, that were consistent with previous results on Swiss-type cheeses by Pauchard et al. [73]. In order to be expressed in $mol \cdot m^{-3}$, the following conversion was performed:

$$s_{CO_2}^{w+fat} = x_{CO_2}(t_\infty) \frac{\rho_{CO_2} \rho_{ch}}{M_{CO_2}} \tag{4.21}$$

where ρ_{ch} =1030 $kg \cdot m^{-3}$, M_{CO_2} =4.4·10-2 $kg \cdot mol^{-1}$, ρ_{CO_2} =1.842 $kg \cdot m^{-3}$ (Perry 75). This yielded a concentration value at saturation of $s_{CO_2}^{ch}$ = 22 mol·of CO_2 per m^3 of cheese. Note that this amount of carbon dioxide is located both in the water and fat phases.

In semi-hard cheese used in this study

Carbon dioxide concentration was measured by a titration method similar to that used by Jakobsen et al. [48] on the same type of cheese as that used in the experiment, both at core and under rind (same locations indicated in section 2) at the very beginning of the hot room. Concentration x'_{CO_2} was expressed in moles of carbon dioxide per kg of cheese, the values were therefore converted in $mol \cdot m^{-3}$ with the cheese density:

$$c_{CO_2}^{w+fat}(d=0) = x'_{CO_2}(d=0)\rho_{ch} \tag{4.22}$$

where ρ_{ch} is also set at 1030 $kg \cdot m^{-3}$. This yielded the following concentration values, 16.1 ± 1.4 and 20.6 ± 1.5 moles·of CO_2 per m^3 of cheese under the rind and at core respectively. The standard deviation corresponded to the intra-batch variability. Reproducibility (inter-batch variability) was not characterized.

4.3.3 *Comparison between experimental CO_2 concentration and expected concentration at saturation*

On the one hand, carbon dioxide in cheese is dissolved both in water and fat phases. Measured carbon dioxide concentration in cheeses can be compared with the theoretical value by estimating the amount of carbon dioxide dissolved in the fat phase. Considering that, at the temperature under study, carbon dioxide concentration in the fat phase is approximately equal to that in the water phase as assumed at saturation by Jakobsen et al. 48:

$$c_{CO_2}^{w+fat} = \left(X^w + X^{fat}\right) c_{CO_2}^w \tag{4.23}$$

where $c_{CO_2}^w$ is the theoretical carbon dioxide concentration in the water phase.

On the other hand, for the simulations, the apparent carbon dioxide concentration c was used, that is the amount of carbon dioxide dissolved only in the water phase per cubic meter of cheese. Therefore:

$$c = X^w c^w_{CO_2} \tag{4.24}$$

Using Eqns. 4.23 and 4.24, this apparent concentration can be deduced from the carbon dioxide concentration measured on semi-hard cheeses as follows:

$$c = \frac{X^w}{X^w + X^{fat}} c^{w+fat}_{CO_2} \tag{4.25}$$

Note that the same conclusions were drawn whatever the mode of calculation of the concentration data (apparent concentration in cheese, or in water phase only). In other words, the statement of saturation was not affected to a large extent by considering the water phase alone.

Industrial cheeses studied during the present work were considered to be saturated in CO_2 at core but not under rind at the beginning of the hot room ripening (Table 4.3). Measurements at this stage of ripening were surprising since it is commonly recognised that the metabolism of propionic bacteria is low at the temperature of the cold room (Hettinga and Reinbold 42). However, it was consistent with the order of magnitude of the bubble sizes encountered in the very beginning of the hot room, also indicating that saturation was reached.

Measurements performed by Jakobsen exhibited slight supersaturation compared to the saturation level deduced from that in liquid water (5%). It is difficult to further discuss these data since some information is not reported in the up-cited paper, such as the duration of equilibrium with gas standards prior to titration or how the experimental procedure got rid of carbon dioxide production in cheese.

Table 4.3: Compilation of CO_2 concentration values measured in semi hard cheese or estimated from its composition, expressed in moles of CO_2 per m^3 of cheese

	Semi-hard cheese under study $(d = 0)$		Danish semi-hard cheese [48]	Deduced from saturated water		
	core	under rind		core	under rind	
X^w	0.42	0.40	0.47	0.42	0.40	0.47
X^{fat}	0.27	0.27	0.11	0.27	0.27	0.11
$c^{w+fat}_{CO_2}$	20.6	16.1	21.6	20.5	19.9	17.2
c	12.5	9.6	17.5	12.5	11.9	13.9

$c^{w+fat}_{CO_2}$: moles of carbon dioxide in water and fat phases per cubic meter of cheese, Eq. 4.23.
c : moles of carbon dioxide in water phase per cubic meter of cheese, Eq. 4.24.

4.4 MECHANICAL PROPERTIES OF CHEESE

Values of the parameters of the Maxwell model were fixed according to the average value that was determined on the same type of semi-cheese than the one under study. See section 2.4 of Laridon et al. [58].

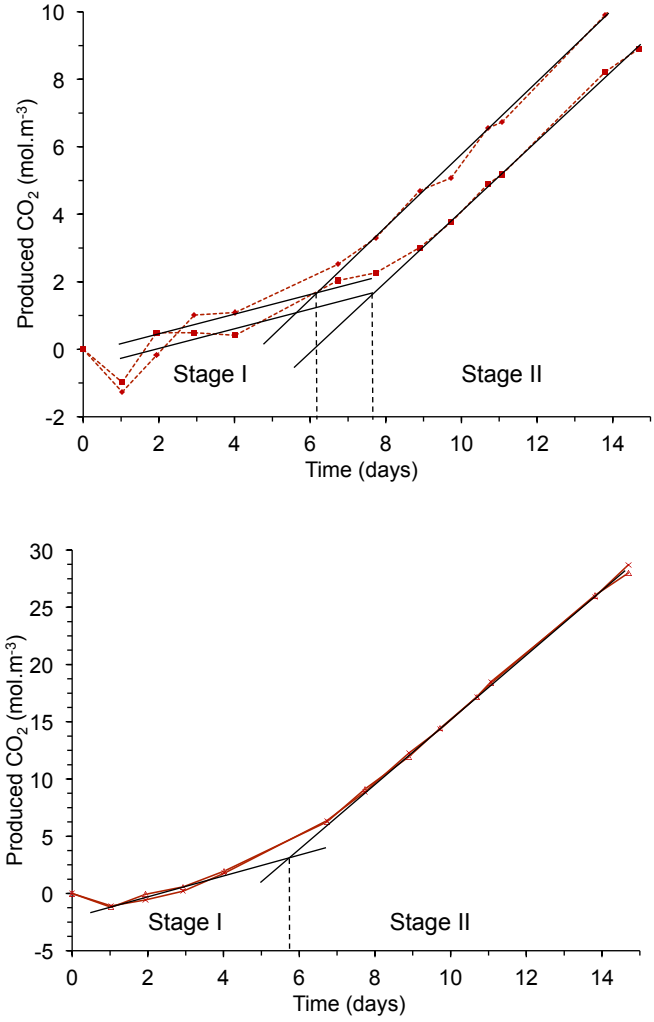

Figure 4.2: Carbon dioxide production under rind (top) and at core (bottom) at 293K. Two replications are shown for each graph, i.e. one bottle for each replication.

5

RESULTS AND DISCUSSION

A sensitivity study was performed in order to characterise the relative influence of the model inputs on the outputs *i.e.* the bubble growth. The objective was, if necessary, and despite the care paid to the estimation of input parameters, to adjust the value of one input parameter most influential and for which the estimate was not enough accurate. Table 4.4 summarises the upper, lower and reference values used for each input parameter. Each parameter was varied separately, all other parameters being kept at their reference values.

Reference values of the input parameters reported in Table 4.4 were relevant of the core of the cheese block. For the mechanical aspects, only the relaxation properties of the last Maxwell element were considered, as they proved to be the most influential parameters on bubble growth (Laridon et al. 58); their variations corresponded to the inter-batch variability. Diffusivity was swept with a +50% and -75% variation to cover extreme variations in diffusivity within the cheese, and to take into account that all the water contained within the cheese may not be available for the carbon dioxide to diffuse. Production rate was swept according to the inter-batch variability estimated in section 4.1, taking into account the highest standard deviation obtained between stages I and II. Since the inter-batch variability of t_{sat} was unknown, large variations in t_{sat} were tested in the sensitivity study, with two extremes values: the first considered the case when saturation is reached at the middle of the hot room ripening, the second considered the case when saturation is reached near the end of the ripening.

In order to rank the most influential parameters on bubble growth, sensitivity indices I_k were calculated for each input parameter X_k as:

$$I_k = 100 \frac{\left| \frac{V_b\left(X_k^{max}\right) - V_b\left(X_k^{ref}\right)}{V_b\left(X_k^{ref}\right)} \right| + \left| \frac{V_b\left(X_k^{min}\right) - V_b\left(X_k^{ref}\right)}{V_b\left(X_k^{ref}\right)} \right|}{\left| \frac{X_k^{max} - X_k^{ref}}{X_k^{ref}} \right| + \left| \frac{X_k^{min} - X_k^{ref}}{X_k^{ref}} \right|} \tag{4.26}$$

The sensitivity indices were assessed at the end of the simulations (15 days). These results are represented in Table 4.4. Some are also compared to the experimental data at the corresponding location (Figure 4.3).

The mechanical parameters of the 5th Maxwell element proved to be the less influential parameters over bubble growth, having sensitivity indices about 100 times lower than the most influential parameter (Table 4.4). Values of mechanical parameters typically encountered under rind (Laridon et al. 57) did not even oppose much more resistance to the bubble growth (data not reported).

Parameters related to the mass transport showed great influence over the bubble volume (those retained in Figure 4.3).

Table 4.4: Values of model parameters for the screening study and the associated sensitivity indices of the bubble volume to each model parameter. I_k was determined at day 15.

		Reference	Lowest value	Highest value	Variation (%)	I_k
λ_5 (s)		9324	6428	12230	±31	2.6
α_5		0.04	0.03	0.05	±25	1.7
$D^{ch}_{CO_2}$ ($\cdot 10^{-10}$ m$^2\cdot$s^{-1})		4.5	1.1	6.75	-75 +50	82
r_{CO_2}(mol$\cdot$m$^{-3}\cdot$s^{-1})	stage I	$1.65 \cdot 10^{-6}$	$1.17 \cdot 10^{-6}$	$2.13 \cdot 10^{-6}$	29	110
	stage II	$3.56 \cdot 10^{-5}$	$2.74 \cdot 10^{-5}$	$4.37 \cdot 10^{-5}$	23	
k^{ch}_H (mol$\cdot$m$^{-3}\cdot$Pa^{-1})		$1.23 \cdot 10^{-4}$	$9.23 \cdot 10^{-5}$	$1.54 \cdot 10^{-4}$	±25	0.4
t_{sat} (days)		0	8	12	-[a]	

[a]Sensitivity indice was not calculated for variation of t_{sat}, because different values of t_{sat} meant that simulations were not conducted for the same duration.

Simulated results obtained with $t_{sat} = 12$ days were consistent with the experimental data (Figure 4.3); however they lacked to reproduce the linear trend of bubble growth expected at this stage of ripening. Growth kinetics obtained with $t_{sat} = 8$ days lacked to pass through average values of the experiment. The results considering that saturation is reached at the beginning of the hot room revealed to be inconsistent with the experimental data, when combined with the other reference values (Table 4.4). However, simulated data with $t_{sat} = 0$ were consistent with experimental data when using the lowest value of carbon dioxide diffusivity as detailed below.

The carbon dioxide production rate proved to be slightly more important over the bubble growth than the carbon dioxide diffusivity in cheese (Table 4.4). High sensitivity of bubble growth to carbon dioxide production, combined to the high inter-batches variability of this parameter, argued in favour of measuring it specifically on a cheese block from the same batch, if accurate validation of the model is required.

Simulated bubble volume obtained with the lower value of diffusivity proved to reproduce the average growth kinetics satisfactorily (Figure 4.3). Carbon dioxide diffusivity in cheese was the only parameter that was not specifically determined on the cheese material under study, but was deduced from the diffusivity in pure water (section 4.2). Lower diffusivity than expected can be explained by the fact that all the water is not available for the carbon dioxide to diffuse or that the tortuosity of

the material has been underestimated. Indeed, tortuosity was set at $\pi/2$ under the hypothesis that fat and protein were spherical, but because of the cheese structure complexity, the tortuosity value may be higher. This also encourages further effort for experimental characterisation of carbon dioxide diffusivity in cheese. Let us remind form the introduction section that there is ni such data in the literature.

It is interesting to note that the acceleration of the bubble growth expected beyond the saturation can be postponed by several days because of the low levels of diffusivity, hence calling in question the previously published conclusions about the saturation time (Huc et al. [44]).

At last, the Henry's constant did not present much influence on the bubble growth (Table 4.4), meaning that the first approximation of the carbon dioxide concentration at saturation used in Eq. 4.20 was sufficient.

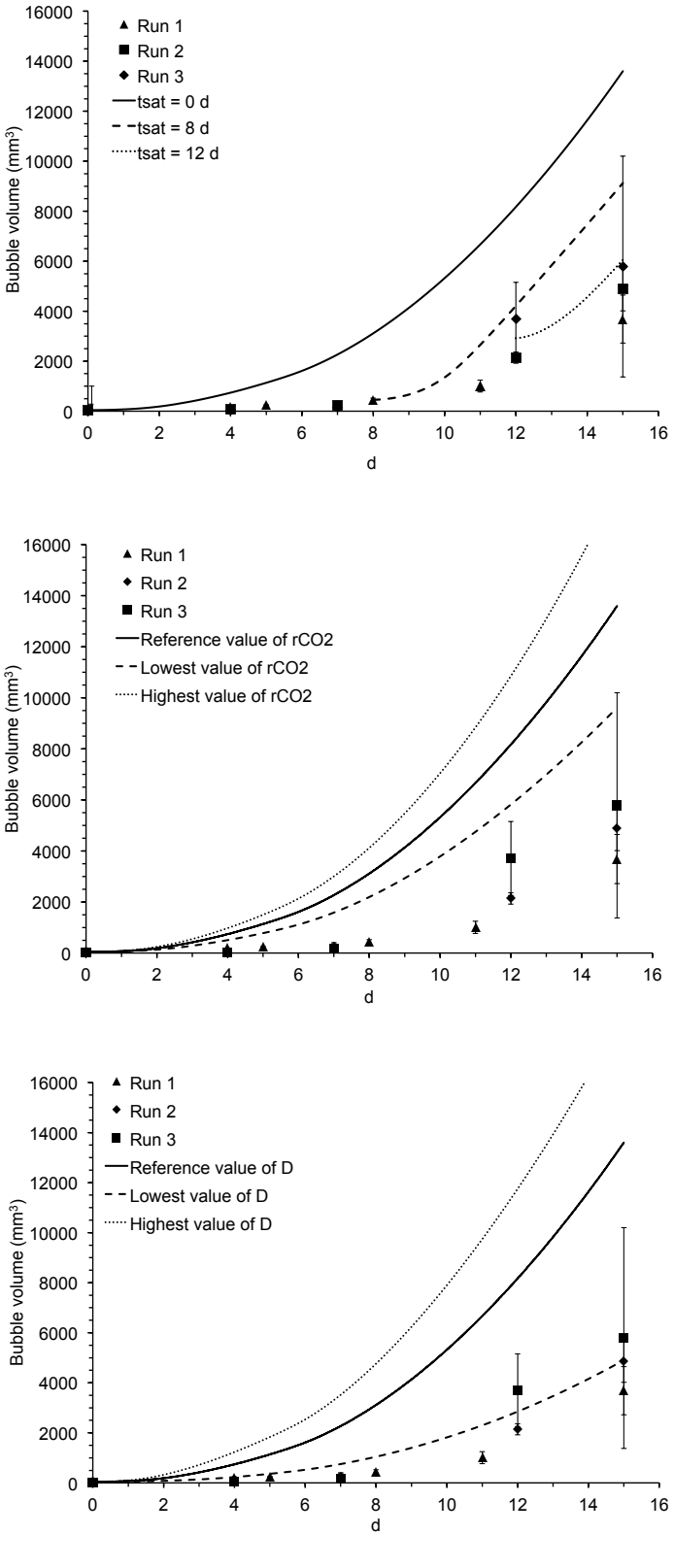

Figure 4.3: Experimental and simulated bubble volumes at the core of the cheese block. Effect of the variations of input parameters of the model all other parameters being set at fixed value: (a) t_{sat}, (b) r_{CO_2}, (c) $D^{ch}_{CO_2}$. Average and standard deviation are calculated over at least 7 bubbles located in the region of interest. Runs are separated by several months and involved a cheese block coming from a different batch.

Considerations about the spatial variability of the model parameters

For this study, two regions of interest (ROI) were considered in the cheese block: at core and under the rind. The two ROI considered experimentally were 3 cm from each other. Assuming diffusivity of the order of 10^{-10} $m^2 \cdot s^{-1}$ yields a characteristic diffusion time between the two ROI of about 100 days, which is significantly higher than the maximal stay in hot room (about 15 days). Therefore, it was considered that the two ROI could be considered independently from each other, from a mass transport point of view.

In order to further validate the model, simulations were conducted for values of input parameters determined under the rind. In particular, $D^{ch}_{CO_2}$ was set at the lower value given in Table 4.4, as it proved to be the value that best fitted the experimental data at core. Production of carbon dioxide was set at its value under rind (Table 4.2). X^w under the rind was set at 0.40, which had an impact on the initial concentration within the domain and on the Henry's constant, that were therefore lower than for the simulations at core. At last, considering the measurements of carbon dioxide concentration made on the same type of semi-hard cheese as the one used in this study (section 4.3.2) and average carbon dioxide production at rind (section 4.1) yielded a saturation that should be reached under the rind at about at 8 days after entering the hot room.

Simulations were therefore conducted with t_{sat} set at 8 days in hot room, which yielded acceptable agreement at the start (until day 12), but for which the final volume was too high. Therefore a second simulation was made with t_{sat} at 12 days. These two simulations permitted to cover the experimental range of results (Figure 4.4). It was assumed for this comparison that diffusion of carbon dioxide was uniform through the cheese block, which may not be the case – it might be lower under the rind. This reinforces the previous conclusion about the need of measurement of this property for this specific food material. In addition, even if such duration does not fit the actual ripening time applied at the industrial scale, further experiments with ripening duration longer than 15 days should be conducted in order to provide more data points for a more complete validation of the model under the rind.

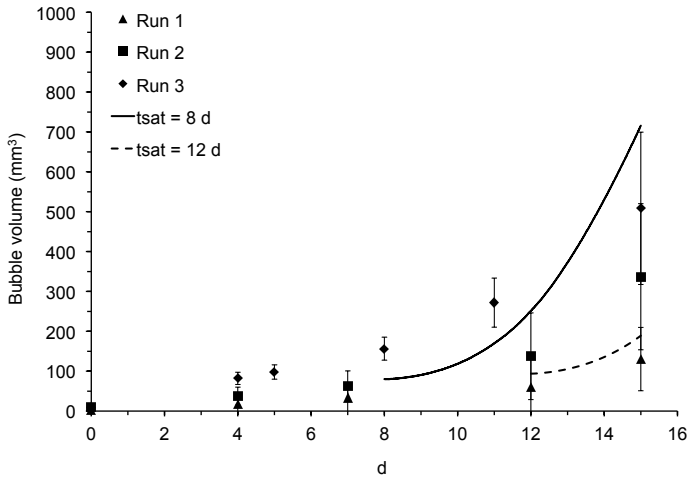

Figure 4.4: Experimental and simulated bubble volumes under the rind. Average and standard deviation are calculated over at least 7 bubbles located in the region of interest. Runs are separated by several months and involved a cheese block coming from a different batch.

6 CONCLUSIONS

The growth of bubbles in cheese was investigated both experimentally and by simulation. Bubble volumes in chees blocks during ripening were assed experimentally with the help of X-Ray imaging and MRI with a dedicated image processing method. Special care was taken on the determination of the model parameters. Mass transport parameters were assessed both from literature data and from dedicated experiments while mechanical parameters were already investigated in a previous study. Growth was considered to occur only when saturation in carbon dioxide was reached under the conditions of the experiment (atmospheric pressure, 293K). A sensitivity study was conducted on the bubble growth model in order to rank the parameters that were the most influential.

Experimental results were compared to simulations, and the model proved to reproduce the bubble growth in cheese in a qualitative manner. The only parameter that was not determined experimentally was adjusted to fit the experimental sets of data with good agreement. Lower diffusivity of carbon dioxide than expected was explained by either an underestimation of tortuosity (initially assumed for spherically-shaped and regularly arranged obstacles) or an overestimation of the space available for diffusion (it was assumed for the first-hand estimation of diffusivity that the whole fraction of water was available for carbon dioxide diffusion).

Experimental bubble growth proved to be highly variable between batches, especially under the rind. Likewise, among the most influential parameters, all involved in the mass balance, production of carbon dioxide also showed to be quite variable between batches, with a standard deviation of about 30%. The latter being most probably the cause of the former. This conclusion argued in favor of high number of repetitions (for instance more than three runs retained for the monitoring of bubble growth) in order to attain a more complete validation of the model.

The sensitivity analysis also showed the predominance of diffusivity on the bubble growth, with an identical level compared to production rate. This conclusion, together with the adjustment of this parameter in the model for the fitting of experimental data, highlighted the need of the measurement of this property in cheese, still lacking in the literature. At last, the mechanical behaviour of cheese proved not to have any effect on bubble growth compared to the mass transport properties.

Chapitre 5

FIRST STEPS TOWARDS A BETTER UNDERSTANDING OF THE GROWTH OF MULTIPLE NEIGHBOURING BUBBLES IN CHEESE

1

INTRODUCTION

The previous chapter on the growth of a single bubble highlighted the most influent factors driving the bubble growth, while validating the ability of this simplistic model to reproduce the average bubble growth within semi-hard cheese blocks. However, it should be emphasised that in cheese blocks, bubbles can rarely be considered to be isolated from each other, and rather present an average of six neighbouring, very close bubbles. In order to move forwards a better understanding of these multiple interactions, a dedicated experiment similar to that used in Chapter 3 and involving two adjacent gaseous cavities was conducted, and was reproduced numerically. This part of the PhD work has necessitated a great amount of implementation, and still requires further work; the results presented below, especially the experimental ones, are preliminary and some tracks of improvement are proposed at the end of the present chapter. For this reason, and although some promising results are already available, the content of this chapter should be considered as pespectives of Chapter 4.

2 MATERIAL AND METHODS

2.1 EXPERIMENTAL SET-UP

The experiment consisted in placing a cheese sample containing a single bubble in an hermetically sealed maintaining apparatus comprising a non-negligible headspace.

The cheese sample consisted of a cylinder comprising a single bubble, and was placed in a maintaining apparatus (Figure 5.2) that ensured constant height of the lateral face of the cylinder throughout the experiment. The headspace height is 23 mm for 30 mm diameter, yielding a volume of 16 258 mm^3, that is two orders of magnitude higher than the typical bubble volume (typical bubble radius ranging from 3 to 5 mm). The headspace was considered as a second gaseous cavity that had a specific volume (surface of the interface divided by the volume of the cavity) lower than the isolated bubble within the sample. The height of the headspace was adjustable at wish, but kept constant in the present study.

The vicinity of the two gaseous cavities aimed at reproducing the real conditions of bubble growth in cheese, either near the crust, where the headspace of the apparatus reproduces the headspace between the cheese and the surrounding foil (Configuration 1 in Figure 5.1) ; either at core between neighboring bubbles, where the headspace of the apparatus acts as a cylindrically shaped bubble with a different specific volume than the actual bubble (Configuration 2 in Figure 5.1).

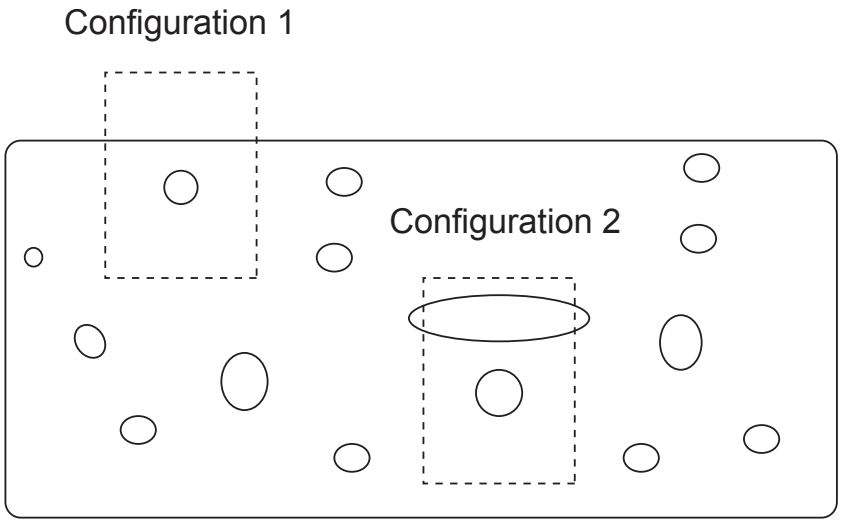

Figure 5.1: Typical situations investigated experimentally

The set-up is considered hermetically sealed for the gazes, using plastic joints that were squeezed while screwing the different pieces of the device. However, tests were made without cheese, and small gas leaks could be observed, at about 0.03% per hour at about 30 kPa.

This maintaining apparatus was placed in a temperature-controlled setup that consisted of an airflow circulating through a double shell surrounding the apparatus drawn in Figure 5.2. Air temperature was regulated in temperature by a cryostat (Julabo FP50, Julabo GmbH, Germany) with a set point temperature at 20 °C, with an actual average at (21 ± 1) °C. This set-up was then placed in an MRI antenna in a MRI scanner for monitoring purpose.

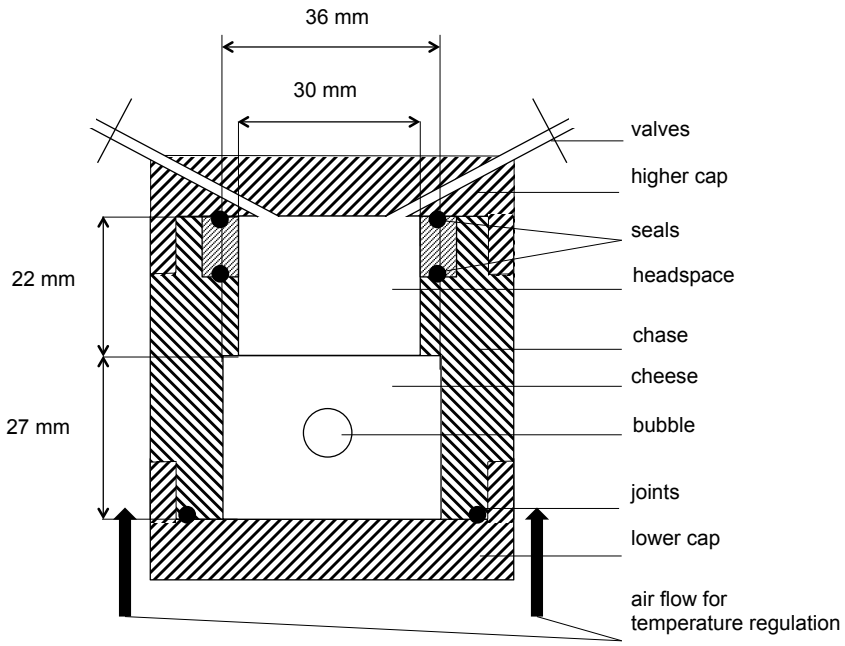

Figure 5.2: Cross-section of the experimental device

2.2 CHEESE SAMPLING

For each experiment, an industrial cheese block was placed in a MRI scanner in order to locate a bubble that was surrounded by plain cheese with diameter matching that of the sustaining apparatus. Once located, the bubble was extracted with a cork borer with an interior diameter of 38 mm. Special care was taken to extract the cylinder as slowly as possible to minimise the unwanted strain in diameter of the extracted cheese cylinder. However, this yielded cheese cylinders that had lower diameters. Right after the extraction, a stretchable plastic film was used on the cylinder to limit desiccation and gas exchange. The extracted cylinder was then placed in a MRI scanner to locate the bubble position within the cylinder, to ensure the bubble could be centred when cutting the edges of the extracted cylinder to the sustaining apparatus dimensions.

Several sustaining apparatus with varying inner diameter were available to make sure interference fit was possible whatever the actual extracted cylinder diameter. The sustaining apparatus with 36.1 mm inner diameter was used for every experiment.

Moisture content was measured on a test sample and on a sample that had been used for an experiment, and it proved that there was a loss of about 1 percentage point between the test sample and the one that was used for the experiment after 6 days. This allowed us to neglect any changes in cheese composition and to neglect the water exchange between cheese and the cavities, as well as their possible impact on the mechanics of cheese

2.3 EXPERIMENTAL PROCEDURE

The experimental conditions are synthesised in Table 5.1 for the three experiments considered. Before headspace gas was flushed with CO_2, a first MRI sequence was launched to measure the exact initial volume and morphology of the bubble as well as its exact initial location within the sample. Hence, there was a non-negligible time between the sampling of the cheese cylinder and the first headspace flushing, during which some carbon dioxide could flow out of the sample. This time is indicated in Table 5.1, and is further discussed in section 2. It was hypothesised that at the beginning of the experiment, concentration of gases other than CO_2 was negligible in the bubble, the reason why this gaseous cavity was not flushed. The pressure in the headspace and the volume of the bubble in cheese were monitored continuously. Multiple flushing of the headspace with CO_2 could be carried out during the experiment (see Table 5.1, and refer to the results section). Conversely to the experiment presented in Chapter 3, the pressure in the bubble was not monitored since leakage of gas were not perfectly controlled, biasing the mass balance which is a key point of this study.

Table 5.1: Summary of the three experiments and of their most significant characteristics

Experiment		1	2	3
Start date		16/05/13	20/06/13	15/10/13
End date		20/05/13	25/06/13	20/10/13
Extent of ripening in hot room before sampling (days)		6	6	5
Duration of the experiment (h)		100	130	120
Time between sampling and launching of the 1st MRI sequence (h)		1.5	1.0	2.0
Initial gas composition	Headspace	CO_2		
	Bubble	assumingly 100% CO_2		
Flushing of headspace during experiment		no	yes	yes
Bubble initial radius (mm)		5.8	4.0	4.7
$H_c - H_b$ (mm)		9.3	10.7	8.0
Cylinder initial height (mm)		19.7	28.2	26.4
Cylinder initial diameter (mm)		36.1	36.1	36.1
Use of glue onto the external surfaces of the sample		no	bottom	bottom and lateral

2.4 MEASUREMENTS

2.4.1 *Pressure and temperature*

Pressure sensors (XCEL-100-25A, Kulite, USA) were connected to the headspace with the help of the valves indicated in Figure 5.2. The pressure sensors were connected to a data logger (Agilent 34970A, Agilent Technologies, USA) and saved with an acquisition frequency of $2{\cdot}10^{-2}$ Hz. The headspace was also monitored in temperature with the help of optic fibres connected to a data logger (FISO UMI 8, Fiso Technologies, Canada) with the same acquisition frequency.

2.4.2 *MRI sequences*

A 3-D Spin-Echo sequence with the following parameters was used to monitor the time-course changes in volume of the bubble:

echo time = 12 ms, repetition time = 400 ms, bandwidth = 295 Hz, 1 scan, pixel size = 0.09 mm², 88 slices, slice thickness 0.7 mm, Signal Noise Ratio = 27, acquisition time 54 min. The whole cylinder was acquired.

This sequence was launched every two hours throughout the experiment.

2.5 IMAGE ANALYSIS FOR INDIRECT ASSESSMENT OF BUBBLE VOLUME

Bubble volume was obtained from MRI image analysis by summing all the bubble voxels after thresholding according to the Otsu method (Otsu 71). With such a method, some voxels of partial volume (partially filled with gas and cheese) were not considered, leading to a systematic underestimation of the volume. The uncertainty on the determination of the bubble volume was a function of the measured volume, and did not exceed 15% of the measured volume.

2.5.1 *Determination of the volume of other cavities*

Image analysis also included the determination of the volume of cavities that were neither the bubble nor the headspace. This allowed the discussion of the importance of such cavities regarding the time-course changes of volume of the bubble under study.

Figure 5.3: Thresholding and labeling of a MRI cross-section image, in the case of extreme detachment of the cheese from the internal surfaces of the sustaining apparatus. Red: headspace and sustaining apparatus (not detected by MRI), blue: cheese, yellow: bubble; green: cavities.

2.6 MODEL OF BUBBLE GROWTH AND CARBON DIOXIDE TRANSPORT

The simulations were conducted using the same modelling developed in Chapter 4 (section 3), except that the geometry, boundary and initial conditions were adapted according to the experimental conditions. The lower and lateral surfaces were still fixed in displacement. Another gas interface was considered at the upper surface to take into account the exchange of carbon dioxide between the upper surface of the cheese sample and the headspace (Eq. 4.4). At the start of the experiment, bubble and headspace were considered to be composed of 100% CO_2 at atmospheric pressure. Similarly to what was done for the bubble- cheese interface, the numerically computed carbon dioxide pressure was applied at the headspace-cheese interface (Eq. 4.11). Figure 5.4 presents the geometry used for the simulations.

A screening study similar to that conducted in Chapter 4 was also conducted within this framework, and Eq. 4.26 was used to calculate sensitivity indices. More input parameters were considered, as the problem was more complex than the problem of mass exchange between cheese and a single bubble. The parameters values are presented in Table 5.2.

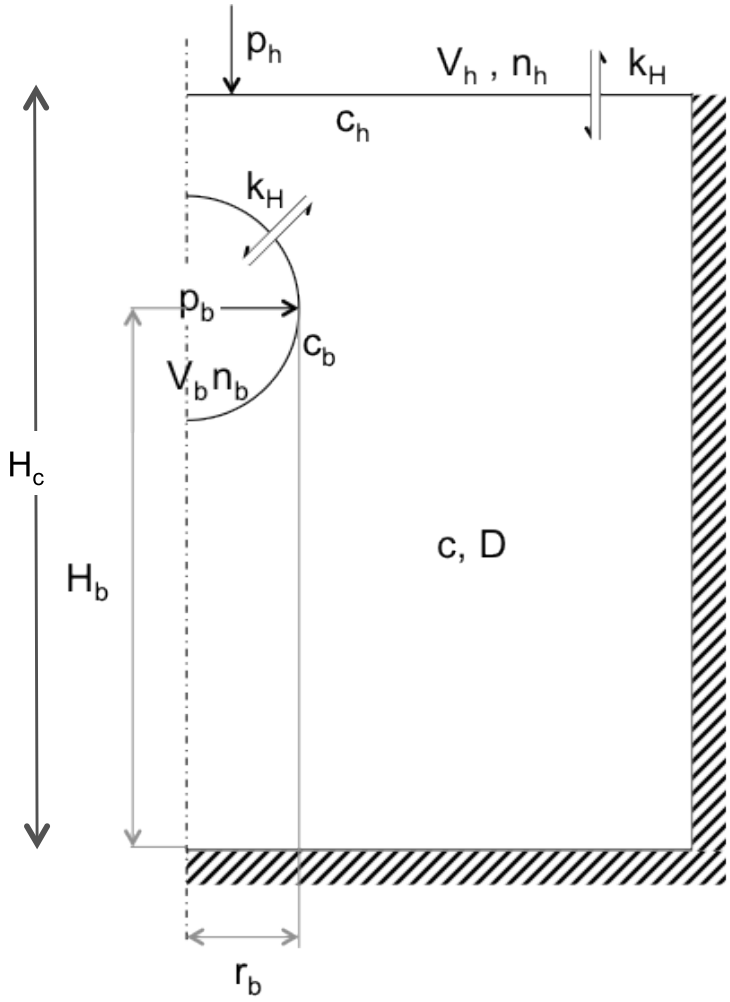

Figure 5.4: Geometry and boundary conditions used for the simulations

3

PRELIMINARY EXPERIMENTAL RESULTS

For each experiment, three types of results are shown. The first show the time-course changes in headspace pressure and bubble volume. They are accompanied by the morphology and cross-section of the bubble as characterised by MRI at different sected times of the experiment. The second is an estimate of the CO_2 partial pressure-equivalent along the axis of the cylinder to facilitate discussion on the results. This partial pressure-equivalent was calculated in the cheese domain as

$$p_{CO_2} = \frac{c}{k_H^{ch}}$$

where c was the apparent carbon dioxide concentration used as the unknown for the simulation and k_H^{ch} the Henry's constant for carbon dioxide in cheese, as evaluated in section 4.3.1 of Chapter 4. For the gaseous cavities, the partial CO_2 pressure was used. The partial pressure-equivalent was estimated relative to the atmospheric pressure in the followings.

3.1 EXPERIMENT 1

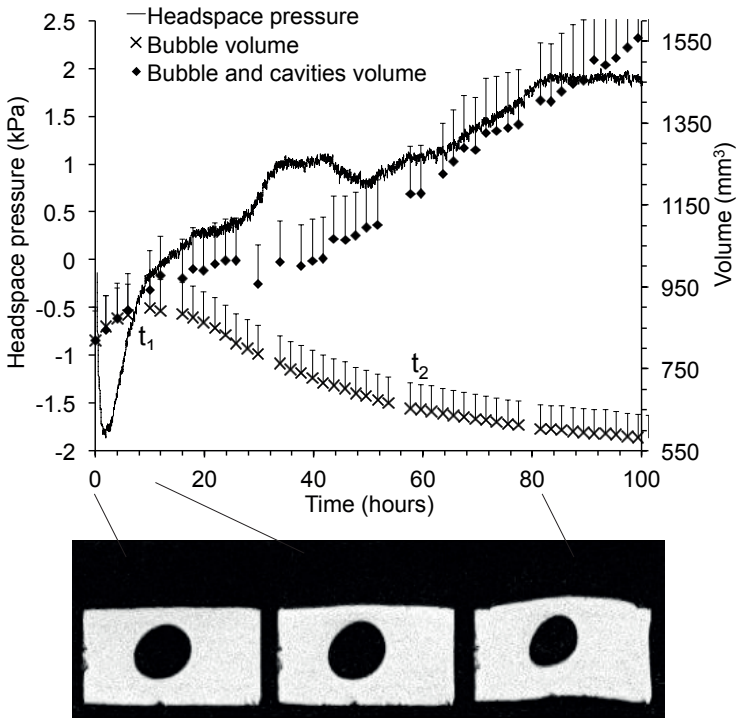

Figure 5.5: Time-course changes in bubble volume and headspace pressure during Experiment 1, with a selection of MRI cross-section s at times $t = 0$, 10 and 85 h

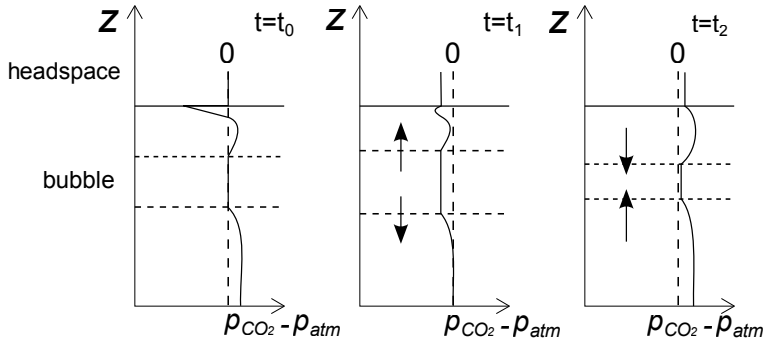

Figure 5.6: Vertical profiles of CO_2 partial pressure-equivalent deduced from the time-course changes in the bubble volume and the pressure in the headspace during Experiment 1. The vertical profile is placed at the centre of the cylinder.

At the beginning of experiment (until 2.5 h), the decrease of the headspace pressure can be explained by the fact that between the extraction and the start of the experiment, CO_2 moved from the cheese to the atmosphere. When at $t = 0$, the headspace is filled with CO_2 at atmospheric pressure, the CO_2 migrates from the headspace to the cheese, to compensate the loss that occurred just before the beginning of the experiment. Part of the increase of the bubble volume during this period can be explained by the negative pressure of the headspace, but there was also a migration of CO_2 from the cheese to the bubble.

The continued decrease of the bubble volume in the same time as an increase of the headspace pressure was caused by the growth of cavities under and on the side of the sample (Figure 5.5). However, if taking into account the overall volume of cavities, the increase can be explained by the production of CO_2 within the cheese, and is confirmed by the simultaneous headspace pressure increase.

Since interpretations were complicated by the presence of more than two cavities, the application of glue onto the lower surface was envisaged to prevent the creation of these cavities.

3.2 EXPERIMENT 2

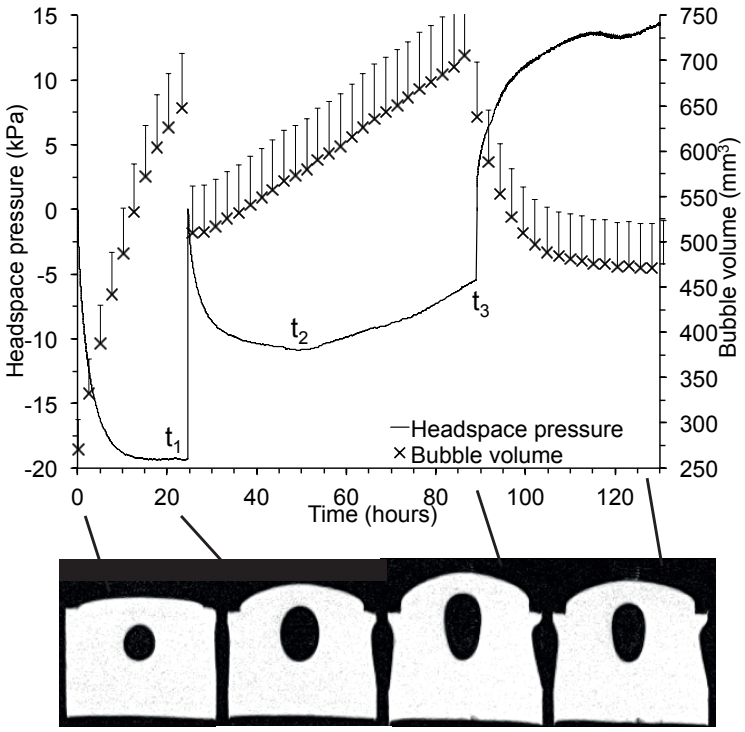

Figure 5.7: Time-course changes in bubble volume and headspace pressure during Experiment 2, with a selection of MRI cross-section s at times $t = 0$, 20, 90, and 130 h

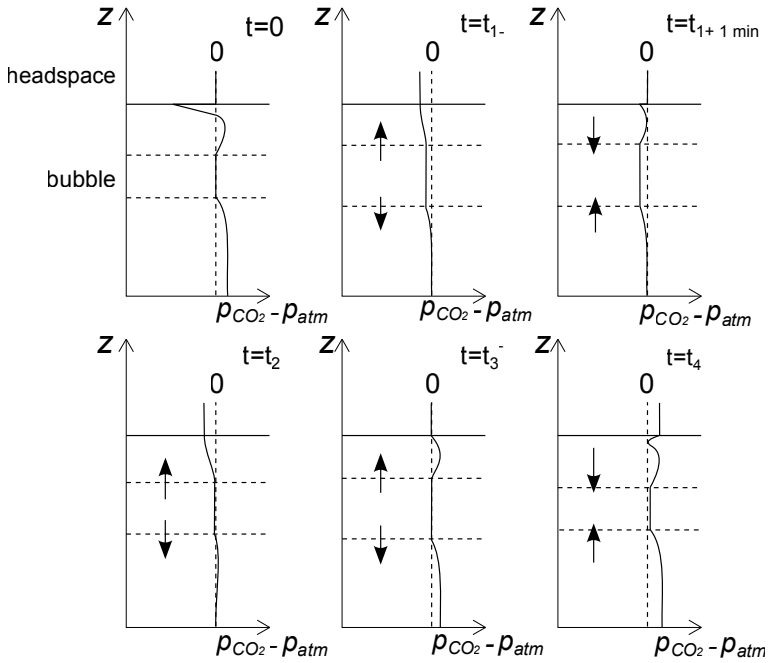

Figure 5.8: Vertical profiles of CO_2 partial pressure-equivalent deduced from the time-course changes in the bubble volume and the pressure in the headspace during Experiment 2. The vertical profile is placed at the centre of the cylinder.

The beginning of Experiment 2 was very similar to that of Experiment 1, except that the decrease of headspace pressure was 10 times higher than for Experiment 1 (Figure 5.7). The bubble volume increase observed can be explained by the vacuum pressure applied at the upside surface, that was applied for a long time (25 h) due to CO_2 migration towards the cheese. When the headspace was flushed again with CO_2 at $t = 25$ h and pressure was set back to the atmospheric value, an almost instantaneous decrease of bubble volume was observed. The bubble volume was nevertheless higher than the initial volume, due to both permanent strain caused by the vacuum pressure and CO_2 migration from the cheese in the bubble during the preceding period.

During the second period between $t = 25$ h and$t = 90$ h, a transient regime can be observed for the headspace pressure until t_2 ($t = 50$ h), where the pressure started to increase. This can be explained by the fact that, until t_2, there is a concentration gradient between the headspace and the bubble that causes the CO_2 from the headspace to migrate towards the cheese (Figure 5.8). After t_2, the increase of both headspace pressure and bubble volume is due to the CO_2 production within the cheese and its transport towards either headspace or bubble. The other cavities created by the large vacuum pressure (Figure 5.9) presented time-course changes that were similar to those of the bubble, indicating that, contrary to Experiment 1, the presence of cavities did not disadvantage the growth of the bubble in favour of these cavities.

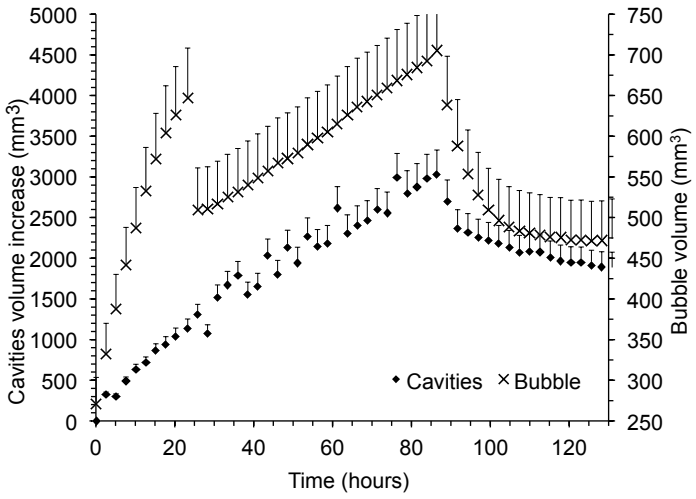

Figure 5.9: Bubble and cavities volumes for Experiment 2

3.3 EXPERIMENT 3

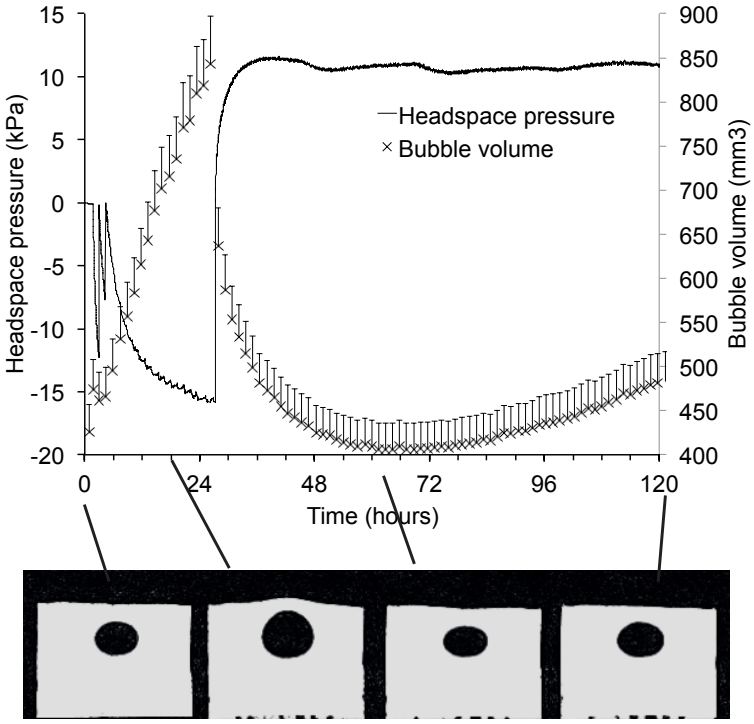

Figure 5.10: Time-course changes in bubble volume and headspace pressure during Experiment 3, with a selection of MRI cross-sections at times $t = 0$, 20, 60 and 120 h

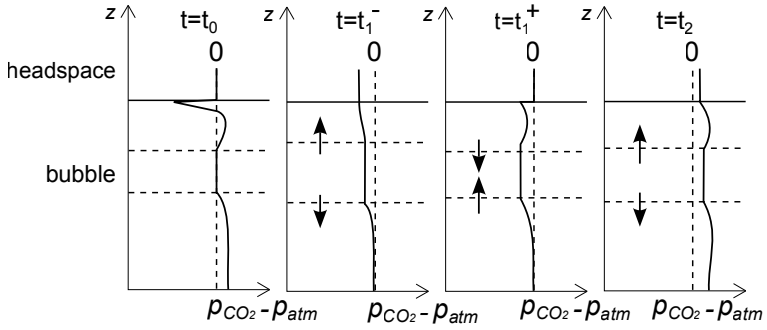

Figure 5.11: Vertical profiles of CO_2 partial pressure-equivalent deduced from the time-course changes in the bubble volume and the pressure in the headspace during Experiment 3. The vertical profile is placed at the centre of the cylinder.

At the beginning of Experiment 3, the headspace was flushed several times (Figure 5.10) to prevent the prolonged high levels of stress that were observed on Experiment 2 (Figure 5.7) and that caused important unwanted strain. Moreover, contact between cheese cylinder and the sustaining apparatus was maintained with glue that was applied on the lower and lateral surfaces. The glue can be observed at the bottom of the MRI images (Figure 5.10). The increase in bubble volume observed from 0 to 24 h can be explained by the negative relative headspace pressure, caused by the migration of CO_2 from the headspace towards the cheese cylinder. At $t = 24$ h, head space was flushed with CO_2 at atmospheric pressure. Part of the decrease in bubble volume from 24 h to 60 h can be explained by the fact that the relative headspace pressure was no longer negative. Again, headspace pressure equilibrium was considered to happen at t_2, where the bubble starts to grow again.

Cavities volume proved not to vary much compared to bubble volume (Figure 5.12). This confirmed the advantage of gluing both the lateral and lower surfaces of the sample.

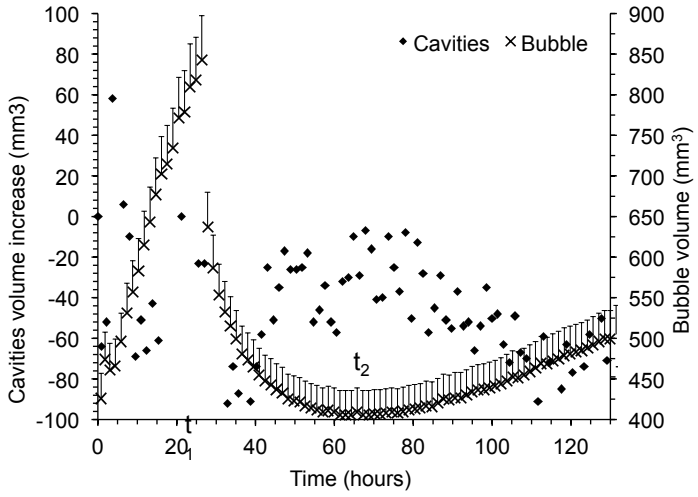

Figure 5.12: Bubble and cavities volume for experiment 3

3.4 GENERAL DISCUSSION OF THE EXPERIMENTAL RESULTS

Firstly, it should be emphasised that dealing with foodstuff brings a lot of product-related constraints, among them the evolving nature of the product was the most hindering and required particular attention, for instance in maintaining the temperature stable and close to that of the actual ripening or the nonaerobic conditions to prevent unwanted microbiological activity. Besides, the dimensions of the set-up made the instrumentation difficult, necessitating to deal with significant measurement uncertainties (see Chapter 2).

After a long period of implementation (six runs additional to the three presented above), the feasibility of mastering such type of experiment was demonstrated. Quite similar trends observed during Experiments 2 and 3 provided evidence of possible reproducibility, a point which was highly questioned during the stage of implementation of the experimental procedure. The most notable similarities were the fact that the sample absorbed a great amount of carbon dioxide, causing negative relative pressure in the headspace as high as 30 kPa (to be compared to the average bubble pressure within cheese that is ten times lower), and the fact that bubble growth was monitored only after headspace pressure equilibrium was reached. This behaviour would tend to suggest that carbon dioxide saturation was not reached everywhere in the cheese cylinder at the beginning of the experiment. However, this is in contradiction with the size of the bubble contained within the samples, that indicated bubble growth occurring in saturation regime. This contradictory effect is still not fully explained. Transfer from the cut surfaces of the cheese cylinder during the waiting time is the most plausible explanation; nevertheless the amount of carbon dioxide estimated from the lowering in pressure in the headspace was two-fold that estimated from the diffusion of carbon dioxide (using analytical solution).

The headspace pressure equilibrium time was observed late in the experiment, indicating that the experiment should have been much prolonged. Indeed, bubble growth concomitant to an increase in pressure in the headspace was only noticeable at the end of the experiment (2 and 3), and not enough data was available for model validation. The developped experimental procedure is not totally questioned, but requires some adaptation, as detailed below.

The first way will be to minimize the time elapsed between the sampling of the cheese cylinder and the launching of the experiment ($t = 0$). Note here that in the previous experimental procedure, most of the time elapsed between the sampling of the cheese cylinder and the initial flush of the headspace was due to the acquisition of a first, highly resolved image of the cheese cylinder and its bubble. This could be much reduced.

If despite of these precautions, the lowering in pressure is still observed in the headspace over a long time, the headspace will be flushed with carbon dioxide, as regularly as necessary to prevent unwanted stress due to a negative relative pressure in headspace. However, contrary to the previous experimental procedure, only the headspace pressure would need monitoring.

Optimal monitoring conditions will be considered to be reached when the headspace pressure starts increasing again. MRI monitoring should only begin at that moment.

The rest of the experiment could be conducted following the procedure already established, over the same duration as initially envisaged, *i.e.* comprised between 5 and 7 days.

At last, the apparition of unwanted cavities between the lower and lateral surfaces and the maintaining apparatus, could be avoided or limited in a large extent by the use of glue on these lower and lateral surfaces.

At the moment, the numerical model developed is unable to produce results consistent with the observed experiments. This discrepancy between simulated and experimental behaviours can be explained by the fact that the headspace equilibrium stage was not convered by the model, that hypothesed saturation regime.

4

SIMULATION RESULTS

Although a high number of simulations, in various conditions was conducted, only the results for the reference parameters configuration are shown : concentration map of the domain (Figure 5.13), time-course changes in bubble and headspace pressure and volume (Figure 5.14), equivalent partial pressure relative to atmospheric pressure along the axis of symmetry (Figure 5.15), and the carbon dioxide streamlines (Figure 5.16). The ranking of the parameters with respect to bubble volume are also presented.

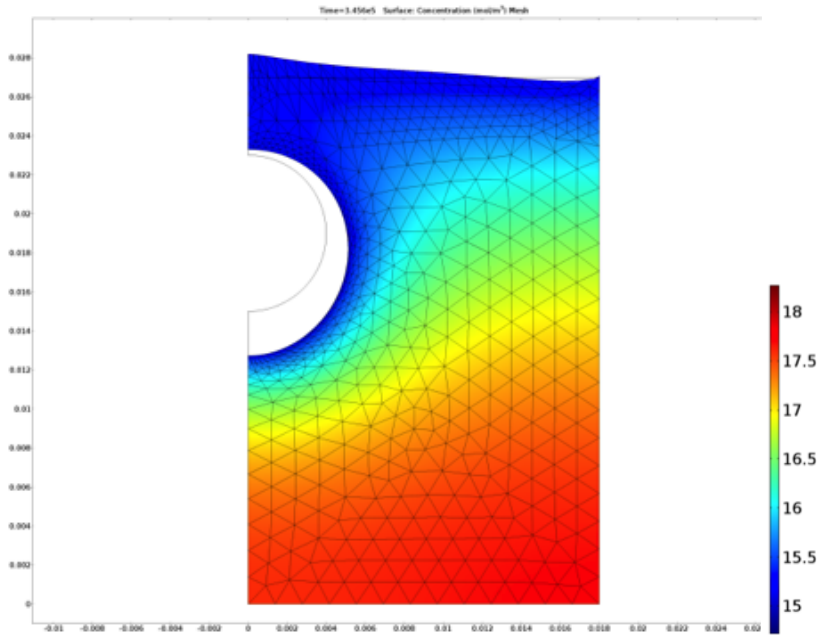

Figure 5.13: Concentration in the domain and deformed shape at the end of simulation (t = 96h).

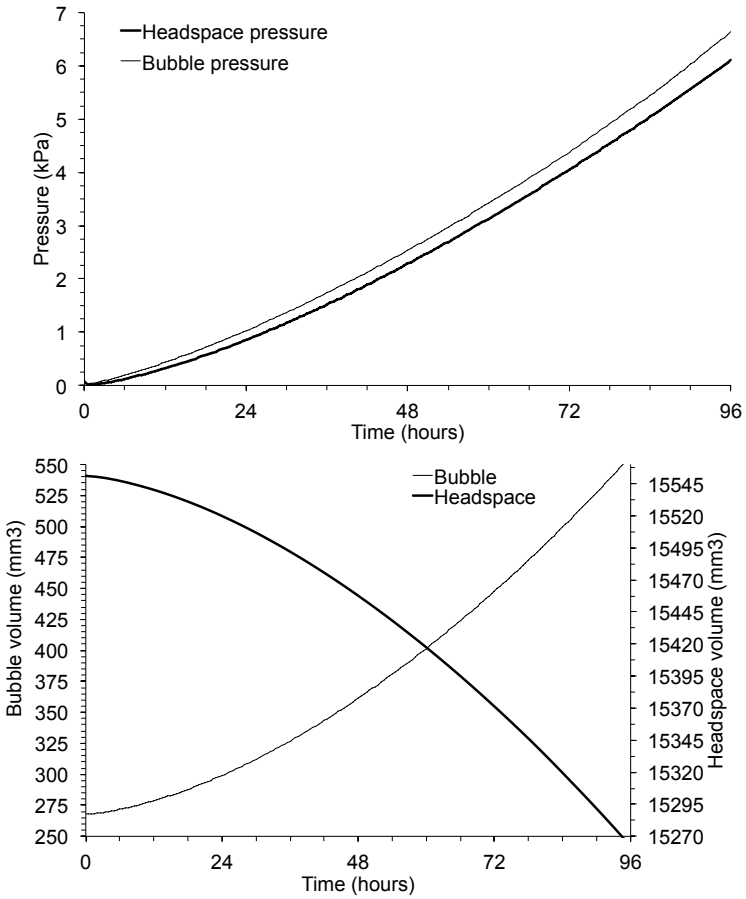

Figure 5.14: Bubble and headspace volume (left) and pressure (right) for reference parameters

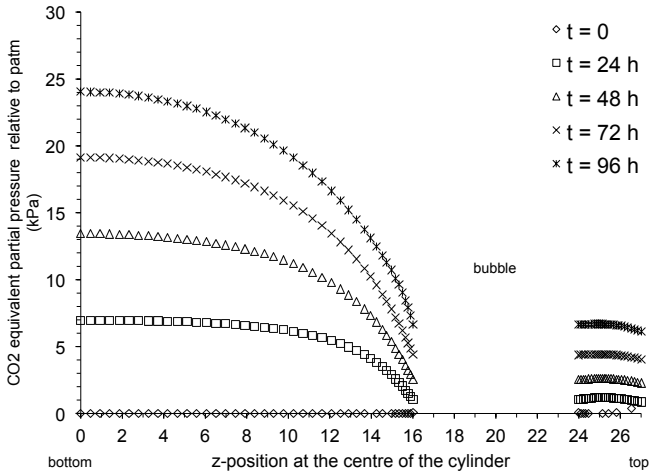

Figure 5.15: CO_2 partial pressure equivalent, relative to atmospheric pressure, at several simulation steps.

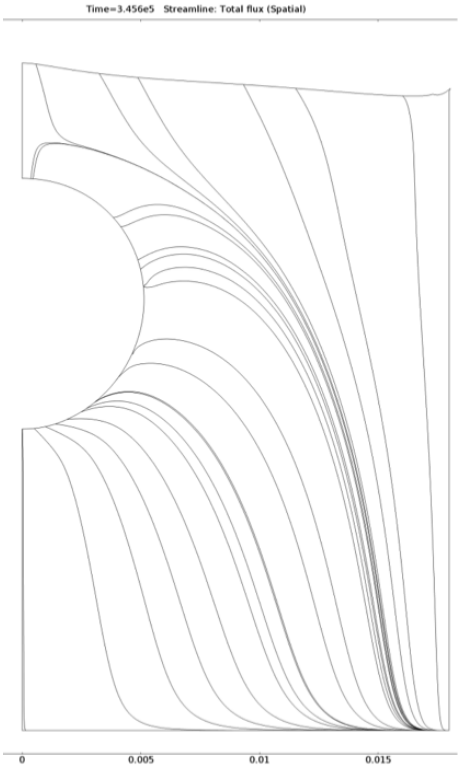

Figure 5.16: Carbon dioxide concentration streamlines for reference set of parameters.

Due to a bubble pressure higher than the headspace pressure, an increase of the bubble volume and a decrease of the headspace volume could be observed (Figure 5.14). The original idea was to compare these trends with the experimental trends originating fron the experimental procedure presented in the previous section.

Due to combined CO_2 production, low carbon dioxide diffusivity, and null mass flow at the lateral and bottom surfaces of the cheese cylinder, CO_2 concentration kept increasing in the domain (Figure 5.15). It was conversely smaller near the interfaces with gaseous cavitites, due to the outward CO_2 flux caused by the change in pressure. Simulations suggested that oversaturation in the cheese domain can reach levels as high as 25% more than the saturation level and less than 10% in cheese wall separating close gaseous cavities. This result would need experimental confirmation by assessing the carbon dioxide concentration in the cheese cylinder to which the experimental procedure presented in the previous section would be applied.

Compared to the screening study conducted in Chapter 4, the screening study in a configuration with a closed headspace in exchange with the cheese material highlighted the importance of geometry parameters such as the initial bubble radius or the initial distance between the headspace and the bubble (Table 5.2). When normalising the time-course changes in bubble volume by the initial bubble volume, smaller bubbles increased proportionally much than larger bubbles, emphasising the role of the specific volume ratio for bubble growth (smaller bubbles have the largest surface to volume ratio). Bubbles nearer to the headspace-cheese interface proved to have final volumes that were lower. This is explained by the fact that the lowest the location of the bubble in the cheese cylinder, the more it benefited from the carbon dioxide produced in the cheese, whereas near the headspace-cheese interface, carbon dioxide moves both towards the headspace and the bubble, as suggested by the streamlines in Figure 5.16.

The ranking of the other parameters (parameters related to mass and momentum transport) did not change compared to the results of Chapter 4. Sensitivity results from the previous chapter are reported for this purpose. In particular, the momentum transport parameters had no influence over the bubble growth compared to the mass transport. Note that the presence of the headspace tended to lessen the sensitivity indices for the diffusivity and the production rate of carbon dioxide, that are 2 to 4 times lower in this study than in the screening study of Chapter 4. For the moment, this comparison should remain qualitative, seeing that the variation that was applied for these parameters differed in the present study, and that when calculating the sensitivity indices, it was considered in a first approach that the influence of the variation of input parameters was linear over the outputs, which is a strong hypothesis. Note that this last hypothesis could be removed by using statistical methods like the one exposed in Chapter 3.

Table 5.2: Values used in the screening study for each entry parameter of the model and impact of these variations on the variation of the bubble volume after 72 h, multiple bubbles model

Parameter	Reference	Lowest value	Highest value	Variation (%)	I_k
λ_5(s)	9324	6428	12230	31	1.3
α_5	0.04	0.03	0.05	25	3.0
$D^{ch}_{CO_2}(\cdot 10^{-10}\ m^2 \cdot s^{-2})$	5.0	2.5	7.9	54	24
$r_{CO_2}(\cdot 10^{-5} mol \cdot m^{-3} \cdot s^{-1})$	1.15	0.58	1.44	37	50
$k^{ch}_H(\cdot 10^{-4} mol \cdot m^{-3} \cdot Pa^{-1})$	1.41	1.06	2.28	43	8.9
$H_c - H_b$ (mm)	8.0	10	6.0	25	24
r_b(mm)	4	3	5	25	85

Table 5.3: Values of model parameters for the screening study and the associated sensitivity indices of the bubble volume to each model parameter. I_k was determined at day 15.

		Reference	Lowest value	Highest value	Variation (%)	I_k
λ_5 (s)		9324	6428	12230	$\pm$31	2.6
α_5		0.04	0.03	0.05	$\pm$25	1.7
$D^{ch}_{CO_2}$ $(\cdot 10^{-10}\ m^2 \cdot s^{-1})$		4.5	1.1	6.75	-75 +50	82
$r_{CO_2}(mol \cdot m^{-3} \cdot s^{-1})$	stage I	$1.65 \cdot 10^{-6}$	$1.17 \cdot 10^{-6}$	$2.13 \cdot 10^{-6}$	29	110
	stage II	$3.56 \cdot 10^{-5}$	$2.74 \cdot 10^{-5}$	$4.37 \cdot 10^{-5}$	23	
k^{ch}_H $(mol \cdot m^{-3} \cdot Pa^{-1})$		$1.23 \cdot 10^{-4}$	$9.23 \cdot 10^{-5}$	$1.54 \cdot 10^{-4}$	$\pm$25	0.4
t_{sat} (days)		0	8	12	-[a]	

[a]Sensitivity indice was not calculated for variation of t_{sat}, because different values of t_{sat} meant that simulations were not conducted for the same duration.

5 CONCLUSIONS

In order to validate the model and its set of values for entry parameters, future investigation will focus on repeated experiments accordingly to the improved experimental procedure detailed in section 3.4.

Experiments conducted so far allowed to demonstrate the feasibility of experimental validation at the bubble scale with a dedicated experiment, with control over initial and boundary conditions for mass and momentum transport.

The sensitivity study that was conducted underlined the importance of geometrical parameters in the case of multiple neighbouring bubbles growth. In particular, distance between the two cavities and the cavities sizes proved to be as important as the diffusive parameters related to the mass balance, previously identified as the driving parameters in Chapter 4.

CONCLUSIONS ET PERSPECTIVES

Au terme des trois axes de travail développés au cours de cette thèse, plusieurs enseignements ont pu être tirés à la fois sur la croissance de bulles dans les fromages à pâte pressée non-cuite mais aussi sur les propriétés mécaniques et de transport du matériau étudié.

Tout d'abord, la caractérisation mécanique du produit a permis de découvrir que, contrairement à ce qui est plus ou moins accepté par les technologues et ce qui était envisagé au début du projet, les propriétés rhéologiques du fromage étudié ne varient pas au cours de l'affinage, ou que tout du moins la grande variabilité entre batches et la précision à la fois de la mesure et de la méthode de détermination de paramètres rendent impossible l'estimation d'une telle évolution. La seule variation observée serait liée à un effet de la température, au cours du passage entre la cave froide et la cave chaude, qui peut diminuer la rigidité du produit à mesure que la température augmente. L'étape de caractérisation mécanique du produit a permis de dégager certains biais expérimentaux, qui bien qu'ils soient connus, sont souvent négligés, et de proposer des suggestions d'améliorations. En particulier, deux biais sont importants, car ils dépassent le cadre de tests de compression-relaxation. En premier lieu, une partie des contraintes relaxe pendant la compression du produit. Cela signifie que, même pour la caractérisation élastique de produits de ce type, une attention particulière doit être portée sur les conditions de sollicitations de celui-ci. En second lieu, citons l'aspect des échantillons, pour lesquels la découpe s'est révélée avoir une forte influence sur la détermination de paramètres. En effet, les échantillons affichant une taille de quelques millimètres, les méthodes de découpe et la nature du matériau font qu'il est difficile d'assurer le parallélisme des faces de l'échantillon. Ce défaut de parallélisme peut causer par la suite des biais de mesure importants selon la méthode de détermination utilisée. Il a été montré dans ce travail de thèse que ce biais peut atteindre 25% avec les méthodes usuelles de régression linéaire.

La méthode de détermination des paramètres viscoélastiques proposée dans le cadre de cette thèse n'est pas limitée au fromage, mais pourrait s'envisager sur d'autres matériaux possédant un large spectre de temps de relaxation, s'étalant de la milliseconde à plusieurs heures. De plus, la méthode proposée s'est avérée moins sensible aux biais expérimentaux étudiés que les méthodes usuelles de détermination de paramètres.

La validation expérimentale du modèle de Maxwell a été menée en conditions de sollicitations mécaniques uniquement. Cela a consisté à imposer une pression à l'intérieur d'une bulle dans un dispositif expérimental de suivi, sur des durées de l'ordre de quelques heures, permettant de raisonnablement négliger les effets de la diffusion de matière au sein du matériau. Cette validation a permis d'affirmer la pertinence de ce modèle, qui, bien que restant simple, propose un accord tant qualitatif que quantitatif pour la reproduction du comportement mécanique des fromages à pâte pressée autour d'une bulle. Cette validation met aussi en avant la bonne adéquation du test rhéologique choisi vis-à-vis des sollicitations à long-terme que subit le fromage lors de la croissance de bulles. En outre, en conditions de sollicitations proches des condi-

tions réelles, il a pu être démontré que les biais de détermination des paramètres à long-terme rencontrés lors de la première étape (bruit sur les données expérimentales, évolution du produit sur la durée de l'expérimentation) ne sont pas un frein à la caractérisation du produit, au regard des différentes incertitudes caractérisées. Si le modèle de Maxwell généralisé n'est pas exempt de défauts, étant limité pour les sollicitations brèves au domaine élastique, il faut souligner le fait que des modèles plus complexes impliquent une caractérisation du matériau qui ne l'est pas moins. En outre, cette caractérisation peut s'avérer délicate sur des produits agroalimentaires, qui peuvent être évolutifs dans le temps : séchage du produit, influence de la composition de l'atmosphère l'environnant sur ses transformations internes et présentent une grande variabilité d'un échantillon à l'autre. Au regard de ces incertitudes, et dans l'état de maîtrise des procédés expérimentaux de détermination de paramètres, il est tout à fait probable qu'un éventuel gain apporté par un modèle rhéologique plus complexe soit entravé par une variabilité (intra produit, intra-batch voire inter-batch) qui peut être très importante.

Le bon accord obtenu entre simulation et expérience découle de deux aspects principaux :

- la grande viscosité du produit sur les échelles de temps considérées, qui permet de ne pas outrepasser la limite élastique lors des sollicitations ;
- le soin apporté à la détermination de paramètres du modèle sur le matériau étudié.

Cette première étape de validation du modèle en conditions de sollicitations mécaniques uniquement a aussi permis de dégager les paramètres mécaniques les plus influents sans subir l'influence du transport de matière, à savoir les paramètres à long-terme que sont le module de cisaillement et le temps de relaxation de la dernière branche du modèle de Maxwell, de l'ordre 5% du module de cisaillement total et 3 heures pour le temps de relaxation.

L'inclusion du transport de matière dans le modèle de croissance de bulle a permis de montrer la faible influence des paramètres mécaniques sur la croissance de bulle. Ce résultat s'articule de manière cohérente avec le fait que la croissance des bulles dans les blocs de fromage est très significative en cave chaude, alors que les propriétés rhéologiques varient peu dans le même temps. Le modèle développé permet de reproduire un comportement moyen de bulle dans un fromage à pâte pressée non-cuite, et souligne l'importance à cet égard des paramètres liés au transport de matière, en particulier le taux de production de dioxyde de carbone et le coefficient de diffusion du dioxyde de carbone dans le fromage. Le premier a fait l'objet de mesures sur le fromage étudié et l'incertitude inter-batch associée a pu être caractérisée, alors que c'est sur le second que les efforts d'ajustement se sont portés. Les résultats du chapitre

4 montrent qu'une estimation à partir des valeurs de diffusion du dioxyde de carbone dans l'eau, pondérées par la teneur en eau et par la tortuosité du matériau donne au mieux un ordre de grandeur, mais ne suffit pas à assurer l'accord des simulations avec les observations expérimentales. Ce constat engage à une détermination expérimentale de ce paramètre pour se rapprocher le plus possible des conditions réelles.

La prédominance du transport de matière met aussi en avant le fait que ce sont avec les leviers pilotant le transport de matière que le technologue pourra opérer des modifications sur le produit. À cet égard, le levier le plus visible reste l'activité fermentaire qui, pour les souches bactériennes envisagées, est une caractéristique de l'affinage en cave chaude. Seulement, cette activité fermentaire n'a pas une influence uniquement sur la teneur en dioxyde de carbone (qui peut être vue comme un coproduit de la fermentation et non comme son objet principal), mais aussi sur d'autres caractéristiques organoleptiques, tel l'aspect aromatique, qui ont, pour l'instant, été négligées.

En outre, la modélisation effectuée n'a envisagé que partiellement le cas de plusieurs bulles interagissant entre elles. Les résultats préliminaires portant sur l'interaction entre deux cavités gazeuses montrent bien que cela perturbe la hiérarchisation des phénomènes de transport établie dans le cas d'une bulle isolée et introduit de nouveaux paramètres qui peuvent piloter la croissance de bulles, essentiellement géométriques cette fois-ci. Ainsi, la taille des cavités gazeuses et la distance les séparant jouent-elles un rôle aussi important que le taux de production de dioxyde de carbone ou de diffusion de celui-ci.

Un autre aspect, qui révèle son importance dans la conduite du procédé de fabrication, est la prise en compte des variations de température. En effet, le projet U2M-ChOp s'est focalisé sur des processus monothermes, à savoir l'affinage en cave chaude. Cependant, la variabilité dans le maintien de la température lors du procédé d'affinage suggère que tous les fromages ne sont pas affinés à la même température, et que cela pourrait expliquer la variabilité observée entre échantillons : tous les phénomènes impliqués dans la croissance de bulles sont sensibles à la température (propriétés mécaniques, activité fermentaire, diffusion). De plus, l'exploration de l'aspect thermique apparaît intéressant dans une optique de réduction des coûts énergétiques de production.

ANNEXES

A

FABRICATION D'UN FROMAGE À PÂTE PRESSÉE NON-CUITE

A.1 DÉFINITION

Le codex STAN 283-1978 définit le fromage comme suit.

Le fromage est le produit affiné ou non affiné, de consistance molle ou semi-dure, dure ou extra-dure qui peut être enrobé et dans lequel le rapport protéines de lactosérum/caséine ne dépasse pas celui du lait, et qui est obtenu :

A. par coagulation complète ou partielle des protéines du lait, du lait écrémé, du lait partiellement écrémé, de la crème, de la crème de lactosérum ou du babeurre, seuls ou en combinaison, grâce à l'action de la présure ou d'autres agents coagulants appropriés et par égouttage partiel du lactosérum résultant de cette coagulation, tout en respectant le principe selon lequel la fabrication du fromage entraîne la concentration des protéines du lait (notamment de la caséine), la teneur en protéines du fromage étant par conséquent nettement plus élevée que la teneur en protéines du mélange des matières premières ci-dessus qui a servi à la fabrication du fromage et/ou

B. par l'emploi de techniques de fabrication entraînant la coagulation des protéines du lait ou des produits provenant du lait, de façon à obtenir un produit fini ayant des caractéristiques physiques, chimiques et organoleptiques similaires à celles du produit défini à l'alinéa (A).

Comme indiqué en introduction du présent mémoire, il n'existe pas de codex général pour les fromages à pâte pressée, mais des standards spécifiques à certaines variétés (emmental, gouda, cheddar, etc.), qui définissent les conditions d'appellations des dits fromages en fonction de propriétés du lait utilisé pour la fabrication, des conditions de fabrication et de la composition du produit fini.

Il existe deux types de fromages à pâte pressée : ceux pour lesquels la pâte est cuite (comme l'emmental ou le comté) et ceux pour lesquels la pâte n'est pas cuite (comme le maasdam ou le laguiole).

A.2 ÉTAPES DE FABRICATION

A.2.1 *Préparation du lait*

Avant la fabrication proprement dite du fromage, le lait utilisé est préparé. Il subit plusieurs traitements.

1. Standardisation en matière grasse : permet d'ajuster le rapport gras sur sec du produit fini.
2. Pasteurisation : étape d'assainissement du lait.
3. Ensemencement : ajout de ferments lactiques et propioniques.

A.2.2 *Fabrication du fromage*

Une fois le lait préparé, on peut passer à la fabrication proprement dite du fromage.

1. Emprésurage : on ajoute de la présure, qui a pour effet de former un gel, le caillé.
2. Tranchage : opération de découpage du caillé en grains, qui vont favoriser l'égouttage du caillé (c.-à-d. l'expulsion du sérum).
3. Égouttage : cette opération comporte plusieurs étapes toutes visant à favoriser l'expulsion du sérum des grains de caillé, et à préparer la suite. On va ainsi :
   a) brasser le mélange sérum-caillé afin que les grains de caillé soient mobiles et que leurs surfaces d'échange restent libres ;
   b) réduire la concentration en lactose du sérum (délactosage).
4. Moulage : cette première étape de mise en forme du fromage dans des moules vise à séparer le sérum des grains de caillé et donne sa forme au fromage.
5. Pressage : cette étape consiste à appliquer une pression sur les grains de caillé présents dans le moule afin de donner sa forme définitive au fromage et de compléter l'égouttage.
6. Saumurage : le fromage est plongé dans un bain de saumure (solution saturée en sel), qui permet de compléter l'égouttage, d'amorcer le développement organoleptique du produit et de travailler la surface (durcissement de la croûte, assainissement de la surface).

A.2.3 *Affinage*

Une fois le fromage fabriqué intervient l'étape d'affinage. Elle est essentielle car c'est l'étape qui voit le développement des qualités organoleptiques du produit. La pâte subit différentes transformations (par exemple par protéolyse ou lipolyse) qui assurent sa maturation. De plus, dans le cas des fromages étudiés dans le cadre de cette thèse, l'affinage est aussi le siège du développement d'ouvertures (ou bulles ou *yeux*). Suivant les recettes de fromages, l'affinage peut avoir lieu à différentes températures au cours du temps, et se dérouler sur des périodes de temps très variables (de quelques semaines à plusieurs années suivant le type de fromage).

B

PRINCIPES D'IMAGERIE PAR RÉSONANCE MAGNÉTIQUE (IRM)

Cette annexe ne vise pas à donner un exposé exhaustif de l'IRM, mais propose d'en donner les principes, ainsi que de placer l'imagerie dans un contexte de recherche agroalimentaire qui est le cadre de la présente thèse.

B.1 RÉSONANCE MAGNÉTIQUE NUCLÉAIRE (RMN)

Comme son nom le laisse suggérer, l'IRM se base sur le phénomène de résonance magnétique. Il existe différents types de résonance magnétique, mais on n'évoquera ici que de la RMN ^{1}H. Comme l'hydrogène ne possède qu'un proton, on parle indifféremment d'hydrogène, ou de proton (voire même, par abus de langage, de spin). La RMN ^{1}H s'applique facilement au domaine du vivant, en raison de la forte présence d'eau (donc d'hydrogène) dans les sujets d'étude.

B.1.1 *Spin, moment magnétique*

Chaque particule possède des propriétés magnétiques propres, dont le spin, que l'on peut assimiler à un moment magnétique. La représentation la plus courante du spin d'un proton est décrite en figure B.1a.

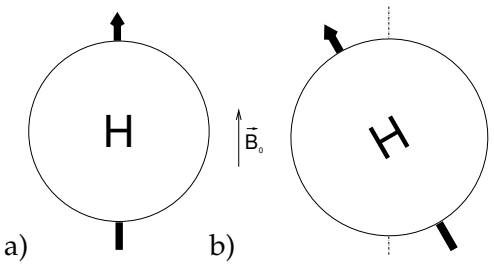

FIGURE B.1 : a) Le moment magnétique est représenté sous la forme d'un vecteur en rotation sur lui-même. b) Mouvement de précession du proton autour de $\overrightarrow{B_0}$.

Au repos (c.-à-d. sans champ magnétique), il n'y a pas d'ordre dans l'orientation des spins. Lorsque l'on plonge les protons dans un champ magnétique $\overrightarrow{B_0}$, les spins de ceux-ci s'orientent dans la même direction que le champ, mais pas nécessairement dans le même sens. On remarque que les protons ont alors un mouvement de précession autour de l'axe de $\overrightarrow{B_0}$ comme indiqué en figure B.1b. Ce mouvement de précession est caractérisé par une fréquence, dite fréquence de Larmor, proportionnelle au champ magnétique. On peut dissocier la précession en une composante longitudinale (dans l'axe $\overrightarrow{B_0}$) et une composante transversale. On appréciera plus avant l'importance de cette décomposition dans le processus d'IRM.

Précession : changement de l'orientation de l'axe de rotation.

Pour s'affranchir de l'approche quantique liée à ces phénomènes, on va se placer d'un point de vue macroscopique et considérer la résultante magnétique globale d'une population de protons donnée. Grâce à la physique statistique (Boltzmann, notamment), on sait que la résultante magnétique longitudinale est dirigée suivant $\overrightarrow{B_0}$ (même sens, même direction). À cause du déphasage de la composante transversale (tous les protons précessent à la même vitesse, mais pas nécessairement avec la même phase), la résultante transversale est nulle.

B.1.2 *Principe de mesure* RMN — T_1 *et* T_2

La technique de mesure en RMN consiste à perturber l'état d'équilibre décrit plus tôt et d'observer le retour à l'équilibre de la population de protons. On vient perturber les protons à l'aide d'ondes de radiofréquence. En envoyant sur l'échantillon des ondes à la fréquence de Larmor, le système va entrer en résonnance. On parle en RMN de phase d'excitation. Lorsque l'on n'émet plus d'onde RF, le système retourne à l'équilibre, et on parle de phase de relaxation.

Lorsque les protons sont excités, cela change l'orientation de l'aimantation macroscopique (alors constituée de la seule composante longitudinale), il s'agit du phénomène de bascule. Il y a donc apparition d'une composante transversale. La relaxation est la phase de retour à une aimantation macroscopique suivant $\overrightarrow{B_0}$ (c.-à-d. à une composante transverse nulle).

La mesure en RMN consiste à évaluer les temps caractéristiques de retour à l'équilibre (ou temps de relaxation) de l'aimantation. Chaque composant (p. ex. : atome, molécule, tissu) possède un T_1 et un T_2 qui lui sont propres. T_1 et T_2 dépendent de l'amplitude du champ magnétique et sont définis comme suit :

- T_1 est le temps nécessaire pour que l'aimantation longitudinale ait atteint 63% de sa valeur finale ;
- T_2 est le temps nécessaire pour que l'aimantation transversale ait perdu 63% de sa valeur initiale.

Les objets étudiés en RMN(patients, produits) ont aussi une densité de protons (notée $N(H)$), qui est aussi une caractéristique propre.

B.2 IMAGERIE

L'imagerie par résonance magnétique est basée sur un certain nombre de séquences d'acquisition RMN. En combinant différents réglages (p. ex. : temps d'acquisition, angle de bascule, fréquence, application de gradients de champ magnétique, etc.) on a accès aux paramètres constitutifs du milieu observé. Ainsi il est possible d'obtenir des cartographies T_1 , T_2 ou $N(H)$ des régions qui nous intéressent.

B.2.1 *Appareillage*

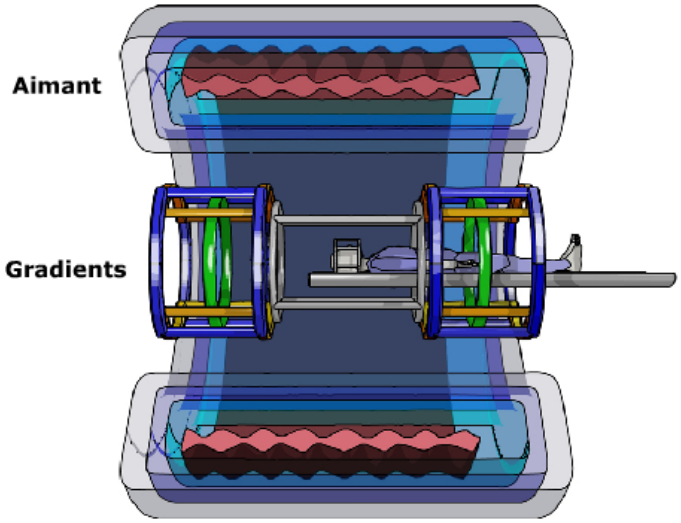

FIGURE B.2 : Vue en coupe d'un appareil IRM standard (illus. Campus Medica)

Pour avoir une qualité satisfaisante, le champ magnétique doit être le plus homogène possible. Il est créé en général, pour les appareils à haut champ ($B_0 > 1$ T), par un aimant supraconducteur, la plupart du temps cylindrique. Celui-ci est alimenté et refroidi en permanence. Les ondes RF sont envoyées et recueillies par des antennes, caractérisées par leur rapport signal sur bruit (plus il est élevé, plus la chaîne de radiofréquence est de bonne qualité).

Gradients

Pour permettre de faire la différence entre les régions de l'espace que l'on étudie, on applique au champ magnétique un certain nombre de gradients. En appliquant un gradient au champ, on va modifier la précession des protons (puisque la fréquence de Larmor est proportionnelle au champ magnétique). Les ondes RF n'influencent alors qu'une certaine partie des protons. Pour simplifier, on peut dire que l'on applique successivement trois gradients dans chaque direction de l'espace : le premier est le gradient dit de sélection de coupe, G_{SC} qui permet de se placer dans un plan ; le deuxième, le gradient de codage de phase, G_{CP} qui localise les protons en introduisant un décalage de phase dans la précession ; le dernier, le gradient de codage de fréquence, G_{CF} qui localise les protons en introduisant un décalage de fréquence.

La qualité des gradients (intensité, vitesse de commutation, etc.) est un élément déterminant pour la bonne réalisation des images, car des gradients plus importants permettent une meilleure résolution spatiale.

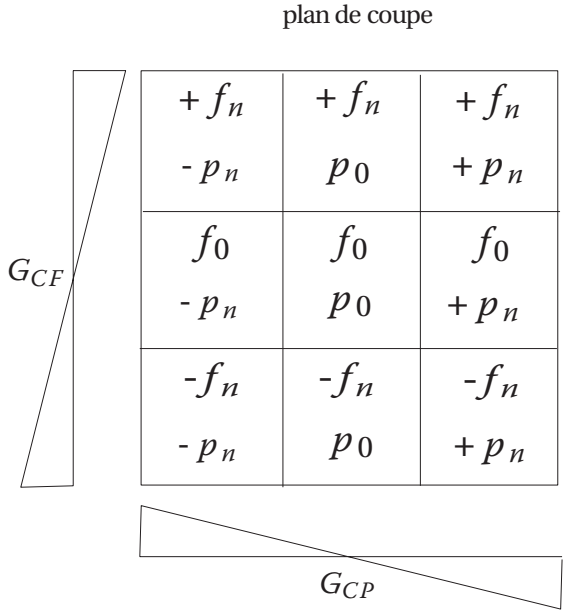

FIGURE B.3 : Gradients de codage. Le gradient de codage de fréquence (G_{CF}) modifie les fréquences des protons ($\pm f_i$) dans la direction suivant laquelle il est appliqué , le gradient de codage de phase (G_{CP}) modifie la phase des protons ($\pm p_i$), mais dans l'autre direction du plan. Les valeurs de fréquence et de phase permettent alors de réaliser un codage du plan.

B.2.2 *Séquences*

Il y a principalement deux types de séquences IRM : la séquence à écho de spin et celle à écho de gradient. Ces séquences ont deux paramètres :

- le temps que l'on met à observer un écho du signal de départ ou temps d'écho TE ;
- le temps entre deux impulsions à 90° ou temps de répétition TR.

Écho de spin (figure B.4)

Elle consiste à :

1. basculer l'aimantation à l'aide d'une impulsion RF à 90° ;
2. inverser le déphasage à l'aide d'une impulsion RF à 180° ;
3. recueillir le signal au temps TE, quand les protons sont à nouveau en phase.

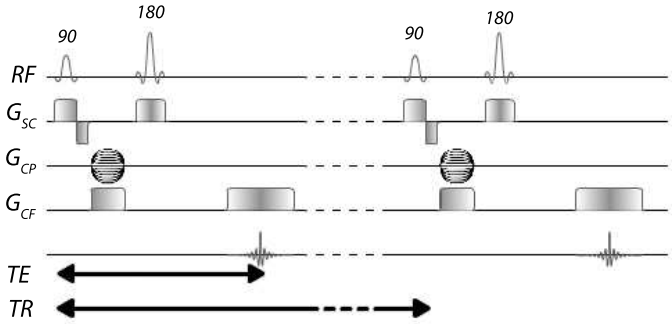

FIGURE B.4 : Séquence d'écho de spin

Écho de gradient (figure B.5)

Pour la séquence à echo de gradient, on n'applique pas d'impulsion à 180°, en revanche on inverse le gradient de codage de phase. Cela permet d'avoir des TE et TR plus courts, en contrepartie d'une plus grande dépendance au déphasage.

Pour simplifier, l'imagerie consiste donc à combiner application de gradients et d'ondes RF de façon adaptée au phénomène à étudier. D'autres types de séquences, et d'autres paramètres existent et permettent d'améliorer l'acquisition d'images dans certaines situations, mais elles sont toutes basées sur ces deux séquences de base.

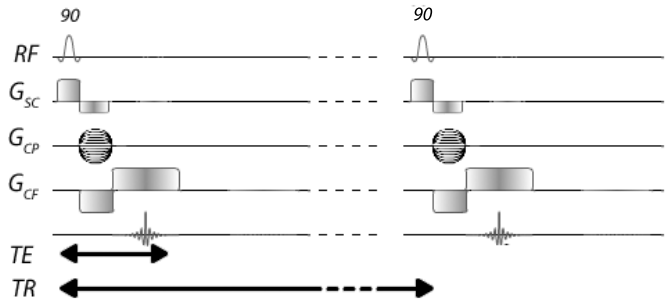

FIGURE B.5 : Séquence d'écho de gradient

B.2.3 *Obtention des images — Pondération*

En jouant sur les paramètres de séquence (TE et TR), on va mettre en avant la variation soit du T_1 , soit du T_2 , soit de la densité de protons.

- Un TR et un TE courts donnent une image indiquant surtout la relaxation T_1 , on parle de pondération T_1 .
- Un TR et un TE longs donnent une pondération T_2 .
- Un TR long et un TE court donnent une pondération en densité de protons.

Le signal recueilli (fréquence, phase) est ensuite soumis à un protocole de traitement du signal (transformations de Fourier et Fourier inverse notamment) pour en donner une image (en niveau de gris) pour laquelle l'intensité lumineuse (le niveau de gris, donc) varie avec les temps de relaxation.

B.3 APPORTS ET CONTRAINTES

En tant que technique de tomographie, l'imagerie par résonance magnétique permet un suivi non-invasif et non-destructif, ce qui constitue un apport majeur dans les études agroalimentaires. En effet, la plupart des produits et des phénomènes étudiés sont évolutifs dans le temps, mais aussi souvent inhomogènes à l'échelle du produit. Un suivi destructif, comme par exemple la découpe de tranches de fromage pour dénombrer les bulles, ne donne qu'une information partielle, et un suivi invasif requiert plus de précautions et ne permet souvent pas de reproduire le phénomène étudié tellement il en perturbe les conditions.

À la différence de l'imagerie clinique, où l'information liée à l'imagerie est essentiellement qualitative (examen de l'image finale) et où les principaux leviers d'analyse sont pondération du signal (cf. B.2.3), un des atouts majeurs de l'imagerie réside dans sa capacité à fournir des informations quantititatives par le post-traitement des images. Les informations qui peuvent être recueillies sont de deux types : géométriques (relevé de dimensions, structure macroscopique, etc.) ou bien, via une modélisation du signal RMN, peut-on avoir accès à certaines caractéristiques physiques des objets étudiés (taux de matière grasse, température, état de contrainte, etc.). En s'assurant d'un protocole expérimental reproductif d'une acquisition sur l'autre, il est alors possible d'avoir un suivi quantitatif au cours du temps.

En revanche, l'IRM apporte un certain nombre de contraintes expérimentales. En effet, suivant le produit observé et les informations recherchées, il y a une première étape de mise au point de la séquence irm qui assurera le meilleur compromis entre :

- une image bien résolue, minimisant l'incertitude de mesure ;
- rapport signal sur bruit le plus important possible pour maximiser la qualité de l'image ;
- un temps d'observation qui soit compatible avec les phénomènes étudiés.

Souvent, un temps d'acquisition relativement long est exigé pour avoir une image à la fois bien résolue et avec un rapport signal sur bruit acceptable. Un autre critère est aussi le champ de vue, qui est la zone qu'il est possible d'observer. Plus cette zone est importante, moins la résolution est importante, et plus le temps d'acquisition augmente. Pour des phénomènes relativement lents comme la croissance de bulle dans les fromages à pâte pressée non-cuite, le temps d'acquisition a relativement peu d'influence, ce qui permet d'aller chercher un optimal de qualité de signal peu importe le temps d'acquisition (chapitre 5). Pour le cas où les phénomènes sont plus rapides (chapitres 2 et 3 par exemple), il faut alors faire des sacrifices en termes de résolution (passage d'une résolution de $0{,}3^3$ mm^3 à $0{,}5^3$ mm^3) pour gagner en temps d'acquisition (passer de l'ordre de l'heure à quelques minutes) et se retrouver sur une fenêtre de temps compatible.

BIBLIOGRAPHIE

BIBLIOGRAPHIE

[1] ITFF-ITG / Actilait. Production de gaz carbonique et formation de l'ouverture dans l'emmental et le comté. etude itg ss 1984/05/c. *Technical study*, 1984. (Cited on page 119.)

[2] José M Aguilera and Peter J Lillford. Microstructural and imaging analyses as related to food engineering. *Food Engineering*, pages 23–38, 2000. (Cited on page 90.)

[3] J.C. Akkerman, P. Walstra, and van H.J.M. Dijk. Holes in dutch type cheese. 1. conditions allowing eye formation. *Netherlands milk and dairy journal*, 1989. (Cited on pages 7, 8 et 91.)

[4] S. H. Alavi, S. S. H. Rizvi, and P. Harriott. Process dynamics of starch-based microcellular foams produced by supercritical fluid extrusion. ii : Numerical simulation and experimental evaluation. *Food Research International*, 36(4) :321–330, 2003. 0963-9969 doi : DOI : 10.1016/S0963-9969(02)00223-5. (Cited on page 117.)

[5] Moris Amon and Costel D. Denson. A study of the dynamics of foam growth : Analysis of the growth of closely spaced spherical bubbles. *Polym. Eng. Sci.*, 24 (13) :1026–1034, 1984. 10.1002/pen.760241306. (Cited on pages 8, 89 et 117.)

[6] A. Arefmanesh, S. G. Advani, and E. E. Michaelides. A numerical study of bubble growth during low pressure structural foam molding process. *Polymer Engineering & Science*, 30(20) :1330–1337, 1990. 10.1002/pen.760302011. (Cited on page 89.)

[7] P. Babin, G. Della Valle, H. Chiron, P. Cloetens, J. Hoszowska, P. Pernot, A. L. Réguerre, L. Salvo, and R. Dendievel. Fast x-ray tomography analysis of bubble growth and foam setting during breadmaking. *Journal of Cereal Science*, 43(3) : 393–397, 2006. (Cited on pages 4 et 83.)

[8] J. Bikard, T. Coupez, G. Della Valle, and B. Vergnes. Simulation of bread making process using a direct 3d numerical method at microscale : analysis of baking step. *International Journal of Material Forming*, 5(1) :11–24, 2012. (Cited on page 90.)

[9] Jérôme Bikard, Thierry Coupez, Guy Della Valle, and Bruno Vergnes. Simulation of bread making process using a direct 3d numerical method at microscale : Analysis of foaming phase during proofing. *Journal of Food Engineering*, 85(2) :259–267, 2008. (Cited on page 90.)

[10] B. Blanc, J. O. Bosset, B. Martin, and J. Jimeno. Gas exchanges at the surface of gruyere cheese during ripening. *Schweizerische Milchwirtschaftliche Forschung*, 12 (2) :30–34, 1983. Times Cited : 0. (Cited on page 119.)

[11] P. Boyaval, C. Deborde, C. Corre, C. Blanco, and E. Begue. Stress and osmoprotection in propionibacteria. *Lait*, 79(1) :59–69, 1999. 186KM Times Cited :10 Cited References Count :29. (Cited on page 119.)

[12] J. Bruchon and T. Coupez. A numerical strategy for the direct 3d simulation of the expansion of bubbles into a molten polymer during a foaming process. *International Journal for Numerical Methods in Fluids*, 57(8) :977–1003, 2008. 10.1002/fld.1660. (Cited on page 89.)

[13] H. Buggisch, P. Mazilu, and H. Weber. Parameter-identification for viscoelastic materials. *Rheologica Acta*, 27(4) :363–368, 1988. Q3046 Times Cited :0 Cited References Count :6. (Cited on page 17.)

[14] J. F. Calzada and M. Peleg. Mechanical interpretation of compressive stress-strain relationships of solid foods. *Journal of Food Science*, 43(4) :1087–1092, 1978. (Cited on pages 34 et 96.)

[15] Grant M. Campbell and Estelle Mougeot. Creation and characterisation of aerated food products. *Trends in Food Science & Technology*, 10(9) :283–296, 1999. 0924-2244 doi : DOI : 10.1016/S0924-2244(00)00008-X. (Cited on pages 89 et 117.)

[16] E. Chiotellis and G. M. Campbell. Proving of bread dough i - modelling the evolution of the bubble size distribution. *Food and Bioproducts Processing*, 81(C3) : 194–206, 2003. 742DB Times Cited :19 Cited References Count :43. (Cited on pages 90 et 118.)

[17] E Chiotellis and GM Campbell. Proving of bread dough ii : measurement of gas production and retention. *Food and bioproducts processing*, 81(3) :207–216, 2003. (Cited on page 90.)

[18] William Mansfield Clark. On the formation of "eyes" in emmental cheese. *Journal of Dairy Science*, 1(2) :91–113, 1917. (Cited on page 8.)

[19] G. G. Codina, S. Mironeasa, C. Mironeasa, C. N. Popa, and R. Tamba-Berehoiu. Wheat flour dough alveograph characteristics predicted by mixolab regression models. *Journal of the Science of Food and Agriculture*, 92(3) :638–644, 2012. (Cited on page 64.)

[20] T. Conde, A. Mulet, G. Clemente, and J. Benedito. Detection of internal cracks in manchego cheese using the acoustic impulse-response technique and ultrasounds. *Journal of Dairy Science*, 91(3) :918–927, 2008. (Cited on page 63.)

[21] J. Culioli and P. Sherman. Evaluation of gouda cheese firmness by compression tests. *Journal of Texture Studies*, 7(3) :353–372, 1976. Times Cited : 74. (Cited on page 83.)

[22] J.F. Davidson and M. A. Cullen. The determination of diffusion coefficients for sparingly soluble gases in liquids. *Transactions of the Institution of Chemical Engineers*, 35 :51–60, 1957. (Cited on page 130.)

[23] B. de Cindio and S. Correra. Mathematical modelling of leavened cereal goods. *Journal of Food Engineering*, 24(3) :379–403, 1995. 0260-8774 doi : DOI : 10.1016/0260-8774(95)90052-D. (Cited on pages 90, 117 et 118.)

[24] M. A. Del Nobile, S. Chillo, A. Mentana, and A. Baiano. Use of the generalized maxwell model for describing the stress relaxation behavior of solid-like foods. *Journal of Food Engineering*, 78(3) :978–983, 2007. ISI Document Delivery No. : 092CB Times Cited : 15 Cited Reference Count : 21 Del Nobile, M. A. Chillo, S. Mentana, A. Baiano, A. ELSEVIER SCI LTD OXFORD. (Cited on pages 17, 18 et 47.)

[25] R. Elshereef, J. Vlachopoulos, and A. Elkamel. Comparison and analysis of bubble growth and foam formation models. *Engineering Computations*, 27(3-4) :387–408, 2010. (Cited on page 89.)

[26] J. Engmann, C. Servais, and A. S. Burbidge. Squeeze flow theory and applications to rheometry : A review. *Journal of Non-Newtonian Fluid Mechanics*, 132(1-3) :1–27, 2005. Times Cited : 38. (Cited on page 34.)

[27] J. J. Eskelinen, A. P. Alavuotunki, E. Haeggstrom, and T. Alatossava. Preliminary study of ultrasonic structural quality control of swiss-type cheese. *Journal of Dairy Science*, 90(9) :4071–4077, 2007. (Cited on page 63.)

[28] J. T. Fan, J. R. Mitchell, and J. M. V. Blanshard. A model for the oven rise of dough during baking. *Journal of Food Engineering*, 41(2) :69–77, 1999. 223EX Times Cited :44 Cited References Count :37. (Cited on pages 90, 117 et 118.)

[29] James J. Feng and Christopher A. Bertelo. Prediction of bubble growth and size distribution in polymer foaming based on a new heterogeneous nucleation model. *Journal of Rheology*, 48(2) :439–462, 2004. (Cited on pages 8, 89, 90 et 111.)

[30] E. Fluckiger, P. Eberhard, and F. Walser. Experiments on eye formation in emmental cheese. *Schweizerische Milchzeitung*, 104(84) :623–624, 1978. Cited Reference Count : 5 ref. Versuche zur Lochbildung im Emmentalerkase. (Cited on pages 64 et 81.)

[31] Lorna J Gibson and Michael F Ashby. *Cellular solids : structure and properties*. Cambridge university press, 1999. (Cited on page 8.)

[32] S. M. Goh, M. N. Charalambides, and J. G. Williams. Large strain time dependent behavior of cheese. *Journal of Rheology*, 47(3) :16, 2003. (Cited on pages 30, 47 et 83.)

[33] S. M. Goh, M. N. Charalambides, and J. G. Williams. Characterisation of non-linear viscoelastic foods by the indentation technique. *Rheologica Acta*, 44(1) : 47–54, 2004. ISI Document Delivery No. : 887KJ Times Cited : 4 Cited Reference Count : 19 SPRINGER NEW YORK. (Cited on pages 18, 30 et 47.)

[34] S. M. Goh, M. N. Charalambides, and J. G. Williams. Characterization of the nonlinear viscoelastic constitutive properties of mild cheddar cheese from indentation tests. *Journal of Texture Studies*, 36(5-6) :459–477, 2005. ISI Document Delivery No. : 987LJ Times Cited : 3 Cited Reference Count : 30 BLACKWELL PUBLISHING OXFORD. (Cited on pages 17, 30 et 47.)

[35] D. Grenier, T. Lucas, and D. Le Ray. Measurement of local pressure during proving of bread dough sticks : Contribution of surface tension and dough viscosity to gas pressure in bubbles. *Journal of Cereal Science*, 52(3) :373–377, 2010. (Cited on page 82.)

[36] David Grenier, Yannick Laridon, Dominique Le Ray, Sylvain Challois, and Tiphaine Lucas. Experimental growth of a single eye in a semi-hard cheese under a known gas pressure : an mri device and its associated methods. *Food Research International*, to be submitted. (Cited on pages 95 et 97.)

[37] David Grenier, Tiphaine Lucas, and Dominique Le Ray. Gas pressure measurements in eyes of semi-hard cheese : Influence of the cheese outskirts on the growth of the bubbles at the core of the cheese. *International Dairy Journal*, to be submitted. (Cited on pages xiv, 78, 81, 82, 83, 91, 93 et 131.)

[38] D. Guggisberg, M. T. Frohlich-Wyder, S. Irmler, M. Greco, D. Wechsler, and P. Schuetz. Eye formation in semi-hard cheese : X-ray computed tomography as a non-invasive tool for assessing the influence of adjunct lactic acid bacteria. *Dairy Science and Technology*, 93(2) :135–149, 2013. (Cited on page 63.)

[39] L. Hailemariam, M. Okos, and O. Campanella. A mathematical model for the isothermal growth of bubbles in wheat dough. *Journal of Food Engineering*, 82(4) : 466–477, 2007. ISI Document Delivery No. : 177RG Times Cited : 5 Cited Reference Count : 48. (Cited on pages 90, 117 et 118.)

[40] Conn J F Handleman, A R and J W Lyons. Bubble mechanics in thick foams and their effects on cake quality. *Ceral Chemistry*, 38 :294–305, 1961. (Cited on page 89.)

[41] R. Harper and M. Baron. Cheese grading. mechanical properties compared with quality assessed subjectively. *Journal of Dairy Research*, 16(03) :363–367, 1949. (Cited on page 17.)

[42] D. H. Hettinga and G. W. Reinbold. The propionic acid bacteria - a review. ii. metabolism. *Journal of Milk and Food Technology*, 35 :358–372, 1972. (Cited on page 133.)

[43] H Huang and J.L. Kokini. *Prediction of dough volume development which considers the biaxial extensional growth of cells*, pages 113–120. Eagan Press, St Paul, MN, USA, 1999. (Cited on page 89.)

[44] D. Huc, F. Mariette, S. Challois, J. Barreau, and G. Moulin. Multi-scale investigation of eyes in semi-hard cheese. *Innovative Food Science and Emerging Technologies*, 2013. (Cited on pages 3, 34, 90, 118 et 139.)

[45] D. Huc, C. Michon, N. Roland, S. Challois, and F. Mariette. Influence of salt content on eye growth in semi-hard cheeses using mri and co2 production measurements. *International Dairy Journal*, 2014. (Cited on pages 3, 119, 129 et 130.)

[46] Delphine Huc. *Hiérarchisation des facteurs contribuant à la croissance des bulles dans des fromages à pâte pressée non cuite par une approche multi-échelles*. PhD thesis, Université de Rennes 1, 2013. (Cited on pages 5, 9 et 121.)

[47] Delphine Huc, Sylvain Challois, Matthieu Monziols, Camille Michon, and François Mariette. Spatially-resolved characterization of eye-growing kinetics in semi-hard cheeses. *Journal of Dairy Science*, 2014. (Cited on pages 63 et 83.)

[48] M. Jakobsen, P. N. Jensen, and J. Risbo. Assessment of carbon dioxide solubility coefficients for semihard cheeses : the effect of temperature and fat content. *European Food Research and Technology*, 229(2) :287–294, 2009. Times Cited : 0. (Cited on pages 118, 119, 131, 132 et 133.)

[49] JCGM. *Guide to the expression of uncertainty in measurement*. BIPM, 2008. (Cited on pages 68 et 72.)

[50] S. F. Jones, G. M. Evans, and K. P. Galvin. Bubble nucleation from gas cavities — a review. *Advances in Colloid and Interface Science*, 80(1) :27–50, 1999. (Cited on page 117.)

[51] Matti Keentok, Marcus P. Newberry, Peter Gras, Frank Bekes, and Roger I. Tanner. The rheology of bread dough made from four commercial flours. *Rheologica Acta*, 41(1-2) :173–179, 2002. (Cited on page 118.)

[52] Gyeong-Won Kim, Gab-Soo Do, Yeonghwan Bae, and Yasuyuki Sagara. Determination of the viscoelastic properties of agar/agar-gelatin gels based on finite element method optimization. *Food Science and Technology Research*, 14(6) :525–525, 2008. (Cited on page 18.)

[53] Gyeong-Won Kim, Man-Soo Kim, Yasuyuki Sagara, Yeong-Hwan Bae, In-Bok Lee, Gab-Soo Do, Sung-Hyoun Lee, and Suk-Won Kang. Determination of the viscoelastic properties of apple flesh under quasi-static compression based on finite element method optimization. *Food Science and Technology Research*, 14(3) :221–231, 2008. (Cited on page 18.)

[54] M. Kontopoulou and J. Vlachopoulos. Bubble dissolution in molten polymers and its role in rotational molding. *Polymer Engineering and Science*, 39(7) :1189–1198, 1999. Kontopoulou, M Vlachopoulos, J. (Cited on page 90.)

[55] H. Kraggerud, J. P. Wold, M. Hoy, and R. K. Abrahamsen. X-ray images for the control of eye formation in cheese. *International Journal of Dairy Technology*, 62 (2) :147–153, 2009. ISI Document Delivery No. : 448NA Times Cited : 1 Cited Reference Count : 16 Kraggerud, H. Wold, J. P. Hoy, M. Abrahamsen, R. K. Wiley-blackwell publishing, inc Malden. (Cited on page 63.)

[56] R.S. Lakes. *Viscoelastic Materials*. Cambridge University Press, 2009. (Cited on page 17.)

[57] Y. Laridon, C. Doursat, D. Grenier, C. Michon, D. Flick, and T. Lucas. New method for the assessment of the viscoelastic parameters of materials. application to semi-hard type cheese. *Rheologica Acta*, Submitted. (Cited on pages 77, 82, 83, 96, 97, 98, 124 et 138.)

[58] Y. Laridon, D. Grenier, D. Houeix, C. Doursat, T. Lucas, and D. Flick. Modelling of the growth of a single bubble in semi-hard cheese ; with experimental verification and sensitivity analysis. *Journal of the Mechanics and Physics of Solids*, to be submitted. (Cited on pages 63, 119, 134 et 137.)

[59] B. Launay and C. Michon. Biaxial extension of wheat flour doughs : Lubricated squeezing flow and stress relaxation properties. *Journal of Texture Studies*, 39(5) : 496–529, 2008. ISI Document Delivery No. : 351GJ Times Cited : 1 Cited Reference Count : 78 Launay, B. Michon, C. BLACKWELL PUBLISHING OXFORD. (Cited on pages 34 et 118.)

[60] Han Choon Lee, Byung Do Oh, Sung Won Bae, and Moo Hwan Kim. Single bubble growth in saturated pool boiling on a constant wall temperature surface. *International Journal of Multiphase Flow*, 29(12) :1857–1874, 2003. (Cited on page 63.)

[61] Kija Lee, Kaho Uegaki, Chihiro Nishii, Tadashi Nakamura, Auska Kubota, Tsunao Hirai, and Kazutaka Yamada. Computed tomographic evaluation of gas hole formation and structural quality in gouda-type cheese. *International Journal of Dairy Technology*, 65(2) :232–236, 2012. Times Cited : 0. (Cited on page 63.)

[62] Shau-Tarng Lee, N. S. Ramesh, and Gregory A. Campbell. Study of thermoplastic foam sheet formation. *Polymer Engineering & Science*, 36(19) :2477–2482, 1996. 10.1002/pen.10645. (Cited on pages 8 et 117.)

[63] ShauTarng Lee and N. S. Ramesh. *Polymeric Foams : Mechanisms and Materials*. CRC Press, Boca Raton, London, New York, Washington DC, 2004. (Cited on page 89.)

[64] P. Masi and F. Addeo. An examination of some mechanical properties of a group of italian cheeses and their relation to structure and conditions of manufacture. *Journal of Food Engineering*, 5(3) :217–229, 1986. (Cited on page 83.)

[65] Paolo Masi. Characterization of history-dependent stress-relaxation behaviour of cheeses. *Journal of Texture Studies*, 19(4) :373–388, 1988. (Cited on pages 17 et 18.)

[66] Toshiro Minami, Susumu Maeda, Mitsuo Higasa, and Kazuhiko Kashima. In-situ observation of bubble formation at silicon melt–silica glass interface. *Journal of Crystal Growth*, 318(1) :196–199, 2011. (Cited on page 63.)

[67] C. C. Mourtada-Bonnefoi and H. M. Mader. Experimental observations of the effect of crystals and pre-existing bubbles on the dynamics and fragmentation of vesiculating flows. *Journal of Volcanology and Geothermal Research*, 129(1–3) :83–97, 2004. (Cited on page 63.)

[68] M. Musse, S. Challois, D. Huc, S. Quellec, and F. Mariette. Mri method for investigation of eye growth in swiss-type cheese. *Journal of Food Engineering*, 2014. (Cited on pages 63, 69, 70, 96 et 121.)

[69] Oded Navon, Anatoly Chekhmir, and Vladimir Lyakhovsky. Bubble growth in highly viscous melts : theory, experiments, and autoexplosivity of dome lavas. *Earth and Planetary Science Letters*, 160(3–4) :763–776, 1998. (Cited on page 89.)

[70] D. J. O'Callaghan and T. P. Guinee. *Rheology and Texture of Cheese*, volume Volume 1, pages 511–540. Academic Press, 2004. (Cited on page 17.)

[71] N. Otsu. Threshold selection method from gray-level histograms. *Ieee Transactions on Systems Man and Cybernetics*, 9(1) :62–66, 1979. ISI Document Delivery No. : GE960 Times Cited : 4354 Cited Reference Count : 5 Otsu, n Ieee-inst electrical electronics engineers inc New york. (Cited on pages 70, 95 et 154.)

[72] R. D. Patel. Bubble-growth in a viscous newtonian liquid. *Chemical Engineering Science*, 35(11) :2352–2356, 1980. (Cited on page 89.)

[73] J. P. Pauchard, E. Flückiger, J. O. Bosset, and B. Blanc. Co2 solubility, concentration and distribution in relation to eye formation in emmental cheese. *Schweizerische Milchwirtschaftliche Forschung*, 9(4) :69–73, 1980. Times Cited : 0. (Cited on page 132.)

[74] M. Peleg. Considerations of a general rheological model for the mechanical behavior of viscoelastic solid food materials. *Journal of Texture Studies*, 7(2) :243–255, 1976. (Cited on page 17.)

[75] R. H. Perry. *Perry's Chemical Engineers' Handbook*. McGraw-Hill Professional, 8th edition edition, 2007. (Cited on page 132.)

[76] M. S. Plesset. The dynamics of cavitation bubbles. *Journal of Applied Mechanics*, 16 :277–82, 1949. (Cited on pages 7 et 89.)

[77] N. S. Ramesh, H. Rasmussen Don, and A. Campbell Gregory. Numerical and experimental studies of bubble growth during the microcellular foaming process. *Polymer Engineering & Science*, 31(23) :1657–1664, 1991. 10.1002/pen.760312305. (Cited on pages 8, 89 et 90.)

[78] Rayleigh. On the pressure developed in a liquid during the collapse of a spherical cavity. *Philosophical Magazine Series 6*, 34(200) :94–98, 1917. 1941-5982. (Cited on page 7.)

[79] N. B. Richoux, D. Deibel, R. J. Thompson, and C. C. Parrish. Seasonal and developmental variation in the fatty acid composition of mysis mixta (mysidacea) and acanthostepheia malmgreni (amphipoda) from the hyperbenthos of a cold-ocean environment (conception bay, newfoundland). *Journal of Plankton Research*, 27(8) : 719–733, 2005. 974LM Times Cited :14 Cited References Count :34. (Cited on page 119.)

[80] Rocio Rodriguez-Aguilera, Jorge C. Oliveira, Julio C. Montanez, and Pramod V. Mahajan. Gas exchange dynamics in modified atmosphere packaging of soft cheese. *Journal of Food Engineering*, 95(3) :438–445, 2009. (Cited on page 119.)

[81] Harald Rohm and Harald Lederer. Uniaxial compression of swiss-type cheese at different strain rates. *International Dairy Journal*, 2(6) :331–343, 1992. (Cited on page 47.)

[82] R. Sander. Compilation of henry's law constants for inorganic and organic species of potential importance in environmental chemistry, 1999. (Cited on page 131.)

[83] P. Schuetz, D. Guggisberg, I. Jerjen, M. T. Frohlich-Wyder, J. Hofmann, D. Wechsler, A. Flisch, W. Bisig, U. Sennhauser, and H. P. Bachmann. Quantitative comparison of the eye formation in cheese using radiography and computed tomography data. *International Dairy Journal*, 31(2) :150–155, 2013. (Cited on page 63.)

[84] A. M. Seuvre and M. Mathlouthi. Contribution to the study of gas-release during the maturation of a french emmental cheese. *Lebensmittel-Wissenschaft & Technologie*, 15(5) :258–262, 1982. Pn270 Times Cited :1 Cited References Count :36. (Cited on page 119.)

[85] P. Shah, M. Campbell, G, .L. McKee, S, and C. D. Rielly. *Proving of bread dough : modelling the growth of individual bubbles*, volume 76. Institution of Chemical Engineers, 1998. (Cited on pages 89, 90, 117 et 118.)

[86] IM Sobol. Global sensitivity indices for nonlinear mathematical models and their monte carlo estimates. *Mathematics and Computers in Simulation*, 55(1–3) :271–280, 2001. (Cited on page 101.)

[87] Alina Surmacka Szczesniak. Objective measurements of food texture. *Journal of Food Science*, 28(4) :410–420, 1963. (Cited on page 17.)

[88] Arthur V. Tobolsky. Elastoviscous properties of polyisobutylene. vi. relation between stress relaxation modulus and dynamic modulus. *Journal of the American Chemical Society*, 74(15) :3786–3788, 1952. doi : 10.1021/ja01135a021. (Cited on page 17.)

[89] D. C. Venerus, N. Yala, and B. Bernstein. Analysis of diffusion-induced bubble growth in viscoelastic liquids. *Journal of Non-Newtonian Fluid Mechanics*, 75(1) :55–75, 1998. 0377-0257 doi : DOI : 10.1016/S0377-0257(97)00076-1. (Cited on page 89.)

[90] David C Venerus and Nadia Yala. Transport analysis of diffusion-induced bubble growth and collapse in viscous liquids. *AIChE Journal*, 43(11) :2948–2959, 1997. 10.1002/aic.690431108. (Cited on page 8.)

[91] D. Vivier, D. Compan, G. Moulin, and P. Galzy. Study of carbon dioxide release from feta cheese. *Food Research International*, 29(2) :169–174, 1996. Uy713 Times Cited :3 Cited References Count :13. (Cited on page 119.)

[92] S. R. White, J. R. Broadbent, C. J. Oberg, and D. J. McMahon. Effect of lactobacillus helveticus and propionibacterium freudenrichii ssp shermanii combinations on propensity for split defect in swiss cheese. *Journal of Dairy Science*, 86(3) :719–727, 2003. 656HD Times Cited :8 Cited References Count :33. (Cited on page 119.)

[93] MB Whitworth and JM Alava. Non-destructive imaging of bread and cake structure during baking. In *Using Cereal Science and Technology for the Benefit of Consumers : Proceedings of the 12th International ICC Cereal and Bread Congress 24-26 May, 2004*, volume 109, page 456. CRC Press, 2004. (Cited on page 4.)

[94] T. Yano and Y. Shimiya. Expansion of a spherical hole in elastic food materials with surface-tension. *Agricultural and Biological Chemistry*, 52(12) :3113–3117, 1988. (Cited on pages 64 et 90.)

Modélisation et visualisation d'une croissance de bulle dans un milieu viscoélastique évolutif et hétérogène

Résumé

L'objectif de cette thèse était de caractériser, de modéliser et de hiérarchiser les mécanismes acteurs de la croissance de bulles dans un fromage à pâte pressée non-cuite à l'échelle de la bulle. Pour cela, trois étapes majeures ont été envisagées. Une première étape de mise au point d'une méthode de détermination des paramètres du modèle mécanique (modèle de Maxwell généralisé) par ajustement de courbes expérimentales de compression-relaxation a été effectuée. Une deuxième étape de validation a consisté en la réalisation d'un dispositif expérimental permettant de soumettre une bulle isolée dans un cylindre de fromage à diverses sollicitations mécaniques, à suivre l'évolution du dispositif en temps réel et de façon non invasive par IRM, et à confronter ces résultats à des simulations reproduisant les conditions d'acquisition. Une dernière étape a consisté à rajouter la prise en compte du transport de matière (CO_2) au sein du fromage dans la modélisation. Les résultats de simulation ont dans un premier temps été confrontés au comportement moyen des bulles au sein d'un bloc de fromage, et dans un deuxième temps un dispositif expérimental de validation similaire à celui de l'étape précédente a été développé.

La caractérisation mécanique du fromage a montré que les propriétés rhéologiques n'évoluent pas au cours de l'affinage, mais qu'elles sont soumises à un fort gradient spatial. Le modèle de Maxwell a été validé expérimentalement dans des conditions de sollicitations mécaniques uniquement et une étude de sensibilité a permis de montrer la forte influence des temps de relaxation les plus longs (plusieurs heures) et de la position de la bulle sur la croissance. L'étude du couplage entre transport de quantité de mouvement et transport de matière dans un contexte de croissance d'une seule bulle a permis de montrer la grande influence des paramètres de transport de matière sur la croissance de bulle, en particulier pour le coefficient de diffusion et le taux de production de CO_2. Dans un contexte où deux cavités gazeuses sont mobilisées, les paramètres géométriques (position, dimensions, forme des cavités) se sont montrés aussi importants que les paramètres de transport de matière.

Abstract

The objective of this PhD thesis was to characterise, model and rank the mechanisms involved in the growth of bubbles in semi-hard cheeses, at the bubble scale. Three steps were considered. First, a mechanical characterisation of the material enabled to define a rheological model to describe the behaviour of the material (generalised Maxwell model), and to set-up a method to determine the model parameters by fitting of compression-relaxation data. Secondly, the Maxwell model consisted in setting up an experimental validation procedure allowing studying different loads on a single bubble surrounded by a cheese cylinder. Experiments were monitored in real-time in a non-invasive manner by MRI imaging and were compared to simulations reproducing the experimental conditions. Finally, mass transport (CO_2) was also taken into account in the model. Simulation results were first compared to the average bubble growth in cheese blocks, and then a dedicated experimental set-up similar to that used previously was used.

Mechanical characterisation of semi-hard cheese showed the rheological properties did not evolve during ripening, but presented a steep spatial gradient. Despite its simplicity, the Maxwell model showed good agreement with the experimental results. A sensitivity study demonstrated that the highest relaxation time (about several hours) and the bubble position were the most influent parameters over bubble growth, when only the mechanical model was involved. Coupling between mass and momentum transport in a single bubble case demonstrated the great influence of the mass transport parameters on bubble growth, especially diffusivity and CO_2 production rate. In the case where two gaseous cavities are involved, geometric parameters (cavities positions, dimensions and shape) proved to be as important as the mass transport parameters on the bubble growth.